A study on SERS sensor for the identification and spatial distribution visualization of the VOC gas

陳, 林

A study on SERS sensor for the identification and spatial distribution visualization of the VOC gas

Chen Lin

Joint Graduated School of Mathematics for Innovation

Kyushu University

January 2024

Acknowledgements

Throughout the journey of pursuing a doctoral degree at Kyushu University, I encountered numerous challenges, experienced failures, and moments of confusion. However, with the support of my supervisors, friends, and encouragement from my family, I persistently sought solutions, enhanced my research skills, and maintained a positive outlook on life. It is through these efforts that I was able to successfully complete my doctoral dissertation.

I would like to express my deepest gratitude to my supervisor, Prof. Kenshi Hayashi, for his unwavering support, invaluable guidance, and profound expertise throughout my research journey. He also granted me sufficient freedom to explore areas of my research interest and offered insightful advice when I faced uncertainties, thus advancing the completion of my research project. Additionally, his kindness, gentle demeanor, and positive approach to life are goals I aspire to achieve in the future.

I extend my sincere appreciation to the professors who assisted me in conducting my experiment. Prof. Fumihiro Sassa taught me how to use laboratory equipment and engaged in discussions during laboratory meetings regarding my experimental results. Prof. Bin Chen was my undergraduate supervisor who introduced me to the world of research and recommended me to pursue a doctoral degree under Prof. Hayashi's guidance. She patiently guided me through research projects, offering constructive feedback on my experimental outcomes, which facilitated the continuation of experiments. I'm also grateful to Professor Chuanjun Liu, who guided me on crafting a well-structured paper and gave me the opportunity to visit his laboratory.

I would like to express my sincere gratitude to the doctoral thesis reviewer, Prof. Yuji Oki, Prof. Fumihiro Sassa, and Prof. Shizuo Kaji. They provided professional advice that helped me revise my dissertation and allowed for its better completion.

I am immensely grateful to the staffs in Hayashi lab, Ms. Maiko Moribe, Mr. Shigeru Kaneko, and Ms. yuukou Saruwatari. When I first arrived in Japan, unable to speak Japanese, Ms. Moribe assisted me by translating and editing numerous Japanese documents. Moreover, she gave me a lot of life advice, aiding me in quickly adjusting to life in Japan. Mr. Kaneko was a researcher at a company, and during my job search, I had numerous discussions with him regarding interview techniques and career planning experiences. Additionally, we exchanged life experiences, which allowed me to gain a better understanding of Japanese culture and customs. Ms. Saruwatari helped me manage a lot of paperwork, saving time and ensuring I had ample time for my experiments.

Special thanks go to members in Hayashi lab. Dr. Lingpu Ge, Mr. Hao Guo, Ms. Shiyi Zhang, Mr. Cong Wang, Mr. Zeping Yu, Ms. Xiao Ye, Mr. Zihan Luo, Mr. Yasuhiro Kusuda, Mr. Tianshu Jiang, Mr. Zongyuan Yang, and all friends in Hayashi lab. They brought me a lot of joy in life and provided me with assistance. Furthermore, I'd like to thank my basketball buddies and Mr. Yang Gao; we competed together, shared drinks, and alleviated the stress of studying.

I am indebted to Joint Graduate School of Mathematics for Innovation (JGMI), for their financial support, which enabled me to complete the doctoral program. I would also like to thank Prof. Shizuo Kaji for providing me with the opportunity to conduct research in image processing and offering invaluable guidance on data processing issues.

Lastly, I want to express my gratitude to my dear family for their financial support and providing me with the freedom to pursue my passions.

Abstract

The main origins of volatile organic compounds (VOC) in the air include human production and activities, as well as natural processes. Monitoring and controlling VOC can reduce emissions caused by human activities, thereby maintaining environmental quality and safeguarding human health. Gas sensor technology, as an online detection method, has been widely utilized for the detection and identification of VOC gases. Simultaneously, upon identifying the types of gases, visualizing their spatial distribution allows for the search of gas sources and facilitates understanding the information within the gas sources. Gas sensors based on the principles of Surface enhanced Raman scattering (SERS) offer rapid response, molecular-level detection sensitivity, specific identification based on molecular structure, and high-resolution visualization capabilities. Therefore, the aim of this research is to develop a SERS gas sensing platform capable of identifying multiple VOC and visualizing the spatial distribution of gases. This dissertation comprises five chapters outlined as follows:

In Chapter 1, the study's background was introduced. The introduction and gas sensor technologies related to VOC were depicted. Moreover, the detection principles and fabrication methods of SERS sensors were explained.

In Chapter 2, the SERS sensor with high intensity, combined with an adsorption concentrating method, was utilized to detect ultra-low concentrations of geosmin in aqueous solutions. Gas was generated from a heated geosmin aqueous solution using a bubbling method. Upon contact with the cooler surface of the sensor, the high-temperature gas condensed into mist, enabling the collection of geosmin SERS spectra. With our ultra-high sensitivity detection system, a response ranges from 10 ppt to 10 ppb geosmin in ultrapure water was confirmed. Additionally, detection of 100 ppt geosmin in tap water was achievable.

In Chapter 3, a multiple SERS gas sensor matrix via spin-coating functional polymer was proposed to enhance gas recognition capability. Polymer films were fabricated using Poly(acrylic acid), Poly(methyl methacrylate), and Polydimethylsiloxane. The high design flexibility of a double-layer film was achieved using the layer-by-layer method with two single-layer films. SERS gas sensor coated with different polymer films exhibited distinct affinity to target gases. The principal component analysis algorithm was utilized to visualize the gas clusters in a two-dimensional graph. The three target gases—phenethyl alcohol, acetophenone, and anethole—were effectively distinguished when analyzing the characteristic variables in

the response matrix, which combined gas responses obtained from sensors coated with three single-layer and three double-layer films.

In Chapter 4, a SERS sensor array was developed to visualize the spatial distribution of gas evaporating from the odor source. The SERS sensor array was positioned above the odor source and scanned by a homemade detection system to acquire the SERS spectra matrix of the odor gas. The intensities of the characteristic peaks from the collected spectra were utilized to generate a heatmap image. After noise reduction processing of the heatmap image, the localization of the odor source became distinctly identifiable in the resultant graph. Additionally, the size of the odor source could be determined using the visualization result. Moreover, this method was employed to visualize the spatial distribution of two distinct odor sources. To recognize between these two odor sources, the non-negative matrix factorization algorithm was utilized to decompose the obtained SERS spectra matrix, extracting feature and concentration information at each spot on the sensor array. The feature information was used to identify the odor source, while the concentration information facilitated the generation of the heatmap image. Gaussian fitting was applied to process the image for localizing the odor source. Consequently, the localizations of these two odor sources were identified and visualized using a single heatmap image.

In Chapter 5, the experimental results were summarized, and the future prospects of this dissertation were presented.

Table of contents

List of figures

List of tables

List of Symbols and Abbreviations

C	Concentration of gas	ppm
D_r	Diffusion rate	mg/min
F	Flow rate of diluent gas	L/min
k	Factor for converting gas weight to gas volume	
M	Molecular weight	g/mol
P	Gas pressure	mmHg
t	Temperature in the chamber	°C
ppm	Parts per million	
ppb	Parts per billion	
ppt	Part per trillion	
P_r	Induced polarization of Raman scattering	
α	Raman polarizability of the electrons	
E	Applied electric fields	
rpm	Revolutions per minute	
VOC	Volatile organic compounds	
GC-MS	Gas Chromatography-Mass Spectrometry	
MOS	Metal oxide semiconductor	
QCM	Quartz crystal microbalance	
NDIR	non-dispersive infrared	
FTIR	Fourier transform infrared	
E-nose	Electronic-nose	
SERS	Surface-enhanced Raman scattering	
Ag NPs	Silver nanoparticles	
EM	electromagnetic mechanism	
CM	Chemical mechanism	
LSPR	Localized surface plasmon resonance	
EFs	Enhanced factors	
PCA	Principal component analysis	
2D	two-dimensional	
MIB	2-methylisoborneol	
GSM	Geosmin	

MFC	Mass flow controller	
PAA	Poly (acrylic acid)	
PMMA	Poly (methyl methacrylate)	
PDMS	Polydimethylsiloxane	
FT/IR	Fourier transform infrared spectroscopy	
SEM	Scanning electron microscope	
UV	Ultraviolet	
AA	L-ascorbic acid	
4-ATP	4-aminothiophenol	
BZD	Benzaldehyde	
EBZD	4-ethylbenzaldehyde	
UV-vis	Ultraviolet-visible	
RSD	Relative standard deviation	
LU	Left-Up	
C	Center	
LB	Left-Bottom	
RU	Right-Up	
RB	Right-Bottom	
NMF	Non-negative matrix factorization	
CNN	Convolutional neural network	
t-SNE	t-distributed stochastic neighbor embedding	
NBC	Naive Bayesian classifier	
SVM	Support vector machine	
RFC	Random forest classifier	
DWT	Discrete wavelet transform	

Chapter 1

1. Introduction

1.1 Volatile Organic Compounds gas detection

1.1.1 Volatile organic compounds (VOC) gas

Volatile organic compounds (VOC) are a group of organic chemicals with a relatively high vapor pressure at room temperature, easily evaporating and emitted as gases from solid or liquid sources [1]. To understand the specifics of VOC gases, classification based on their chemical functional structures is applied. Consequently, VOC gases can mainly be categorized as alkanes, esters, alcohols, aldehydes, halogenated compounds, and aromatic compounds [2, 3]. The VOC gases with different functional group present distinct property. Alkenes and aromatic compounds are often considered pollutants due to their role in the formation of photochemical ozone in the environment [3]. Halogenated VOC are hazardous components owing to their strong bioaccumulation potential, inherent toxicity, and stability [4].

VOC gases are produced from diverse emission sources, encompassing both natural origin and human activities. They can contribute to environmental pollution and in some cases, have adverse health effects on humans when present in high concentrations indoors or outdoors. In addition, both the quantity and diversity of the VOC gases produced as byproducts fluctuate during biological processes. For instance, respiration in humans and animals, metabolic processes in plants, microbial activity, and the decomposition of organic matter can all release VOC gases. Therefore, VOC gases can be used as marker of health diagnosis, food quality, process of plant growth [5].

1.1.2 Detection of VOC gas

Detecting VOC gases is challenging and complex due to their presence in low concentrations, and the presence of various constituent components. If VOC gases could be successfully detected, a wealth of valuable information covering category, concentration, and spatial distribution could be acquired.

- Category: Given the complexity of real-world applications, the target VOC gas often coexists with other interfering gases. The target VOC gas should be accurately distinguished from other gas components.
- Concentration: The quantity of gas molecules can be reflected by its concentration.

Typically, high concentrations of VOC gases pose harm to the environment or human health. Therefore, effectively avoiding their negative impact can be achieved by detecting the concentration of the target VOC gas.

- Spatial distribution: The spatial distributions of VOC gases differ in the absence and presence of airflow. (1) In the absence of wind, gas diffusion may be more restricted, leading to a more localized concentration distribution. Through the spatial distribution of VOC gas in this condition, we can comprehend the information encapsulated in the odor source, encompassing composition, size, and temporal variations.; (2) In the presence of wind, gas diffusion occurs more extensively. The wind carries gases, dispersing them across broader areas, resulting in a more uniform distribution or faster dispersion. Analyzing this gas spatial distribution using a robot equipped with recognition algorithms enables the localization of odor sources.

1.2 Gas sensing method

1.2.1 Gas chromatography-mass spectrometry

Gas chromatography-mass spectrometry (GC-MS) is a powerful analytical technology for identification and quantification of multiple compounds in the gas samples [6, 7]. First, GC separates the components of a complex gas sample by their different volatilities as they pass through a chromatographic column. Next, MS identifies and quantifies these separated components by analyzing their mass-to-charge ratios and fragmentation patterns. In this stage, the separated components are ionized by a high-energy electron beam, creating charged particles. These charged particles are then accelerated through an electric field, determined by a mass analyzer to confirm their mass-to-charge ratios. Consequently, the fragmentation patterns (fingerprint) of the compounds are recorded in mass spectra, aiding in the identification and quantification of the various components. GC-MS has gained extensive application due to its high sensitivity in analyzing mixed gas samples across various fields, encompassing food [8] and environmental analyses [9], as well as disease diagnosis [6]. However, this method can’t be utilized in on-site and in vivo detection because of its high cost, bulky equipment, and time-consuming processing. Hence, the portable and cost-effective sensor need to be developed for VOC gas sensing.

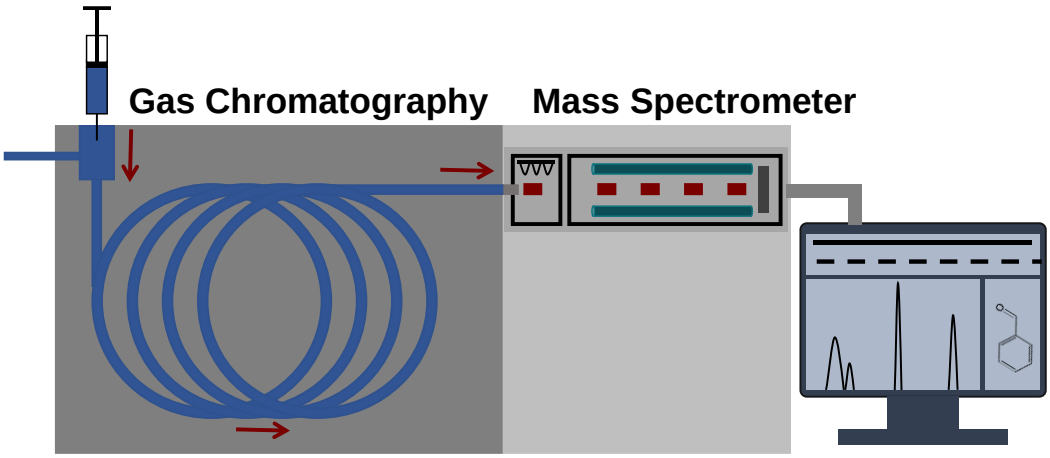

Fig. 1. 1. Schematic diagram of GC-MS for analyte detection.

1.2.2 Gas sensor technology

1.2.2.1 Semiconductor sensors

A semiconductor gas sensor is a device that utilizes semiconductor materials to detect the concentration of a specific gas by measuring the electrical changes with the device. These sensors rely on the interaction between gases and the semiconductor surface (sensing material), causing changes in the physical parameters of the semiconductor material such as conductivity, permittivity, and work function [10]. The altered physical parameters are transduced into electronic signals, such as resistance, capacitance, and inductance, by the VOC gas sensor. Consequently, the changed electronic signal values enable the detection of the concentration of a target VOC gas.

Varity of semiconductor materials have been utilized in the fabrication of gas sensor, including metal oxide, conductive polymer, carbon materials, metal nanoparticles, and hybrid composites. The metal oxide materials have been widely used to fabricate the metal oxide semiconductor (MOS) sensors. Based on the majority charge carriers in the semiconductor materials, there are primarily p-type MOS sensors (e.g., CuO) carrying holes and n-type MOS sensors (e.g., SnO_2, TiO_2, WO_3, ZnO, SnO_2, NiO) carrying electron. In the air, oxygen molecules adsorb onto the semiconductor material surface, forming various oxygen species like O^{2-}, O^-, and O_2^- ions by capturing electrons from the conduction band [11-13]. This leads to the creation of an electron depletion region on the surface of n-type semiconductor materials and an accumulation of holes in p-type semiconductor materials. In n-type MOS sensors, when reducing gas molecules react with oxygen ions, electrons return to the conduction band of the sensing

material, reducing the thickness of the electron depletion region and decreasing the sensor's resistance. Conversely, oxidizing gases capture electrons from the oxygen species, increasing the resistance of n-type sensing materials [14]. For p-type MOS sensor, the material functions as an acceptor, forming a hole accumulation region. Exposure to reducing analytes causes the hole accumulation layer to thin due to the electron-hole recombination process, reducing the hole concentration in the p-type MOS sensor and consequently increasing the device's overall resistance. Conversely, the resistance is decreased when oxidizing gases are detected [15]. MOS sensors have been developed to detect various gas analytes, such as H_2, nitrogen oxides (NO_x), carbon monoxide (CO), NH_3, ethanol, H_2S, and VOC. ZnO nanorods were synthesized via a hydrothermal method to detect ethanol gas, exhibiting fast response/recovery time and high response [16]. TiO_2 nanofibers were developed through electrospinning a hybrid solution for detection of CO gas. This MOS sensor showed a response to CO concentrations as low as 1 ppm [17]. CuO nanowires were fabricated via a template-assisted electrodeposition method, exhibiting good repeatability and achieving a detection limit of 2.5 ppb for H2S gas [18]. The main advantages of MOS sensors include high sensitivity, good reversibility, cost-effective, and fast response time. Nevertheless, poor selectivity performance and the requirement of high operating temperatures hinder the application of MOS sensor.

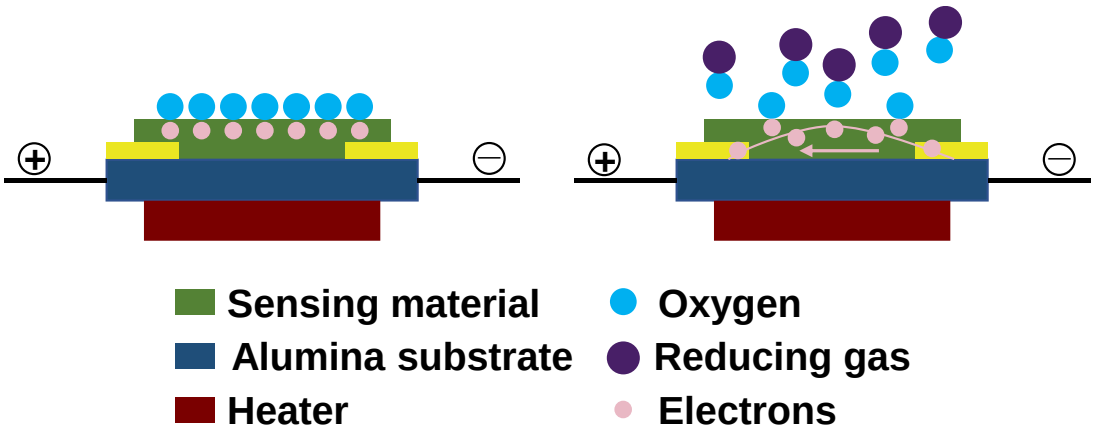

Fig. 1. 2. Schematic diagram of MOS sensor.

1.2.2.2 Gravimetric sensors

The gas's mass can be utilized for its detection. Quartz crystal microbalance (QCM) sensor are commonly used for as gravimetric sensor. When the mass on the crystal's surface changes (like deposition of gases or liquids), the crystal's resonant frequency shifts, allowing for highly sensitive detection and measurement of these mass changes.

Because QCM sensors solely measure gases based on mass, their selectivity is quite poor. However, their selectivity can be enhanced by coating gas-sensitive materials onto the sensor surface. A wide range of sensing materials have been used in QCM sensors, involving polymers [19, 20], metal oxides [21-23], carbon nanotubes [24], and molecularly imprinted polymer [25]. QCM sensor offers advantages such as fast response time, high sensitivity, low cost, and operation at room temperature [26]. However, the detection accuracy is easily affected by the humidity, and preparation of the gas sensing material is required.

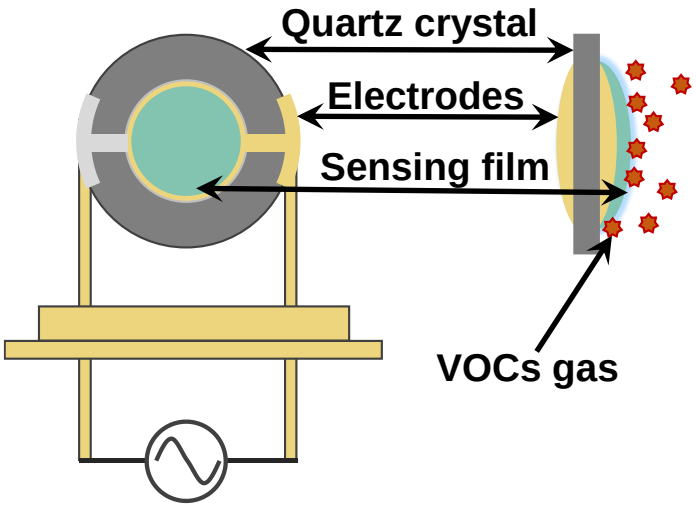

Fig. 1. 3. Gas detected by the QCM sensor.

1.2.2.3 Optical sensors

Most optical sensors are developed to detect gas analytes through direct and indicator-mediated methods [1]. In direct method, the intrinsic optical signals of the gas analytes are collected, such as non-dispersive infrared (NDIR) and Fourier transform infrared (FTIR) sensors. In indicator-mediated sensing methods, changes in the optical response of the indicator are utilized to monitor the presence and concentration of gas analytes. The representative sensors fabricated using this approach are colorimetric and fluorescent sensors.

The NDIR gas sensor analyzes the change in the intensity of the infrared spectrum before and after the adsorption of target gas molecules to identify and quantify the gases present in their surroundings. The NDIR gas sensor-based detection system consists of a light source, sample cell or gas chamber, and a detector. A wide range of gas can be detected using NDIR gas sensor, such as CO [27], carbon dioxide (CO_2) [28], NO_X [29], ammonia (NH_3) [30], and hydrogen chloride (HCl) [31]. The NDIR sensor demonstrates excellent sensitivity and selectivity, along with low power consumption and fast

response time. Nonetheless, challenges remain regarding the device's bulkiness, overlapping gas spectra, and the detection limit for specific target gases [30].

Colorimetric sensors detect gas analytes by observing changes in the sensor's color. This color alteration occurs due to strong chemical interactions between the gas analytes and the sensing materials as shown in Fig.1. 4 [32, 33]. The detection result can be easily observed with the naked eye due to the noticeable color change. For quantitative detection, the three-channel visible range (red, green, blue) obtained with a camera can be used to measure the concentration of the gas analyte. Colorimetric sensors provide high sensitivity often down to parts per billion (ppb) [34] or even parts per trillion (ppt) levels [35]. Until now, a variety of sensing materials are used to fabricate colorimetric gas sensors according to the types of intermolecular interactions, including basic dyes, base dyes, redox dyes, colorants with large permanent dipoles, and chromogenic aggregative materials [36]. The main drawback of colorimetric sensors is their lack of reversibility. Nevertheless, this sensor provides various advantages include cost-effectiveness, portability, and high sensitivity. These attributes have led to their application in various fields such as environmental monitoring [37], food safety [32, 38], and healthcare [39-41].

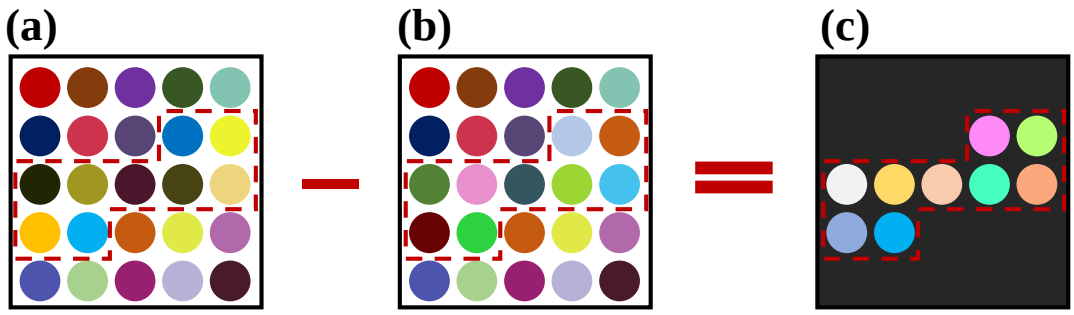

Fig. 1. 4. The colorimetric sensors for gas detection. The color image of the colorimetric sensors (a) before and (b) after gas exposure, as well as the (c) differential image.

The fluorescent sensor, created with fluorescent probes, is another typical optical sensor utilized in gas detection [36, 42]. Its fluorescence emission spectra change upon interacting with gas analytes. Fluorescent sensors provide a range of significant measurement parameters like fluorescence intensity, anisotropy, lifetime, emission and excitation spectra, fluorescence decay, and quantum yield, which are essential for comprehensive data analysis [43, 44]. Fluorescent sensors combined with organic frameworks [45, 46], polymers [47], and small molecules [48] have been developed to detect VOC gas. Fluorescent sensors boast wide-ranging applications because of their

operational simplicity, superior selectivity, and high sensitivity [42, 49]. Furthermore, analyzing the detection results from the fluorescent sensor allows for visualizing the analytes [42, 50]. However, fluorescent sensors have drawbacks, including the requirement for specific probes tailored to target gases, which may also present toxicity concerns [51].

1.2.3 Electronic-nose

An electronic nose (E-nose) is a portable device designed to mimic the human olfactory system's ability to detect and recognize odors or gases [52, 53]. The e-nose comprises cross-sensitive sensor arrays, akin to human olfactory bulbs, which react to diverse chemical components present in an odor or gas mixture, producing specific fingerprint data. Pattern recognition algorithms, similar to those in the brain olfactory cortex, then analyze this data to identify distinct odors or assess gas mixtures [54]. The sensor array in an e-nose comprises multiple gas sensors modified with diverse sensing materials. The interactions between the gas analytes and sensing materials cause changes that are then converted into electrical signals, allowing the acquisition of a fingerprint response to the detected gases. Common types of gas sensors used in e-nose systems include MOS, QCM, conducting polymers, and colorimetric sensors [55]. Pattern recognition algorithms are utilized to process the signals acquired from the sensor array, allowing for the recognition and classification of different gas samples. To date, two types of recognition algorithms have been developed [53, 54]: classical (e.g. principal component analysis [56], linear discriminant analysis [57], decision tree [58], support vector machine [59], and K-nearest neighbor [60]) and artificial intelligence-based methods (e.g. multilayer perceptron [61], extreme learning machines [62], and convolutional neural network [63]). The high-dimensional detection results, along with pattern recognition algorithms, facilitate accurate gas sample recognition. Additionally, the integration of gas sensors within the e-nose system contributes to rapid analysis, cost-effectiveness, and portability. These e-nose advantages enable extensive applications, including food quality assessment [64], environmental monitoring [65], and breath analysis [66, 67]. The limitations of e-nose include three main aspects: lack of long-term stability , high energy demands, and difficulties in handling variations in sensor response using existing recognition algorithms [54, 55, 68].

1.3 Surface enhanced Raman scattering (SERS)

Surface-enhanced Raman scattering (SERS) has been developed as an efficient sensing technique by enhancing the Raman scatting of the molecules adsorbed onto

rough metal surfaces, such as silver or gold nanoparticles (NPs) [69-71]. When a laser interacts with a molecule, the inelastic scattering light at different frequencies compared to the incident laser is known as Raman scattering. Raman scatting provides vibrational and rotational information about the molecule, which can be used to recognize the molecule's species. Enhancing the low-intensity Raman scattering is crucial for practical applications. In 1974, Fleischman et.al first reported the enhanced Raman scattering from pyridine absorbed on a roughened silver electron [72]. In 1977, Jeanmaire and Van Duyne recognized that the increased signal could be explained by the electromagnetic mechanism (EM) at metal surfaces [73]. In the same year, Albrecht and Creighton proposed that enhance signal originates from the chemical mechanism (CM), arising due to the formation of a charge-transfer complex between molecules and metal substrate [74]. These two processes are considered as the fundamental enhancement factors (EF) to the SERS effect [69], represented as follows:

$$P_r = \alpha E$$

where P_r is the induced polarization of Raman scattering, α is the Raman polarizability of the electrons in the molecule, and E is the applied electric fields. In Raman scattering, the incoming light interacts with the molecule, inducing polarization as it couples with the molecule's vibrations. This alters the molecule's dipole moment, causing the scattered light's frequency to differ from the incident light's frequency [75].

The EM is primarily based on the enhancement through the strong local electromagnetic field in the near field of the surface of plasmonic nanostructures, such as silver or gold nanoparticles. When metal nanostructures are exposed to incident light (E), the conductive electrons undergo collective oscillations, creating an electromagnetic field around the interface formed by the metal nanostructure and the dielectric environment. If the frequency of the incident light (w) resonates with the frequency of electron oscillation, it induces localized surface plasmon resonance (LSPR) on the metal surface. LSPR results in a substantial enhancement of the local electromagnetic field around the nanoparticles, generating intense "hot spots" due to the coupled plasmons between two adjacent NPs [75]. On the other hand, the CM involves interactions between the adsorbed molecules and the metal surface leading to the formation of chemical complexation, or charge transfer and charge transfer resonance [76, 77]. These results can enhance the polarizability of the molecule, thus increasing the Raman intensity. The Raman intensity enhanced factors (EFs) originating from the CM typically range from 10 to 10^2, which is considerably lower than the contribution from the EM mechanism, reaching values as high as 10^5 to 10^9 [78, 79]. Consequently, the Raman intensity of the molecule undergoes a significant enhancement when it enters

the hot spot.

SERS sensors have been emerged as a novel VOC gas sensing technique in various applications, such as environmental monitoring [80], food quality [81], and disease diagnose [82-84]. The SERS gas sensor possesses four main merits that drive its applications: (i) Molecular-level high sensitivity, enabling detection of gases at concentrations as low as ppb [85, 86]; (ii) Rapid detection, providing results as soon as the analyte adsorbs on the surface of the SERS sensor [87]; (iii) Multiplexing capability, achieving the recognition of multiplex gas analytes based on their Raman spectra fingerprint [88]; and (iv) label-free detection, allowing gas analytes to be detected without probes [89]. However, the SERS sensor for gas sensing still have some limitations, including the poor affinity of diffuse gas molecules to the sensor surface and the weak Raman scattering of certain gas analytes. To address these issues, modifying the SERS sensor with nonporous materials or employing gas capture probes can offer solutions [80, 86, 90].

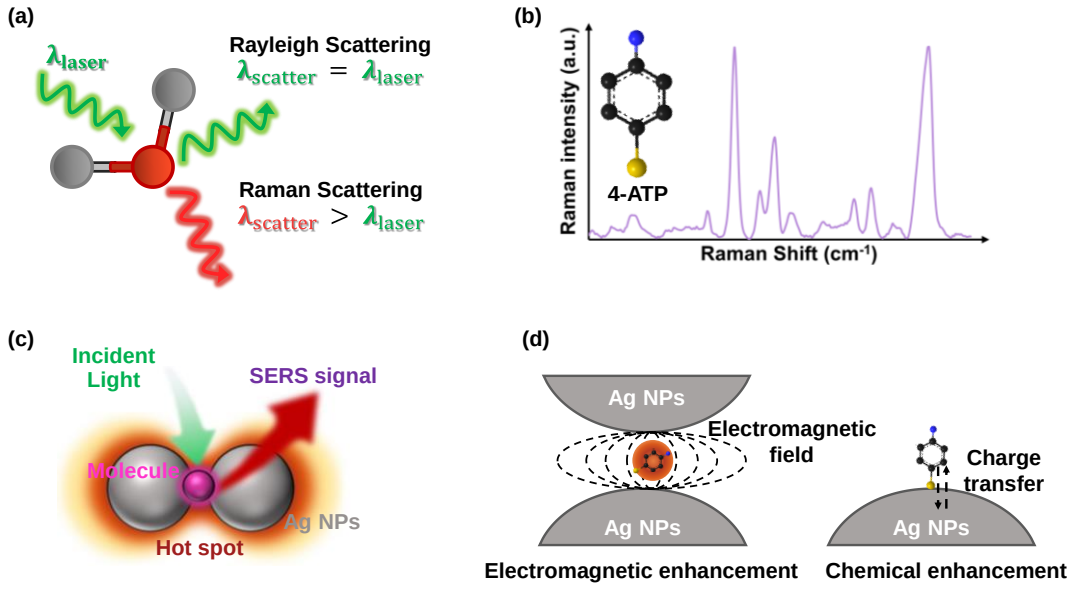

Fig. 1. 5. (a) The schematic diagram of the Raman scattering. (b) The Raman spectra depicting the vibrational modes of the 4-aminothiophenol (4-ATP) molecule. (c) The schematic diagram of the Raman signal enhanced by surface enhanced Raman scattering (SERS) technology. (d) The illustration of the electromagnetic enhancement and chemical enhancement mechanism in SERS [75, 77].

1.4 Fabrication of the SERS sensor

A SERS sensor is developed by depositing orderly arranged metallic nanopatterns on a substrate, enabling the formation of hotspots between the nanoparticles to enhance the Raman signals of the detected analytes. The noble metal elements gold (Au) and silver (Ag) are commonly utilized to fabricate SERS sensors because they can induce a strong LSPR effect [91-93]. The two primary methods for fabricating SERS-based sensors are top-down ordered lithographic fabrication (physical fabrication method) and the facile bottom-up self-assembly-driven approach (chemical fabrication method). The SERS sensor is prepared using lithographic methods in a two-step process: creating a distance-adjustment ($d < 10$ nm) nanopattern on the substrate and depositing metal nanoparticles onto the patterned substrate [71]. Lithographic methods allow SERS sensors with various structural features (geometry, size, and gaps) to be fabricated, so the SERS substrates often have high sensitivities and give reproducible results [91, 94, 95]. However, top-down lithographic fabrication is time consuming and requires expensive equipment [71]. The self-assembly method, utilizing chemical synthesis techniques, is relatively inexpensive and has been primarily employed to synthesize Au and Ag NPs. A SERS sensor can be fabricated by employing a self-assembled method to create an aligned and packed array on a supporting substrate [96-99]. The morphologies and interparticle gaps within uniformly self-assembled NPs can be controlled using various synthetic methods, resulting in excellent SERS sensors [100-103]. However, great experience in chemical synthesis is required to produce NPs. The SERS sensors produced by these two methods have their respective merits and drawbacks, thus requiring a trade-off selection based on the specific requirements of the application.

1.5 Motivation and objectives

To detect and identify multiple VOC with similar molecular structures, exploring and developing an easily fabricated and high-sensitivity SERS gas sensor is essential. Furthermore, visualizing the spatial distribution of gases based on SERS identification results can be used to localize the odor source. Hence, this study aims to achieve three main objectives:

(1) Develop a high-sensitivity SERS sensor with an adsorption concentrating method for the detection of ultra-low concentration.
(2) Enhance the selectivity of the SERS gas sensor by spin-coating functional materials onto the sensor.
(3) Visualize the spatial distribution of the VOC gas evaporating from the odor sources.

1.6 Outline of dissertation

The dissertation outline is presented as follows:

In Chapter 1, the study's background is introduced. The significance of the VOC gas detection and the current gas sensor technology are explained. Following this, the novel SERS gas sensing approach, and the method of fabricating the SERS sensor are introduced. Lastly, the motivation and objectives of this dissertation are presented.

In Chapter 2, a highly sensitive SERS sensor was developed using an adsorption concentrating method to detect ultra-low concentration of geosmin. The geosmin solution was heated using a water bath, generating gas through a bubbling method, which was then adsorbed onto the sensor surface and detected.

In Chapter 3, SERS gas sensors coated with functional polymer film was fabricated to differentiate between three types of VOC gases with similar molecular structures. The sensor's selectivity was tailored using various functional polymer films. Ultimately, the principal component analysis (PCA) algorithm was applied to identify these VOC gases by analyzing their Raman intensities.

In chapter 4, a two-dimensional (2D) SERS gas sensor array was constructed to identify and visualize the spatial distribution of gases evaporating from the odor sources. SERS spectra of the gases at various positions across the SERS sensor array were acquired by scanning its surface while placed above the odor source. The intensity values of selected characteristic peaks at each point were used to generate a heatmap image for visualizing the spatial distribution of gases. From the visualization results, the changing status of the spatial distribution of gases over time was prominently observable. To identify and visualize two distinct odor sources, the non-negative matrix factorization algorithm was applied to analyze the obtained SERS spectra matrix. The outcomes of this analysis were used to identify the gas odor sources and visualize their spatial distributions.

In chapter 5, the experimental results are summarized, and the potential future research avenues are proposed.

Chapter 2

2. SERS sensor for ultra-low detection with an adsorption concentrating method

2.1 Introduction

2-methylisoborneol (MIB) and geosmin (GSM) produced by a variety of microorganisms have been identified as being responsible for the earthy and musty taste and odor of drinking water [104]. In healthy drinking water, the concentration of MIB and GSM are regulated to less than 10 ppt (part per trillion). In general, the analysis of GSM is carried out using GC-MS methods [105]. Despite the high detection limits in GS-MS analysis, the process demands expensive equipment and is time-consuming in the pre-treatment procedure. Therefore, the development of a faster and portable sensing system for detecting water samples outside the laboratory setting is essential [106, 107]. SERS techniques offer a single-molecule level and direct detection approach that enables the rapid analysis of gas chemical molecules based on their unique vibrational fingerprints [108, 109]. Consequently, a high-sensitivity SERS gas senor was developed to detect ultra-low concentrations of GSM in water [110].

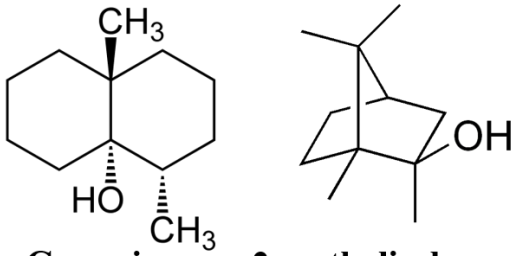

Fig. 2. 1. Chemical structure of 2-methylisoborneol and geosmin.

As described in the section 1.3, the SERS sensor possess high sensitivity when chemical substances exist in the hot spot between two adjacent NPs [111, 112]. However, it's challenging for small-molecule gases to be absorbed on the solid SERS sensor due to its greater diffusion coefficient and affinity with the sensor [113, 114]. Here, a SERS sensor combined with an adsorption concentrating method has been developed to transform liquid analytes into gaseous form, allowing adsorption and

concentration of the analytes on the surface of SERS sensor for ultra-low concentration detection. In detail, the SERS sensor was modified with 3-Methoxybutyl 3-Mercaptopropionate, whose thiol group could establish a coordination bond with silver. The polar function group made the SERS sensor hydrophilic, enriching the adsorption of GSM present in water vapor on the sensor (Fig. 2. 2). Using this method, we transformed an aqueous GSM solution into gas, achieving the detection of a 10 ppt GSM solution with a calculated limit of detection of 5.4 ppt.

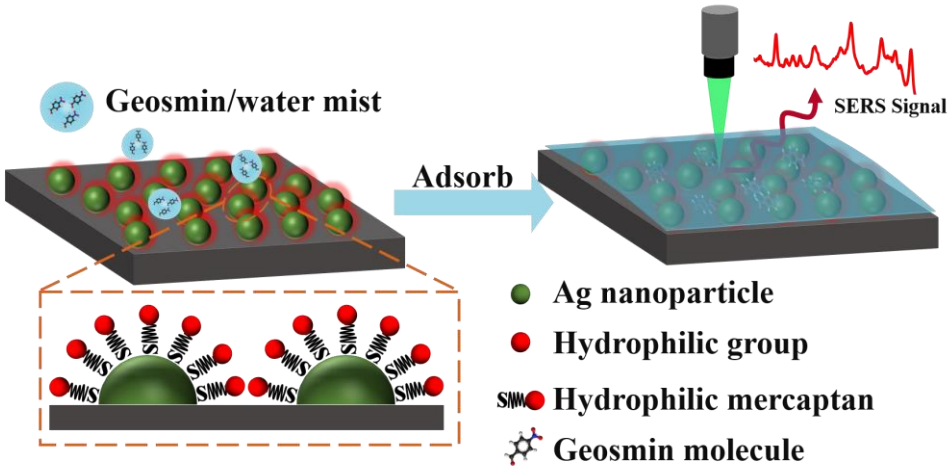

Fig. 2. 2. The schematic diagram of geosmin detection using a SERS gas sensor modified with a hydrophilic chemical probe.

2.2 Materials and methods

2.2.1 Materials

RandaS SERS sensor was purchased from ATOID CO. (Japan). Hydrophilic 3-Methoxybutyl 3-Mercaptopropionate (Tokyo Chemical Industry CO., LTD., Japan) and hydrophobic 1-Octanethiol (Fujifilm Wako Pure Chemical Corporation, Japan) were employed as modifiers to change the polarity of the SERS sensor. Standard GSM (Sigma-Aldrich, America) was diluted by ultrapure water and tap water from laboratory to different concentration (10 ppb, 1 ppb, 100 ppt, 10 ppt).

2.2.2 Formation of geosmin mist

GSM gas was generated from a GSM solution using the bubbling method, while the solution's temperature was controlled via a water bath heating technique. GSM mist formed when the hot GSM gas contacted the cold SERS sensor. As the mist accumulated, a thin water film containing GSM appeared on the surface of the SERS

sensor, as shown in Fig.2. 3.

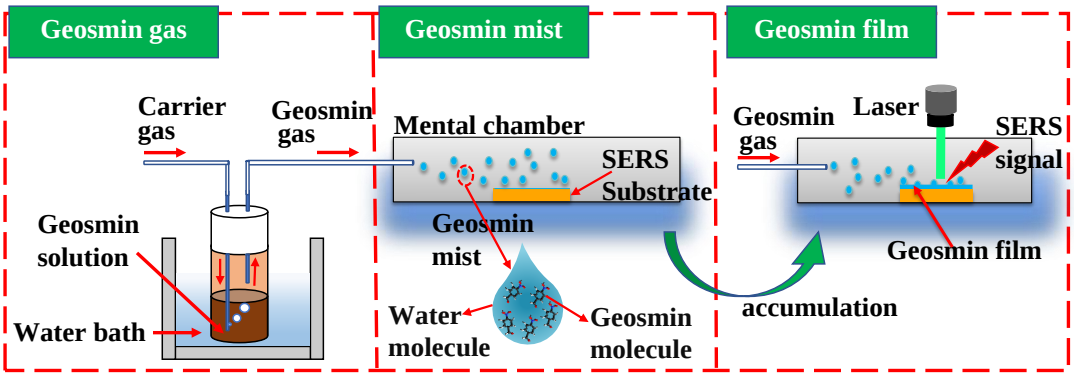

Fig. 2. 3. The process of the generation of the geosmin mist.

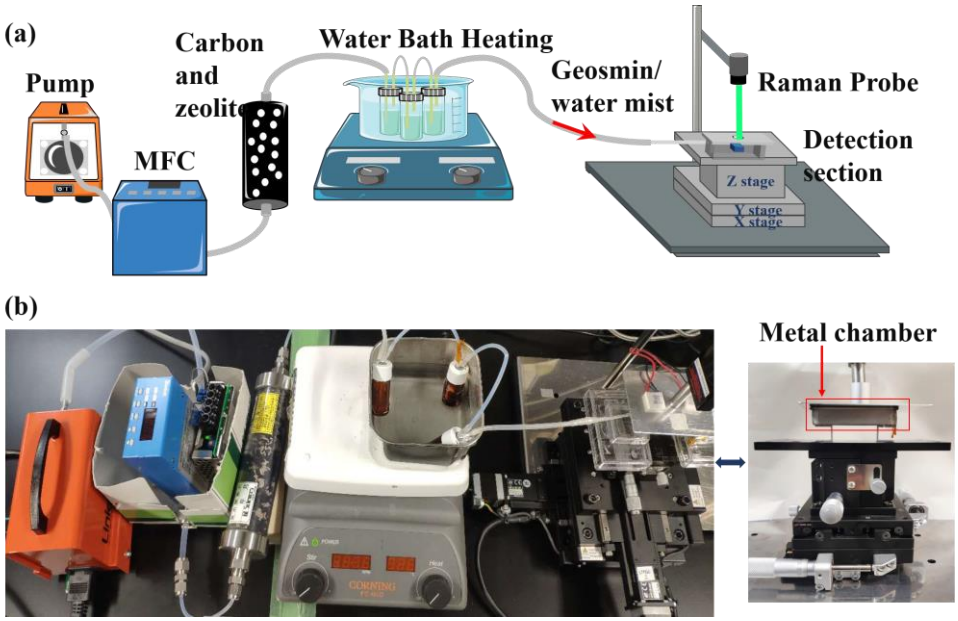

Fig. 2. 4. (a) The schematic diagram and (b) picture of gasification detection system.

2.2.3 Gasification and detection system

As depicted in Fig. 2. 4a and b, GSM solution was added to three small bottles, generating GSM gas through the bubbling method, and subsequently detected within the detection set. The temperature of GSM solution was maintained using a water bath heating method through a hot plate. The gas flow rate was set at 100 ml/min using the mass flow controller (MFC) (KOFLOC Kyoto, Japan). Within the detection set, a commercially available RandaS SERS sensor with Ag nanostructure was utilized. A metallic chamber was designed to prevent laser leakage and the absorption of external light. Additionally, it hindered gas absorption on its inner wall. A computer-controlled automatic mobile stage was devised for convenient adjustment of the laser focus and

irradiation position. SERS measurements were conducted using a Raman spectrometer (AvaRaman, Avantes, Japan) with a 532 nm laser. The laser exposure time was set to 5 seconds, and the average number of calculations was 12 times.

2.2.4 Modification of SERS substrate

To start, the SERS sensor underwent a series of washes with acetone, water, and ethanol. Subsequently, the substrate was immersed in a 3-Methoxybutyl 3-Mercaptopropionate ethanol solution to fabricate the hydrophilic sensor and a 1-Octanethiol ethanol solution to fabricate the hydrophobic sensor for 20 minutes. Finally, the sensor was dried using a nitrogen flow.

2.3 Results and discussions

2.3.1 SERS spectrum for determining geosmin gas

At first, a 10 μL droplet of GSM standard solution was deposited onto the SERS sensor using a pipette and allowed to dry in the ambient environment. Subsequently, the SERS spectrum of GSM was recorded. Following this, gas generated by the gasification system was introduced from a 100-ppm concentration GSM solution to the surface of the bare SERS sensor located in the chamber. By comparing the two spectra, as illustrated in Fig. 2. 5, the characteristic peaks of GSM at 672 cm^{-1}, 805 cm^{-1}, and 1006 cm^{-1} were determined.

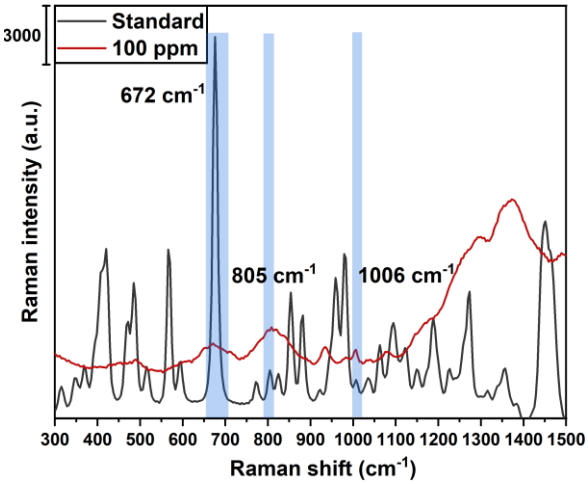

Fig. 2. 5. Comparation of standard and 100 ppm geosmin solution.

2.3.2 Temperature determination of water bath heating

Heating the liquid analyte makes it easier to generate gas. Additionally, increasing the temperature difference between the gas and the sensor allows mist to form more

rapidly on the sensor surface. The heating temperature was regulated using water bath heating, and three small bottles containing the GSM solution were connected in series to enhance gas production (Fig. 2. 4b.).

In this study, the gas generation time is a crucial factor influencing GSM detection. Our focus was on observing variations in sensitivity over time, particularly while heating a 10 ppb GSM solution at 80°C. The SERS spectra of GSM were acquired at different time intervals on the same spots, as depicted in the Fig. 2. 6a. The SERS intensities of the characteristic peaks at 672 cm^{-1} were utilized as quantitative analysis standards for GSM. The SERS intensity was calculated as the difference between the peak and valley value of the characteristic peak. In Fig. 2. 6b, the SERS intensity increased before 10 minutes and subsequently decreased between 1 and 34 minutes. During the aeration process, gas gradually accumulated on the sensor, forming a thin water film due to the warm GSM gas adhered to the cooler sensor. This resulted in

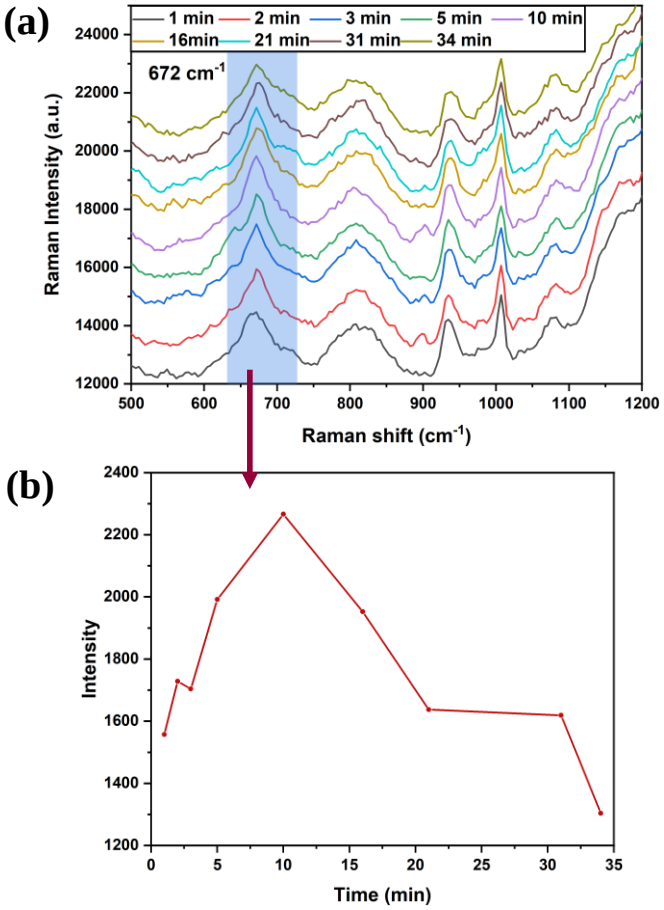

Fig. 2. 6. (a) The SRES spectra and (b) change of SERS intensity at 672cm^{-1} with time when 10 ppb geosmin was detected at 80 ℃.

an initial increase in SERS intensity. However, as an excessive amount of gas attached to the sensor, the thin water film transformed into water droplets. Our hypothesis suggested that these water droplets might hinder the entry of GSM molecules into the hotspots, consequently leading to a decline in SERS sensitivity.

Subsequently, we explored the correlation between heating temperature and the SERS sensor's detection sensitivity. At temperatures ranging from 40 °C to 80 °C, we detect the same concentration (10 ppb) of GSM solution, and the intensities of the three distinctive peaks were calculated as indicated in Fig. 2.7. The greatest SERS intensity at the same temperature was 805 cm^{-1}, while the intensity at 672 cm^{-1} was the second highest. Furthermore, the SERS intensity exhibited an upward trend with increasing heating temperature. While SERS intensity continued to rise beyond 80 ℃, such high temperatures might be dangerous and consume excessive energy in practical applications. Consequently, for the subsequent experiments, we chose 40 ℃ or 50 ℃ as the heating condition. Additionally, the distinctive peak at 805 cm^{-1} might be interfered by the SERS sensor's fixed Raman shift (820 cm^{-1}). Thus, the Raman shift at 672 cm^{-1} was taken into consideration as the characteristic peak of GSM. Upon closer inspection, at a heating temperature of 50°C, compared to 40°C, the average intensity values showed a slight increase and the standard deviation slightly decreased. Furthermore, 50°C was found to be more favorable for the volatilization of GSM from water. Hence, we ultimately selected a heating temperature of 50°C for subsequent experiments.

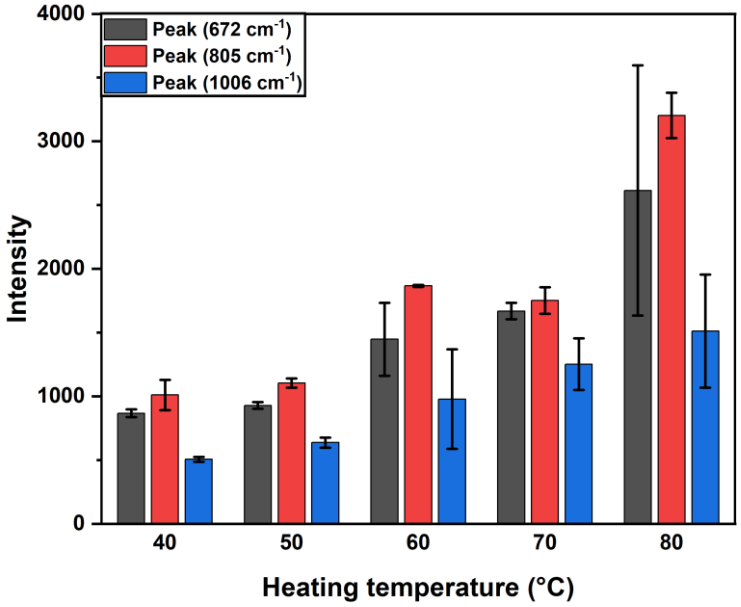

Fig. 2. 7. The average intensity of three characteristic Raman peaks varied at different temperatures.

2.3.3 Influence of hydrophilic and hydrophobic sensors on GSM detection

As discussed earlier, carrier gas transported GSM and water molecules from the sample solution, leading to the formation of a water mist on the sensor. To improve the sensor's ability to detect lower concentrations, the hydrophobic SERS sensor was modified to become hydrophilic. This modification involved the use of 3-Methoxybutyl 3-Mercaptopropionate to impart hydrophilicity to the substrate, while 1-Octanethiol was chosen to maintain its hydrophobic nature. Thiol groups, which form strong coordination bonds with silver, allowed these two selected thiol compounds to attach to the sensor through an immersion method. The -COO functional group of 3-Methoxybutyl 3-Mercaptopropionate was hydrophilic, while the -CH3 functional group of 1-Octanethiol was hydrophobic. Consequently, the hydrophilic sensor was expected to attract more GSM molecules that coexisted with water molecules.

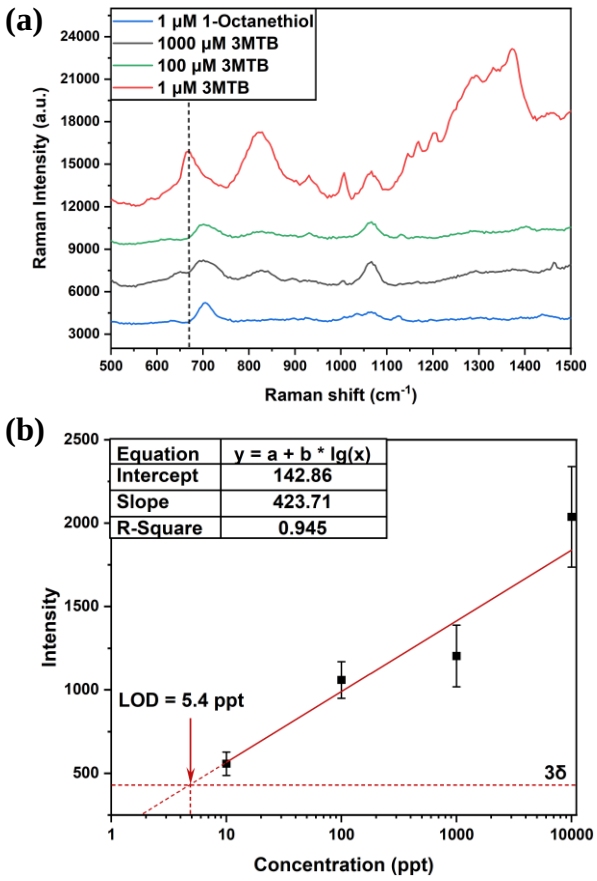

Fig. 2. 8. (a) SERS spectra of geosmin tested by hydrophilic and hydrophobic substrate and (b) Detection range of SERS substrate modified by 3-Methoxybutyl 3-Mercaptopropionate (3MTB).

In the subsequent experiment, we determined the optimal concentration of the

modified sulfide solution. As shown in Fig. 2. 8a, when 1-Octanethiol was used as the modifier, no Raman peak of GSM was observed. This difficulty for the hydrophobic sensor to adsorb water molecules containing GSM led to the absence of the SERS signal. Moreover, the characteristic peak at 672 cm^{-1} was detected only at a modifier concentration of 1 μM. This observation could be explained by the formation of a thick film on the substrate when a high-concentration solution was used, thereby hindering GSM from reaching the hotspots of the SERS sensor.

Gas sensitivity was assessed using the hydrophilic substrate in Fig. 2.8b. The detection limit was determined to be 10 ppt, with a detection range spanning from 0.01 ppb to 10 ppb. Notably, the logarithm of GSM concentration displayed a strong linear relationship with the SERS intensity, showcasing a high correlation coefficient of 0.945. In the collected SERS spectra under conditions without GSM detection, data within the Raman shifts between 549 cm^{-1} and 959 cm^{-1} were selected. The average and standard deviation were calculated for this selected range. The noise intensity value was determined by adding three times the standard deviation to the average value. This value was then used as the limit of detection. Furthermore, the limit of detection (3δ) for GSM in ultrapure water was calculated to be 5.4 ppt.

2.3.4 Detection of geosmin in tap water

To validate the practicality of our proposed detection system, we employed laboratory tap water to directly dilute the standard GSM solution into various concentrations. Employing the previously described detection method, we acquired the SERS spectra of GSM gas at various concentrations, and the detection results were presented in Fig. 2.9a.

The lowest detectable limit for GSM in this experiment was determined to be 100 ppt. When compared to GSM diluted in ultrapure water at the same concentration, the SERS intensity at 672 cm^{-1} was lower. This difference could be attributed to the presence of other particles in untreated tap water, which might have affected the adsorption of GSM molecules on the sensor. Despite this, GSM could still be distinguished based on its unique SERS spectra. However, for chemicals with similar SERS peaks, additional filtration might be necessary.

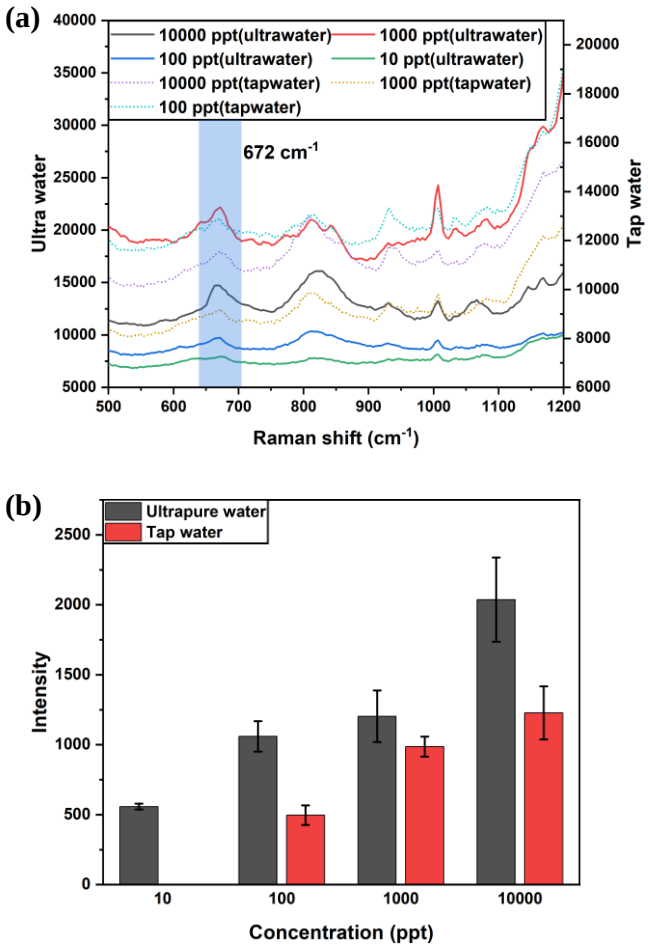

Fig. 2. 9. Comparation of (a) SERS spectra and (b) SERS intensity at 672 cm^{-1} of various geosmin solutions diluted in tap water and ultrapure water.

2.4 Conclusions

In this chapter, a high-sensitivity SERS gas sensor modified with chemical probes, combined with an adsorption concentrating method, was developed to concentrate and adsorb GSM onto the sensor surface, thereby achieving ultra-low concentration detection of GSM. To convert the GSM solution into gas, a gasification and detection system was constructed. The water bath heating method was utilized to facilitate gas generation easily. Under a 50 ℃ heating condition, a concentration as low as 10 ppt of GSM became detectable by the hydrophilic SERS sensor. Moreover, a strong linear relationship between concentration and SERS intensity was established. Additionally, this detection system successfully identified a concentration of 100 ppt of GSM in tap water.

Chapter 3

3. Gas recognition using multiple polymer film

3.1 Introduction

In a SERS spectrum, rich fingerprint information regarding the unique vibration frequencies of molecule is provided. Consequently, processing the specific SERS spectrum proves suitable for effectively accomplishing the classification and recognition of VOC gas samples. However, there is a challenge to recognize gas samples with similar molecular structures, whose characteristic peaks may overlap in SERS spectra. The primary aim of this chapter was to enhance the selectivity of SERS gas sensor in this detection situation. The easily-prepared polymer materials are commonly utilized in gas sensor devices because of their chemical and physical properties [115, 116].

In this chapter, the gas affinities of the SERS sensor array were changed by spin-coating distinct functional polymer films for recognizing different VOC gases with similar structures (Fig 3.1). The fabricated polymer film was employed to impede the contact of low-affinity gases with the SERS sensor, while permitting high-affinity gases to pass through the polymer film and reach the sensor surface. Three plant-based essential oil molecules, namely phenethyl alcohol, acetophenone, and anethole, were chosen as target gases due to their similar structure. Three distinct polymers, Poly(acrylic acid) (PAA), Poly(methyl methacrylate) (PMMA), and Polydimethylsiloxane (PDMS), each possessing different molecular structures and functional groups, were employed as sensing films. On a SERS sensor, single-layer or double-layer film was prepared using the spin-coated method. The double-layer film, characterized by high design flexibility, was fabricated using the layer-by-layer method. Upon detecting the three gases with sensors coated with different polymer films, diverse gas responses were observed. A response matrix, constructed using SERS intensities of the target gases, underwent processing through PCA algorithm. The characteristic variables of response matrix were adjusted by utilizing SERS intensity data collected from different sensors, aiming to optimize the performance of gas recognition.

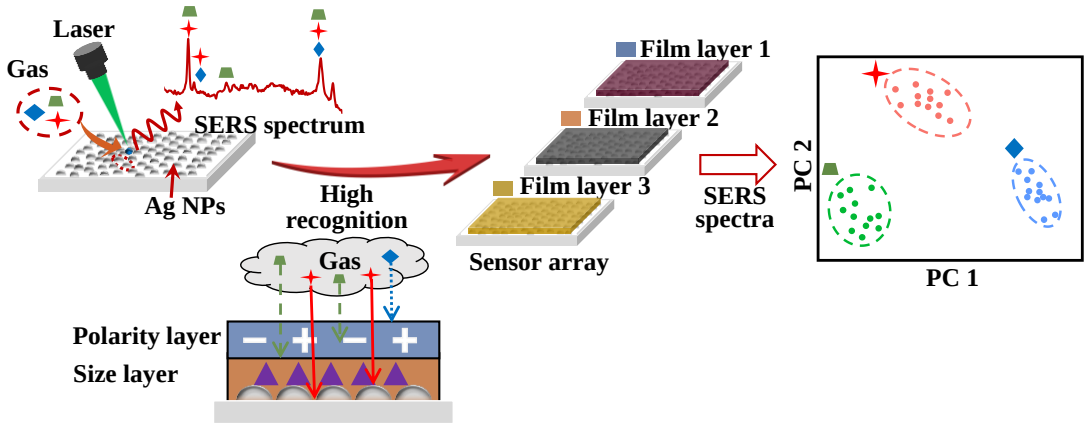

Fig. 3. 1. The schematic diagram of a SERS gas sensor coated with the polymer film array for gas recognition.

3.2 Materials and methods

3.2.1 Materials and instrumentation

Phenethyl alcohol was acquired from Kanto Chemical CO., INC. (Tokyo, Japan), while anethole was obtained from Nacalai TESQUE, INC. (Tokyoto, Japan). Acetophenone, ethanol, PAA, PMMA, hexane, and chloroform were purchased from Wako Pure Chemical Industries CO., Ltd. (Osaka, Japan). PDMS was acquired from Shin-Etsu Chemical CO., INC. (Tokyo, Japan). All reagents were used as received. The supplier of the RandaS SERS sensor was ATOID CO. (Japan). Polymer film coated on SERS sensor was analyzed using Fourier transform infrared spectroscopy (FT/IR-6800, Jasco, Japan). To image sensor morphologies, scanning electron microscopy (SEM, SU8000, Hitachi, Japan) was employed. Using a 532 nm excitation laser as the light source (power = 1.5 mW), a Raman spectrometer (AvaRaman, Avantes, Japan) was used to collect the Raman spectra. The accumulation time was set to 10 seconds for data collection.

3.2.2 Fabrication of polymer-coater SERS sensor

First, we prepared three polymer (PAA, PMMA, PDMS) solutions. PAA (30 mg) was dissolved in 16 mL of ethanol, PMMA (30 mg) was dissolved in 16 mL of chloroform, and PDMS (2 mg) was dissolved in 16 mL of hexane. The polymer solutions were thoroughly stirred prior to utilization.

Next, the SERS sensor was spin-coated with these prepared polymer solutions. The SERS sensor was cleaned by sequential immersion in acetone, ethanol, and ultrapure water, followed by drying with a nitrogen stream. The bare SERS sensor without spin-

coated polymer film served as a reference. For the fabrication of single-layer polymer film-coated SERS sensor, 15 μL of polymer solution was spin-coated onto the SERS sensor and then dried under vacuum conditions. The spin-coating process involved spinning at 500 rpm for 20 s, a slope of 500 rpm to 3000 rpm for 10 s, and then 3000 rpm for 30 s. In case of double-layer polymer film-coated SERS sensors, the layer-by-layer method was employed. The first polymer film was prepared on the cleaned SERS sensor, and after drying, the second polymer film was spin-coated onto the surface.

3.2.3 Gas generation and detection system

The gas generation and detection system schematic are illustrated in Fig. 3. 2. An air pump produced carrier gas with a flow rate of 0.1 mL/min, regulated by an MFC. A gas cleaning filter, containing molecular sieve and zeolite, was placed between the MFC and a glass bottle containing the odorant (3 mL) to control humidity. The target gas was generated using the bubbling method and subsequently detected in a custom-made gas detector cell. The gas concentrations were calculated by [117]:

$$C = \frac{k \times D_r \times 10^3}{F} \qquad (1)$$

where F is the flow rate of the dilute air (0.1 L/min), Dr is the diffusion rate (mg/min), and k is the factor used to convert gas weight to volume, calculated by:

$$k = \frac{22.4 \times (273 + t) \times 760}{M \times 273 \times P} \qquad (2)$$

where t is the temperature in the gas detector cell (20 °C), M is the molecular weight, and P is the gas pressure (760 mmHg). The target gas concentrations for phenethyl alcohol, acetophenone, and anethole were determined to be 403.4, 510.2, and 623.7 ppm, respectively.

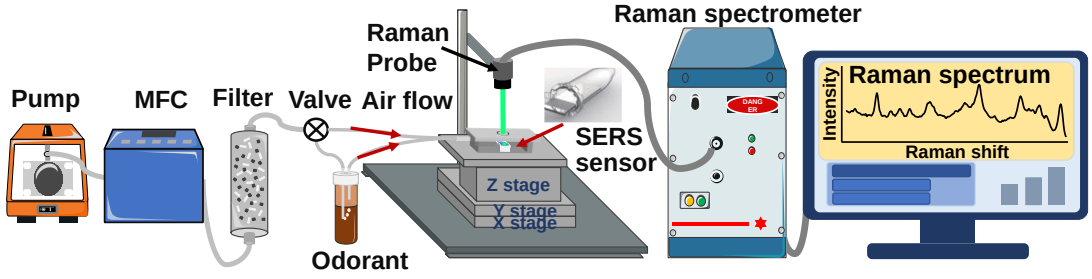

Fig. 3. 2. Schematics of gas generation and detection system.

An adjustable stage was manufactured to fine-tune the position and size of laser focused on the SERS gas sensor. The detection chamber was utilized to prevent laser leakage. SERS spectra of the three target gases were recorded following exposure of the

SERS gas sensor to each gas for a specific duration. Additionally, the gas detection cell underwent a 20-minute air flow wash after each gas detection.

3.3 Results and discussions

3.3.1 SERS spectra of the detected gases

The morphologies of the sensors were depicted in Fig. S3.1, where the size of Ag NPs was approximately 50 nm (Fig. S3.1a). Ag nanoparticles were observed to gather and form clusters, creating more hotspots. Because they all have a benzene ring in their chemical structure, phenethyl alcohol, acetophenone, and anethole were chosen as the target gases. A bare SERS sensor was used to get the SERS spectra of three target gases (Fig. 3. 3). For phenethyl alcohol and acetophenone, the characteristic peaks at 1007 cm^{-1} and 1604 cm^{-1} were attributed to ring breathing vibrational and ring stretching mode [118] (Fig. 3. 3a, b), respectively. In Fig. 3. 3c, benzene ring stretching vibration at 1604 cm^{-1}, C-O-C stretching vibration at 1175 cm^{-1} of anethole gas were clearly observed [119]. Although the main characteristic peaks of the target samples in gaseous and liquid states were similar (Fig. S3.2), the SERS intensities of the gases were weaker, possibly due to the challenge of gas adsorption on the surface of the bare SERS sensor.

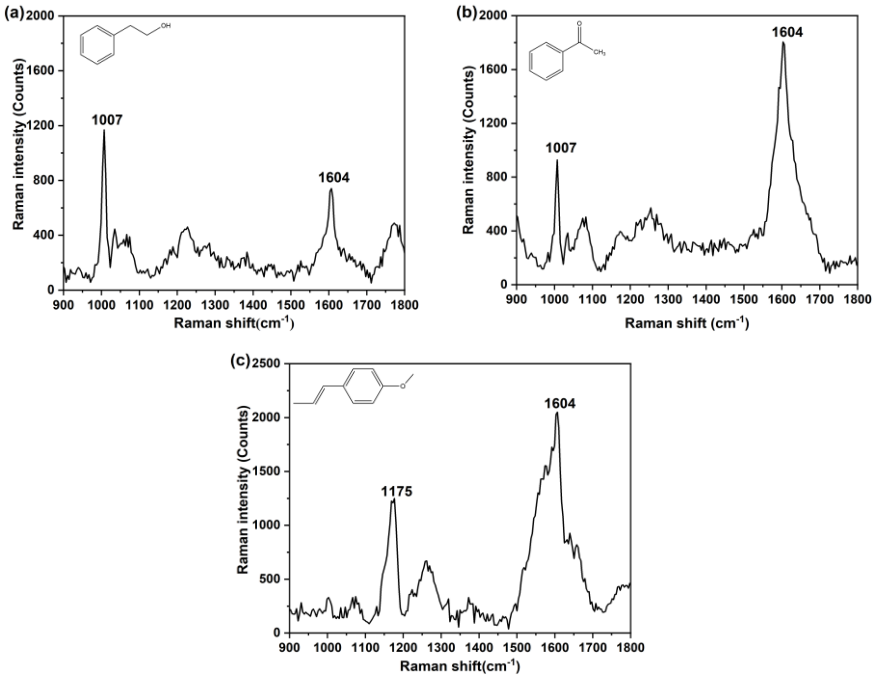

Fig. 3. 3. SERS spectra of (a) Phenethyl alcohol gas, (b) acetophenone gas and (c) anethole gas.

A distinct characteristic peak at 1175 cm^{-1} was identified, which could be used to differentiate anethole gas from acetophenone and phenethyl alcohol gases. However, two prominent peaks at 1007 cm^{-1} and 1604 cm^{-1} were observed in the SERS spectra of acetophenone and phenethyl alcohol gases. Consequently, distinguishing between these two target gases solely based on the peak positions was challenging.

3.3.2 FT-IR spectra of functional polymer film

Discriminating between acetophenone and phenethyl alcohol gases directly using SERS spectra collected by the bare SERS sensor becomes difficult due to the similarity of their distinctive peaks. However, it is commonly known that polymers exhibit distinct properties such as polarity, size, and molecular structure. Drawing inspiration from this, polymers were employed in the fabrication of gas sensors [115]. Herein, we proposed a method to alter the affinity of SERS gas sensor by constructing a polymer film on the sensor through the spin-coating method, aiming to differentiate gases with similar molecular structures.

As functional polymer films for gas sensors, three distinct types of polymers—, PAA [120], PMMA [121], and PDMS [122]—with varying molecular structures and polarity were used. In our designed SERS gas sensors, we leveraged these polymers. Moreover, we explored two types of functional polymer films: single-layer and double-layer polymer films. Specifically, the double-layer film was composed of two single-layer films fabricated using the layer-by-layer method. This approach enabled the realization of a functional double-layer polymer film with high design flexibility, achieved by selecting two different single-layer films based on the specific detection requirements. For a double-layer polymer film sensor, when polymer B was spin-coated onto polymer A, the sensor was referred to as an A-B SERS gas sensor. For example, a PDMS-PAA SERS gas sensor was created by spin-coating a PAA polymer film onto a PDMS film. The thickness of the prepared film layer in this work was less than 10 nm, following similar spin-coating conditions from our previous study [123]. In Fig. 3.4, FT-IR spectra were acquired using the reflection absorption spectroscopy method in the range of 800-3600 cm^{-1}, recorded for both single-layer and double-layer polymer films. Bending vibrations of PAA [124], PMMA [125], PDMS [126] polymers were confirmed with relative reference. In this experiment, we initially fabricated the first polymer film on the bare SERS sensor and then collect the FT-IR spectrum. Subsequently, the second polymer film was spin-coated on this sensor, and the FT-IR spectrum was recorded once again. The polymer films were attached to the SERS sensor based on the characteristic spectra. Additionally, we observed that only the bending vibration of the top polymer film appeared when a double-layer film SERS sensor was detected. This observation

indicated that the first polymer film layer was nearly completely covered by the top polymer film layer.

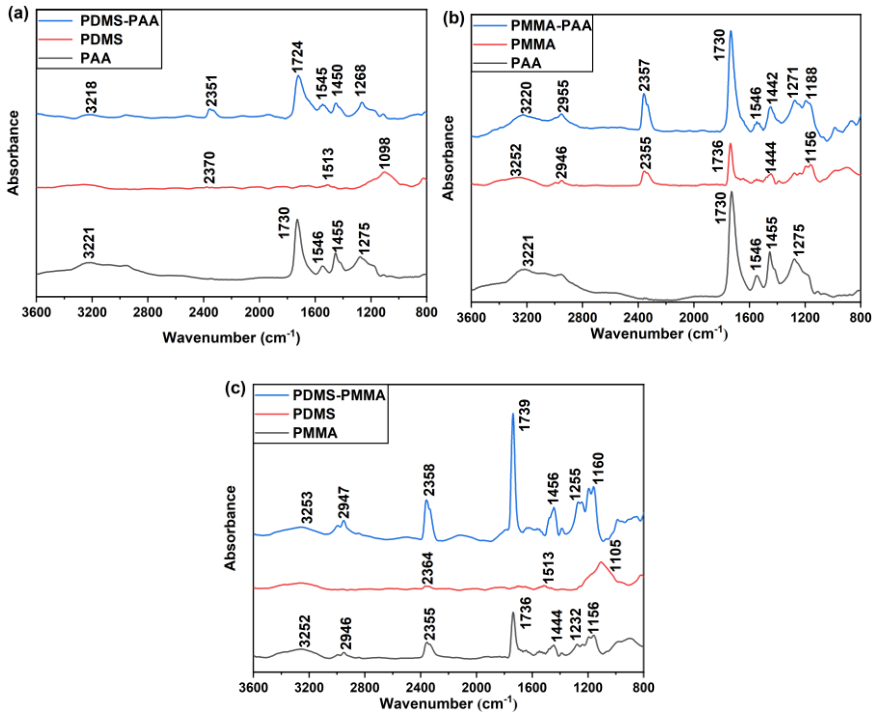

Fig. 3. 4. FT-IR spectra in the range 800-3600 cm^{-1} of SERS gas sensor coated by (a) PDMS-PAA, (b) PMMA-PAA and (c) PDMS-PMMA polymer film.

3.3.3 Sensitivity of polymer film coated SERS gas sensor

The background SERS spectra of the bare sensor and sensor coated with PAA, PMMA, and PDMS were presented in Fig. S3.3. No characteristic peaks at 1007 cm^{-1}, 1175 cm^{-1} or 1604 cm^{-1} were observed in the background SERS spectra. All SERS spectra in our result were obtained after subtracting the baseline of the SERS sensor. Phenethyl alcohol, acetophenone, anethole gases were individually detected by polymer film-coated SERS gas sensors. The target gas was exposed to the sensor before SERS spectra were collected. It is well-known that different regions on a SERS sensor exhibit hotspots with varying signal enhancements [127]. Therefore, ensuring point-to-point reproducibility across a SERS sensor is crucial for accurately assessing the sensor's sensitivity. In this study, SERS spectra from 30 randomly selected points on polymer film-coated SERS gas sensors were obtained. Additionally, the SERS intensities of phenethyl alcohol gas at 1007 cm^{-1}, detected by PAA-coated, PMMA-coated, and PDMS-coated sensors, were calculated and plotted in Fig 3.5. PMMA-coated and PDMS-coated sensor exhibited the lowest and highest sensitivity for phenethyl alcohol gas, respectively. The SERS spectra of phenethyl alcohol gases obtained from polymer

film-coated sensors were shown in Fig. S3. 4. Furthermore, the SERS intensity results for acetophenone gas at 1007 cm^{-1} and anethole gas at 1175 cm^{-1} detected by three polymer film coated SERS gas sensor, were recorded in Fig. S3.5 and S3.7, respectively. The SERS spectra of acetophenone and anethole gases detected using three polymer-coated sensors were shown in Fig. S3.6 and S3.8, respectively. The variations in affinities arising from the physicochemical properties of polymers for the target gas led to differences in the amount of gas absorbed on the sensor surface, resulting in diverse intensities in the SERS signal for the target gas. Moreover, small variations in the points of SERS intensities were observed on a single sensor. The variation in SERS intensity on the SERS gas sensor could be attributed to two main factors: (1) the density and size of Ag nanoparticles sputtered on the SERS sensor exhibited a certain level of uniformity, affecting the homogeneity of intensities and quantities of hotspots, and (2) due to the fluidity of the gas, the attachment point of gas on the sensor was indefinite, leading to variations in the quantity of gas at different detection points. Consequently, the analysis utilized data from 30 points to enhance accuracy.

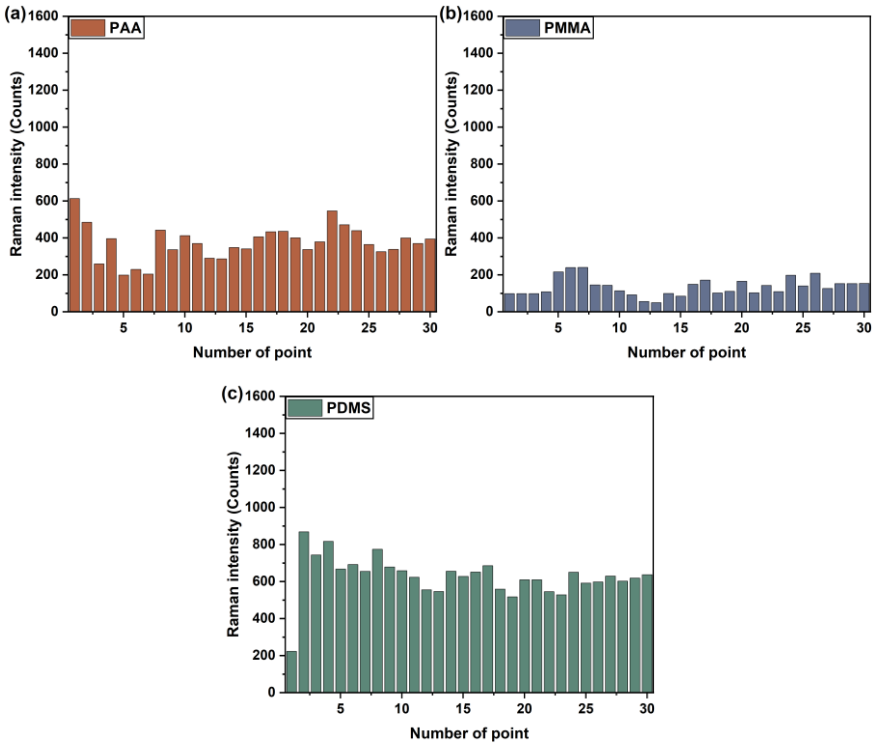

Fig. 3. 5. SERS intensity collected from random 30 points obtained by using (a) PAA, (b) PMMA and (c) PDMS polymer film coated SERS gas sensor for phenethyl alcohol gas detection.

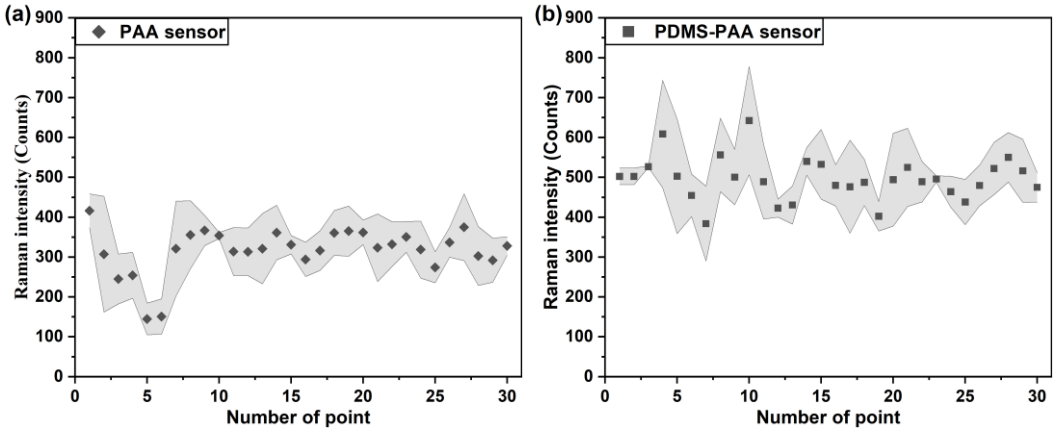

Fig. 3. 6. Error band calculated using 30 points obtained from (a) PAA-coated, (b) PDMS-PAA-coated SERS gas sensor for phenethyl alcohol gas detection.

Another aspect considered in evaluating SERS sensors is their batch-to-batch producibility [128]. Since single-layer polymer film sensors exhibited distinct gas responses, we extended our investigation to the gas response of double-layer polymer film sensors. Specifically, we detected phenethyl alcohol gas using PAA-coated and PDMS-PAA-coated SERS gas sensors. To ensure consistent relative positions, the x-y stage in the detection system was adjusted for all three sensors, maintaining the same positions for 30 detected points relative to the gas inlet. Due to the increased thickness of the double-layer polymer film, gas molecules took longer to adhere to the SERS gas sensor surface. The average values and error bands for the same relative position points (three points) on the three sensors were calculated, as depicted in Fig. 3. 6. While there was variation in the SERS intensities among the 30 points, the relatively narrow error bands at the same position suggested acceptable batch-to-batch producibility of the SERS gas sensor. Additionally, the SERS intensity of phenethyl alcohol gas detected by the PDMS-PAA-coated sensor was higher than that of the PAA-coated sensor. This difference could be attributed to the better affinity of PDMS polymer to phenethyl alcohol gas compared to the PAA-coated sensor (Fig. 3.5). Therefore, the double-layer PDMS-PAA polymer film structure enhanced the sensor's affinity to phenethyl alcohol gas. This confirmed that a novel response property could be achieved by designing a double-layer polymer film with two single-layer polymer films. Three types of double-layer polymer films, PDMS-PAA, PMMA-PAA and PDMS-PMMA, were selected to fabricate SERS gas sensors for detecting phenethyl alcohol, acetophenone, and anethole gases.

3.3.4 Gas recognition using polymer film coated SERS gas sensor array

3.3.4.1 Target gas recognition by bare and single-layer polymer film coated sensor

The SERS intensity results of a previously described characteristic peak (Fig. 3.5, S3.5, and S3.7) revealed that the polymers employed in this study exhibited varying affinities to the three target gases. Instead of focusing solely on the intensity value at a single characteristic peak, the SERS intensities at 1007 cm^{-1}, 1175 cm^{-1} and 1605 cm^{-1} were employed as responses for discriminating among the three target gases. A total of 90 samples (comprising three target gases with 30 points each in one detection) were considered, with intensity values at the three selected peaks treated as characteristic variables, as depicted in Fig. S3. 9. Consequently, a response matrix $M_{90\times3}$ is generated for gas recognition analysis. PCA, an unsupervised machine learning method, was then applied for the dimensionality reduction of the high-dimensional data [129, 130]. Principal components (PCs) were extracted through linear combinations of the original variables. Subsequently, the cluster trends of the target gases were visualized in a two-dimensional space using uncorrelated scores from two PC. In this study, the response matrix was pre-processed through auto-scaling to mitigate the large variation observed in different Raman intensity data. We conducted PCA analysis using R software (version 4.1.0). The two primary PC scores (PC1 and PC2) were employed to create two-dimensional graphs. Subsequently, a confidence ellipse with a confidence level of 95% for each cluster was added onto the two-dimensional plot. Increased distances between the confidence ellipses of distinct clusters indicated greater differences,

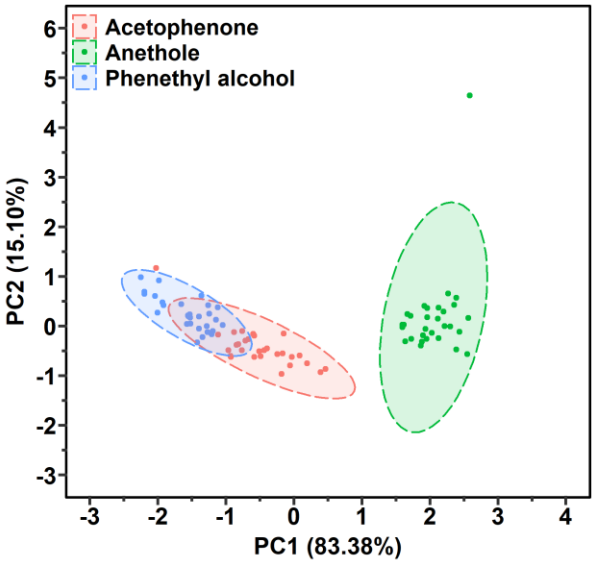

Fig. 3. 7. PCA score plots of phenethyl alcohol, acetophenone and anethole gases detected by bare SERS sensor.

facilitating their distinguishability. Additionally, the size of the confidence ellipse signified the dispersion of the samples; larger ellipses indicated more dispersed samples.

Initially, we utilized the response matrix derived from the unmodified SERS sensor for gas recognition. The PCA score plots of samples detected by the unmodified sensor were presented in Fig. 3.7. In this plot, the clusters of phenethyl alcohol and acetophenone exhibited an overlap, while the cluster of anethole was distinctly recognizable. This observation could be attributed to the similarity in the SERS spectra of phenethyl alcohol and acetophenone, sharing common characteristic peaks at 1007 cm^{-1} and 1605 cm^{-1}. In contrast, anethole possessed a unique peak at 1175 cm^{-1}, allowing for its discrimination from phenethyl alcohol and acetophenone gases. Furthermore, the horizontal alignment of these three clusters suggested that SERS intensity at 1175 cm^{-1} plays a crucial role in PC1.

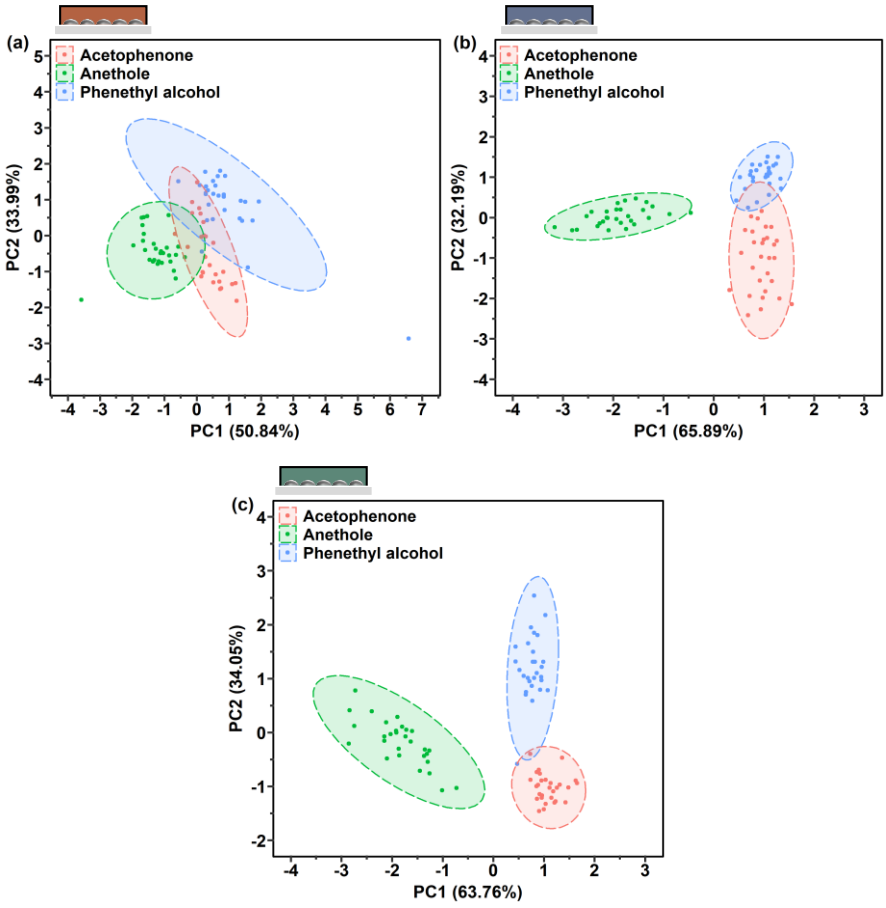

Fig. 3. 8. PCA score plots by (a) PAA-coated, (b) PMMA-coated or (c) PDMS-coated SERS gas sensor used for phenethyl alcohol, acetophenone and anethole gases detection.

Subsequently, we employed a single-layer polymer film SERS gas sensor to recognize three target gases. The distribution of 90 collected samples from the single-layer polymer film sensor was depicted in PC1-PC2 space in Fig. 3. 8. Generally, the clusters of the three gases exhibited distinct distribution patterns. Specifically, clusters of the 90 samples detected by the PAA-coated sensor overlapped with each other, while clusters in the PC1-PC2 space of the PMMA-coated and PDMS-coated sensors were distributed both horizontally and vertically. Phenethyl alcohol and acetophenone clusters overlapped in Fig. 3. 8a, b and c, a phenethyl alcohol sample was incorrectly classified into the acetophenone cluster in Fig. 3. 8c, attributed to their similar SERS spectra. On PMMA and PDMS sensors, there were less overlaps between the acetophenone and phenethyl alcohol clusters compared to the results from the unmodified sensor. The distribution patterns in the PC1-PC2 space of the three polymer-coated sensors confirmed that these polymers elicited different gas responses for phenethyl alcohol, acetophenone, and anethole. It was noteworthy, however, that the three target gases did not occupy entirely separate regions.

3.3.4.2 Target gas recognition of two single-layer and one double-layer polymer film coated SERS gas sensor

As a single-layer polymer-coated SERS gas sensor proved insufficient for the recognition of the three target gases, gas responses from two different polymers were employed for the recognition process. The responses from the two polymers could be acquired through two different approaches: SERS intensities recorded from (1) combinations of two single-layer polymer-film coated sensors or (2) one double-layer polymer-film coated sensor. If the gas responses of polymer A and B were defined as R_A and R_B, respectively, the gas response of the double-layer polymer A-B could be represented as either $R_A + R_B$ (a combination of responses from A and B) or R_{AB} (a new characteristic gas response). Herein, the PCA method was employed to determine which method exhibited superior recognition ability for the three target gases. A response matrix $M_{90\times6}$ was formed by combining the data from two single-layer polymer film-coated sensors, incorporating 90 samples (comprising three target gases with 30 points each) and six characteristic variables (representing three SERS intensities for each of the two polymer films). Additionally, a response matrix $M_{90\times3}$ was created for the double-layer polymer film-coated sensor, comprising 90 samples and three characteristic variables (representing three SERS intensities detected by one sensor). The PCA score plots for the combination of PAA-coated and PDMS-coated SERS gas sensors and PDMS-PAA coated sensor were illustrated in Fig. 3. 9. In Fig. 3. 9a, the anethole cluster was distinctly separated, and there was a relatively small overlap

between the phenethyl alcohol and acetophenone clusters. However, an acetophenone sample appeared within the phenethyl alcohol cluster, indicating incomplete discrimination between phenethyl alcohol and acetophenone clusters by the PAA-coated and PDMS-coated sensor combination. The PDMS-PAA coated sensor exhibited a less effective recognition performance, as depicted in Fig. 3. 9b. The recognition performance of the PMMA-coated and PAA-coated sensor combination surpassed that of the PMMA-PAA coated sensor, as evident in the PCA score plots in Fig. S3. 10. Surprisingly, the response combinations of PDMS-coated and PMMA-coated sensors (Fig. S3.11) resulted in well-differentiated clusters for the three gases. However, it was noteworthy that the distance between the anethole cluster and the phenethyl alcohol cluster was relatively close. Increasing the number of characteristic variables in the response matrix might further enhanced the separation distance among the three gas clusters. In conclusion, a double-layer polymer film-coated sensor exhibited a distinct response characteristic in comparison to a single-layer polymer film-coated sensor. Importantly, the combination of responses from two single-layer polymer film-coated sensors demonstrated superior gas recognition performance when compared to one double-layer polymer film-coated sensor.

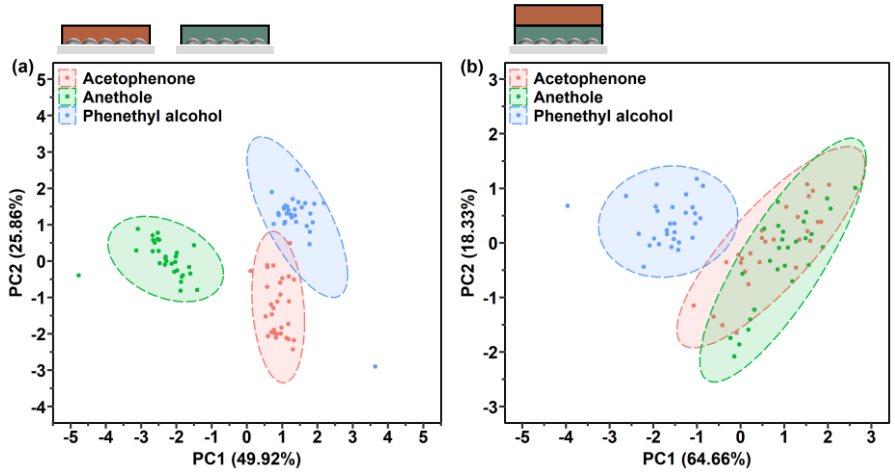

Fig. 3. 9. Comparation of PCA score plots of the (a) PDMS-coated and PAA-coated SERS gas sensors combination and (b) one PDMS-PAA coated SERS gas sensor used for phenethyl alcohol, acetophenone and anethole gases detection.

3.3.4.3 Gas recognition ability improvement by increasing characteristic variables in response matrix

The gas responses acquired from multiple polymer film-coated SERS gas sensors were utilized in constructing a response matrix for gas recognition. Consequently, three response matrices were formed: $M_{90\times9}$ (representing three single-layer film-coated

sensors), $M'_{90\times9}$ (representing three double-layer film-coated sensors), and $M_{90\times18}$ (representing the combination of three single-layer and three double-layer film-coated sensors). Specifically, $M_{90\times9}$ and $M'_{90\times9}$ were both constructed with 90 samples and nine characteristic variables (SERS intensities at three characteristic peaks multiplied by three polymers film). The characteristic variables of $M_{90\times18}$ were set at 18, comprising SERS intensities at three characteristic peaks multiplied by the total number of polymer films (three single-layers + three double-layer). PCA score plots in PC1-PC2 space for these three response matrices were shown in Fig. 3. 10. By increasing the number of characteristic variables from six to nine, as shown in Fig. 3. 10a, the three gas clusters

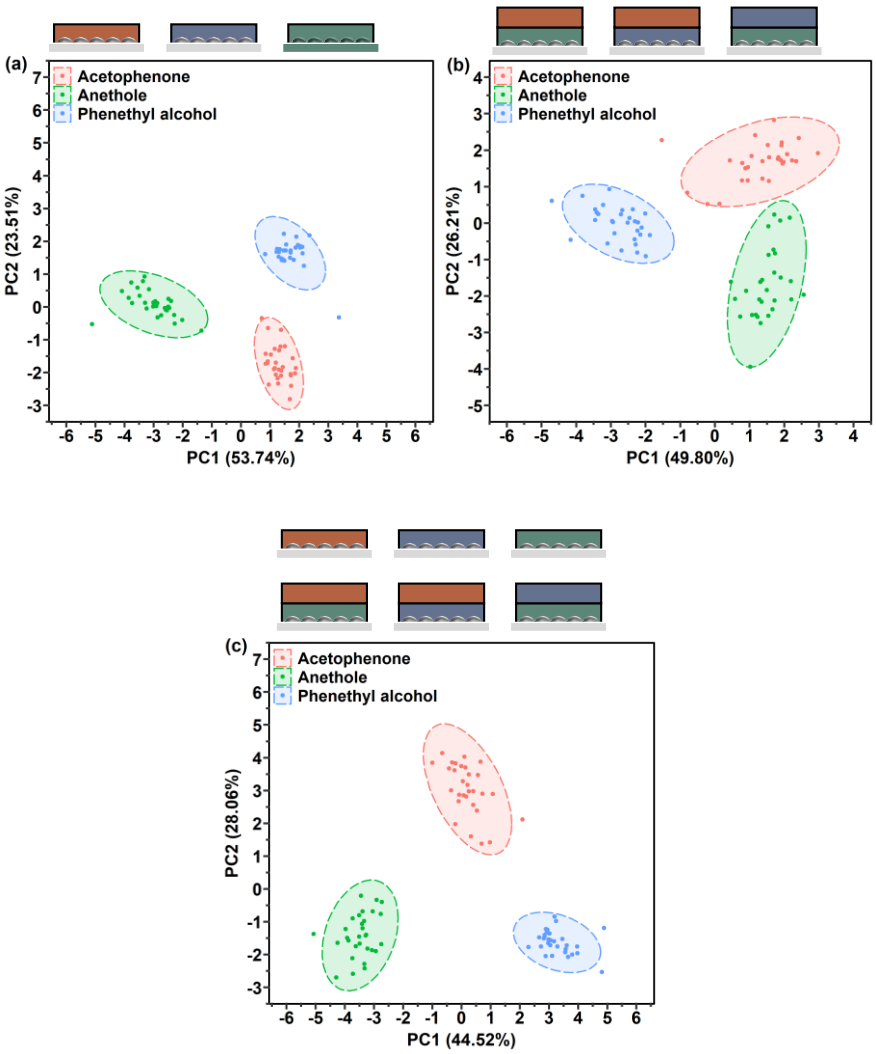

Fig. 3. 10. PCA score plots of the (a) three single-layer polymer film coated SERS gas sensors, (b) three double-layer polymer film coated SERS gas sensors, (c) three single-layer and three double-layer polymer film coated SERS gas sensors used for phenethyl alcohol, acetophenone and anethole gases detection.

were completely separated, and the distance between clusters was further compared to the results in Fig. S3. 11. Notably, the response matrix $M'_{90\times9}$ had the same number of characteristic variables as $M_{90\times9}$, enabling easy recognition of the three gas clusters. In contrast, the PCA score plot in Fig. 3.10b revealed the proximity of the anethole cluster to the acetophenone cluster. This observation could be attributed to the double-layer polymer film-coated sensor presenting a novel response property for the three target gases. Consequently, the amount of information provided remained consistent with that of the single-layer polymer film-coated sensor. Notably, in Fig. 3.10c, the three gas clusters exhibited a widely dispersed distribution. Therefore, increasing the number of characteristic variables in the response matrix, processed by the PCA method, effectively enhances the gas recognition capability, as indicated by our results.

3.4 Conclusion

In this chapter, multiple polymer film coated SERS gas sensors were developed to distinguish gases with similar structures. Three target gases, namely phenethyl alcohol, acetophenone, and anethole, each comprising a benzene ring and distinctive functional groups, were chosen for the study. Single-layer polymer films on SERS gas sensors were fabricated using PAA, PMMA, and PDMS through the spin-coating method. Additionally, a double-layer polymer film was created by flexibly combining two single-layer films using the layer-by-layer method. The SERS spectra of the three target gases were collected as they were detected by polymer-coated sensors with varying gas affinities. Characteristic variables in the response matrix for PCA analysis were SERS intensities at selected characteristic peaks of the target gases. Furthermore, the choice of characteristic variables could be altered by employing SERS intensities detected by different polymer-coated sensors. As inferred from the PCA results, gas molecules with similar structures were accurately discriminated, showcasing that the double-layer film-coated sensor exhibited a novel response property compared to a single-layer film-coated sensor. The most effective gas recognition outcome was observed when the response matrix was constructed with 18 characteristic variables according to the PCA score plot. Additionally, the gas recognition performance was enhanced by increasing the number of characteristic variables in the response matrix. This outcome substantiates that the recognition of gases with similar molecular structures can be achieved using SERS sensors spin-coated with multiple polymers possessing different affinities.

Chapter 4

4. Visualization of the spatial distribution of gas from odor sources

4.1 Introduction

On the basis of recognizing VOC gases, visualizing the spatial distribution of gases can extend the range of applications. Analyzing the spatial distribution of the VOC gas provides crucial insights into the odor source. By examining how airflow influences the spatial distribution of the detected gas, a robot equipped with recognition algorithms can accurately pinpoint the location of the odor source [131-133]. Furthermore, studying the spatial distribution of gas evaporating from the odor source allows us to elucidate essential information encompassed in the odor source, such as its composition, localization, and temporal variations [134-136].

The gas spatial distribution can be visualized using the gas concentration information obtained from sensors. A large-scale sensor array was previously constructed using the metal MOS sensors and used to visualize gas distributions [137]. This sensing system was portable and cost-effective; however, it collected a limited amount of data, which led to relatively low-resolution images. A fluorometric sensor has been developed for the visualized detection of the gas. The intensity of the fluorescent light changed with the concentration of the detected gas after the sensor was excited with ultraviolet (UV) light, the fluorescent signal was collected using a camera [134, 138]. As a result, the spatial distribution of the gas was visualized using a high-resolution color image. This sensor required suitable fluorescent dyes for the target gas and consideration of the lighting interference in the environment. Moreover, a gas sensor based on LSPR combined with a cooled charge-coupled device camera was used to visualize gas distributions. The LSPR sensor was easily fabricated by depositing metallic nanoparticles (NPs) on the substrate, which was used without further modification and exhibited a rapid response. Specific gas molecules interacting with the NPs shift the LSPR frequency and intensity, enabling gas detection and quantification. These changes were used for gas visualization [139]; however, the selectivity of the LSPR sensor has yet to be resolved. Notably, SERS sensors offer solutions to various challenges encountered in other gas sensing technologies. SERS sensor offers three key

advantages in visualizing spatial distribution of gas: (1) accurate identification of analytes through vibrational spectroscopy [69, 140], (2) label-free molecular detection, streamlining the detection process [70], and (3) high-resolution imaging by capturing SERS spectra at various positions on the sensor surface [141, 142].

In this chapter, we introduced a two-dimensional (2D) SERS sensor array designed to visualize the spatial distribution of gas evaporating from odor sources positioned at various positions. Specifically, the 2D sensor array, comprising nine identical small-sized SERS sensors, was constructed in a 3×3 grids. The benzaldehyde odor source was heated to release the gas, and the custom-designed sensor array was positioned above the odor source. Subsequently, the odor-adsorbed sensor array underwent scanning to collect SERS spectra from different locations. From the gathered SERS spectra, the intensities of specific Raman characteristic peaks corresponding to the detected odor were extracted. This intensity information was then utilized to generate a heatmap image, offering a visual representation of the spatial distribution of the odor. Ultimately, by analyzing features of the gas spatial distribution, the localization of the odor source can be determined.

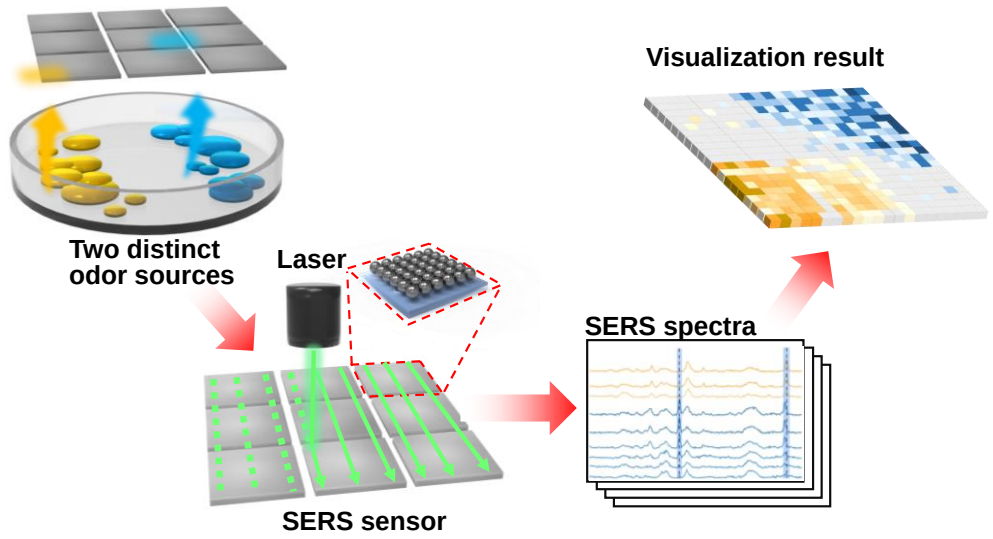

Fig. 4.1. The schematic illustration of visualizing the odor source using a two-dimensional SERS gas sensor array.

4.2 Materials and Methods

4.2.1 Fabrication of SERS sensor

The fabrication process of the SERS sensor involves three steps: synthesizing Ag

seeds solution, using Ag seeds to synthesize larger Ag NP solution, and transferring these larger Ag NPs onto a glass substrate. All steps were conducted in the laboratory.

First, the Ag seed solution was synthesized according to a previous report [143]. One mL of an aqueous solution containing sodium citrate (1 wt%), 0.25 mL of an aqueous solution of silver nitrate ($AgNO_3$) (1 wt%), and 0.2 mL of an aqueous solution of sodium chloride (NaCl) (20 mM) were introduced into 1.05 mL of water while stirring. Following a 5-minute interval, the citrate-silver-NaCl solution was combined with 47.5 mL of boiling water, with the addition of 80 μL of an aqueous solution of L-ascorbic acid (AA) into the boiling water one minute before introducing the citrate-silver-NaCl solution. After heating for one hour, the resulting solution yielded the Ag NP seed solution.

Second, Ag NPs with a size of approximately 90 nm were synthesized using the prepared Ag seeds solution. Initially, 2 mL of an aqueous solution containing silver nitrate ($AgNO_3$) (1 wt%) was combined with 800 μL of ammonia water (25%−28%). Subsequently, 550 μL of the original solution of Ag NP seeds was introduced into water (18.92 mL) with stirring in a 50 mL glass bottle. Following that, an aqueous silver-ammonia complex solution (280 μL, 43 mM) and an aqueous solution of L-ascorbic acid (AA) (8 mL, 2.5 mM) were added to the same glass bottle. After stirring for one hour, the Ag NPs were concentrated through centrifugation, redispersed in 5 mL of an aqueous solution. Finally, 100 μL of an aqueous solution of tetrabutylammonium nitrate ($C_{16}H_{36}N_2O_3$) was added.

Lastly, a densely packed Ag NP monolayer film was deposited onto a glass substrate using the oil/water/oil three-phase system based on the Marangoni effect [100, 144]. In this process, 2.5 mL of the concentrated aqueous Ag NP solution was mixed with 2 mL of chloroform in a 15 mL centrifuge tube. Following a 30-second hand shaking of the tube, 0.6 μL of hexane was introduced. The formation of the densely packed NP monolayer film took place at the interface between hexane and water in this solution. Finally, the monolayer film was transferred onto the glass substrate to serve as the SERS sensor. This transfer was accomplished by inserting a glass substrate under the monolayer film at an angle and then pulling it out, resulting in the film being transferred onto the glass substrate measuring 5 mm × 5 mm. The entire fabrication process was illustrated in Fig. S4.1. A 2D sensor array was created by arranging nine SERS sensors in a 3 × 3 configuration. In this sensor array, neighboring sensors were closely positioned, and their distance was deemed negligible (0 mm). Consequently, the overall dimensions of our SERS sensor array were 15 mm × 15 mm.

4.2.2 Reproducibility of the fabricated sensor

Immersing nine SERS sensors in an 8 mL ethanol solution containing a 4-aminothiophenol (4-ATP) at a concentration of 1 μM for one hour, followed by cleaning with an ethanol solution and drying under a nitrogen flow. The reproducibility of the fabricated SERS sensor was evaluated by calculating the SERS intensities of the selected characteristic peak.

4.2.3 Detection of the gas evaporating from odor source

For generating odor sources, BZD solution was individually added to an aluminum cup with a 5 mm diameter and depth. Gas generation occurred under two conditions: without heating and with the odor source heated using a Peltier device for one minute to accelerate gas evaporation. Five positions were selected for placing the odor source: center, left-bottom, left-up_left-bottom, right-up_left-bottom and center_left-bottom, as depicted in Fig. S4.2. The SERS sensor array was positioned above the stationary odor source fixed in an enclosed space (Fig. 4. 2a). The detection process was illustrated in Fig. S4.3. Following gas adsorption onto the sensor surface, the sensor array was moved from the odor source and fixed in the detection chamber. The gas's SERS spectra were then collected using a portable Raman spectrometer (Fig. 4. 2b). During the detection process, a total of 1296 spectra were acquired from one sensor array in a scanning format of 36 points × 36 points using a program-controlled detection system. The step distance between the two points was set at 0.4 mm, resulting a calculated detection area of 14.0 mm × 14.0 mm. Each SERS spectrum was collected with a duration of 1 second.

The detection of odor sources with varying sizes followed the same procedure. The size of the odor source was changed by positioning an aluminum plate with a circular hole above it and adjusting the hole's diameter. In addition, as Fig. S4. 4 illustrates, the centers of the hole and the source of the odor were oriented along the same vertical line.

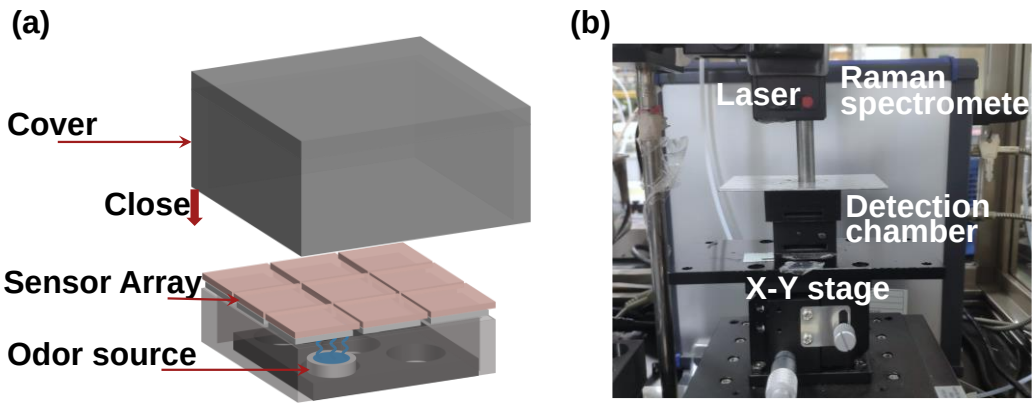

Fig. 4. 2. (a) The gas evaporated from benzaldehyde odor source adsorbed to the SERS sensor array. (b) The photography of home-made gas detection system.

4.2.4 Distribution pattern of the odor source

Utilizing a single SERS sensor array, we simultaneously observed the spatial distribution of gases evaporating from two BZD odor sources. By filling identical cups with the same volume of BZD solution, two odor sources were generated. To position the two odor sources, three distribution patterns were established. Moreover, the proposed approach was applied to simultaneously identify and locate the sources of BZD and 4-ethylbenzaldehyde (EBZD) odors.

4.3 Results and discussions

4.3.1 Performance of fabricated SERS sensor

Using an oil/water/oil three-phase technique, the Ag NPs monolayer film was transferred to the glass substrate to fabricate SERS sensors. The process of seed-mediated development was utilized to synthesize the Ag NPs with large sizes. As illustrated in Fig. 4.3, ultraviolet-visible (UV-vis) spectra were acquired in order to comprehend the optical characteristics of the Ag NP seeds and Ag NPs. For Ag seeds, a distinct dipole peak was observed at around 400 nm. At approximately 500 nm, a new quadrupole peak emerged for the Ag NPs. Moreover, the dipole peak position was red-shifted to a longer wavelength [143]. The morphological features of the Ag NPs on the

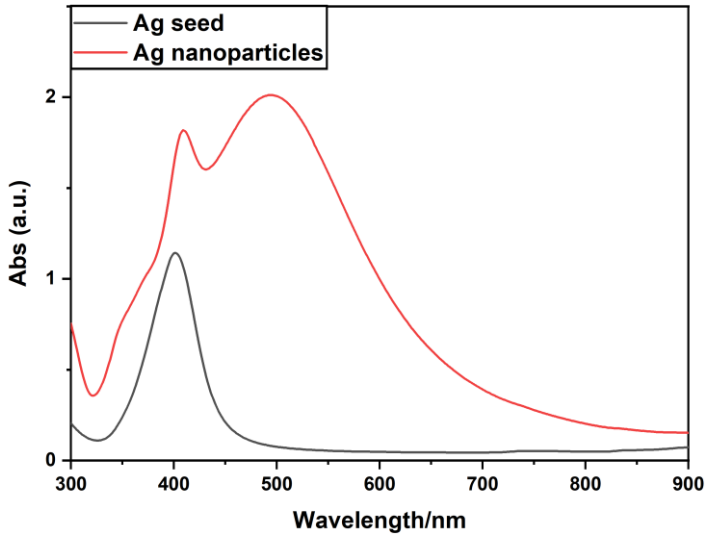

Fig. 4. 3. The UV-vis spectra of the synthesized Ag nanoparticle (NP) seeds and Ag NPs with large size.

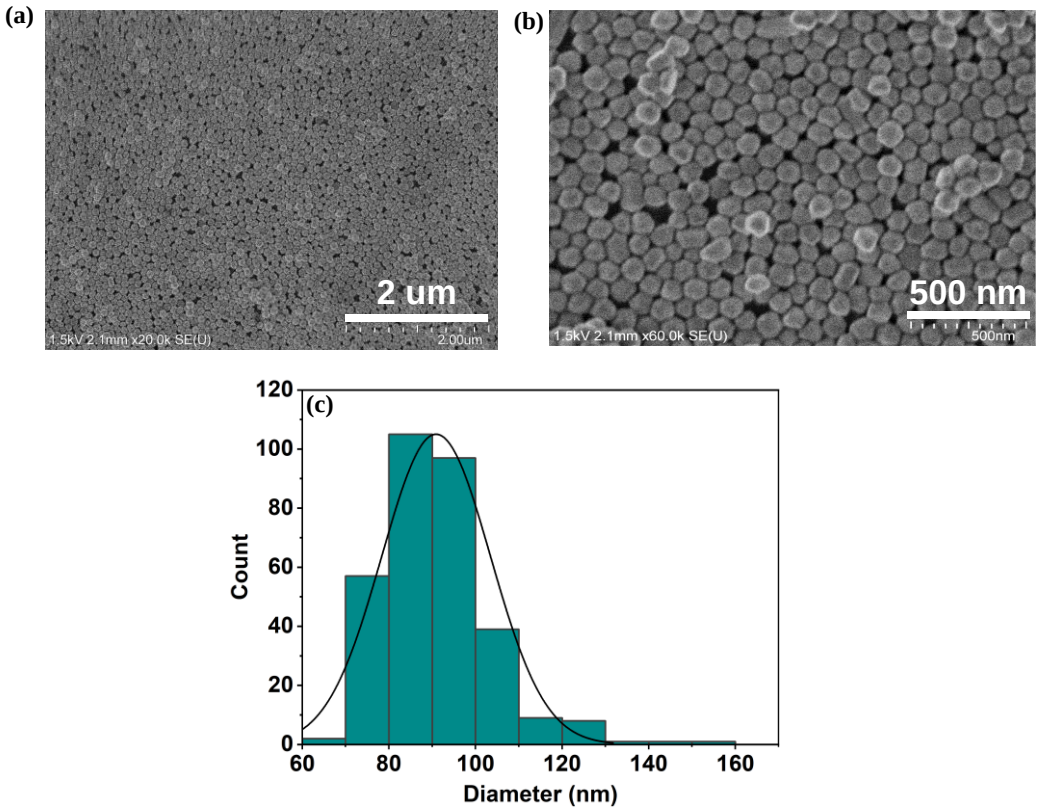

Fig. 4. 4. (a, b) Scanning electron microscope (SEM) image of the Ag NPs on the SERS sensor. (c) Size distribution of the Ag NPs obtained by ImageJ software.

SERS sensor are shown in Fig. 4.4a and b, demonstrating that the monolayer film with a

dense and large-scale arrangement was transferred to the glass substrate. Fig. 4.4a and b illustrated the morphological features of the Ag NPs on the SERS sensor, showcasing the successful transfer of the monolayer film with a dense and large-scale arrangement onto the glass substrate. The synthetically generated Ag NPs exhibited nearly uniform sizes. The scanning electron microscope (SEM) image was processed using ImageJ software (version 1.53) to analyze the size distribution of the Ag NPs on the sensor, as depicted in Fig. 4.4c. The average diameter of the Ag NPs was calculated to be 90.90 ± 12.56 nm.

The sensor was immersed in a 4-ATP solution and the SERS spectrum of 4-ATP was recorded in order to evaluate the homogeneity and reproducibility of the fabricated SERS sensor, as depicted in Fig. 4. 5a. The bond vibration information of the prominent characteristic peaks was summarized in Table S4.1 [145]. Over a 2 mm × 2 mm area,

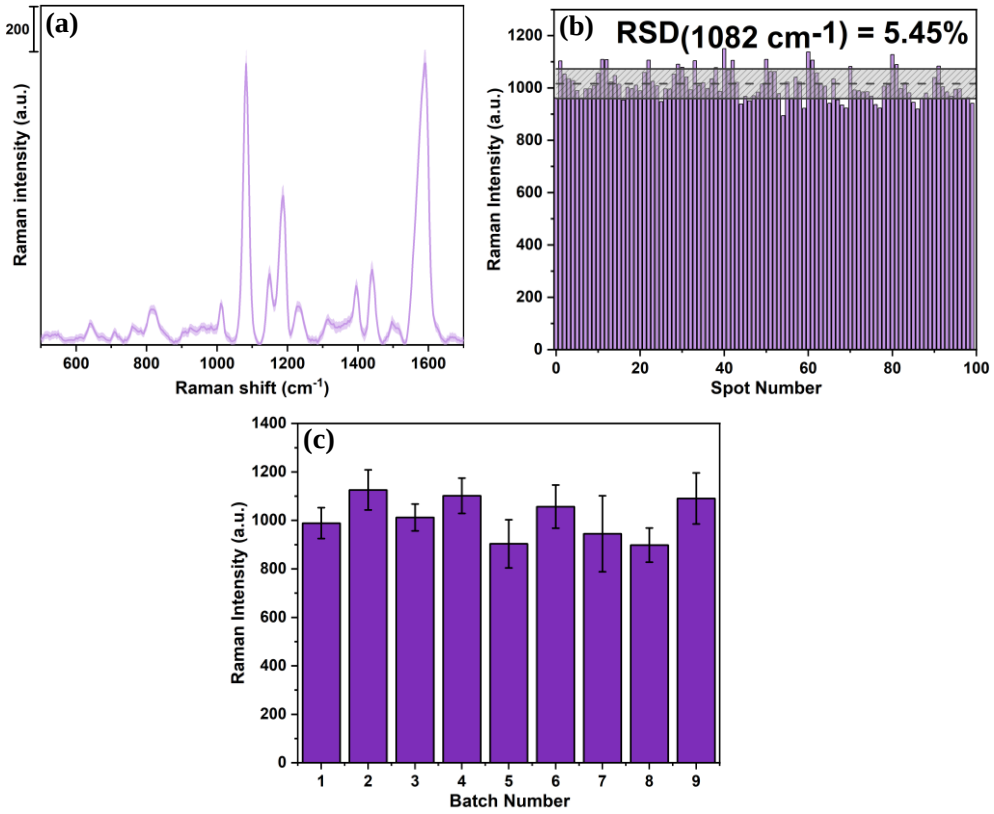

Fig. 4. 5. (a) SERS spectra of the 4-aminothiophenol (4-ATP) modified on the fabricated SERS sensor. (b) The histogram of the SERS intensities at 1082 cm^{-1} in their corresponding SERS spectra of 4-ATP collected from 100 positions on the sensor. (c) Average values of SERS intensities at 1082 cm^{-1} of 4-ATP obtained from nine SERS sensors.

we obtained 100 SERS spectra at a step distance of 200 μm. The spot-to-spot variation

distributions of the SERS intensities for the 1082 cm^{-1} peak were illustrated in Fig. 4. 5b. For the SERS intensity, the relative standard deviation (RSD) was 5.45%. As a result, the fabricated SERS sensor possessed high uniformity over a large area [69, 146, 147]. Additionally, the reproducibility of the SERS sensor was assessed using nine batches of sensors modified with 4-ATP. Fig. 4.5c provided an overview of the average SERS intensities at 1082 cm^{-1} from 100 spectra for each of the nine batches of fabricated sensors. The great batch reproducibility of the SERS sensor was confirmed with an RSD value of 8.45% across the nine sensors.

4.3.2 BZD odor source detected without heating

4.3.2.1 Benzaldehyde odor detection versus time

The SERS sensor array was exposed to the odor source for the first five minutes of the odor detection process, after which it was scanned. The same array was then exposed for a further 15 minutes prior to the execution of the second scan. Ultimately, a third scan was performed following a further 15-minute exposure. Throughout all three scanning procedures, the beginning point and scanning mode of the array remained constant. We obtained SERS spectra from a specific location near the odor source at different time points, and the results were shown in Fig. 4. 6. For BZD gas, two distinct characteristic peaks were observed at 1006 and 1603 cm^{-1} [148]. The intensity of the peak at 1006 cm^{-1} exhibited an increase over time, suggesting a greater quantity of BZD molecules adhering to the surface of the SERS sensor.

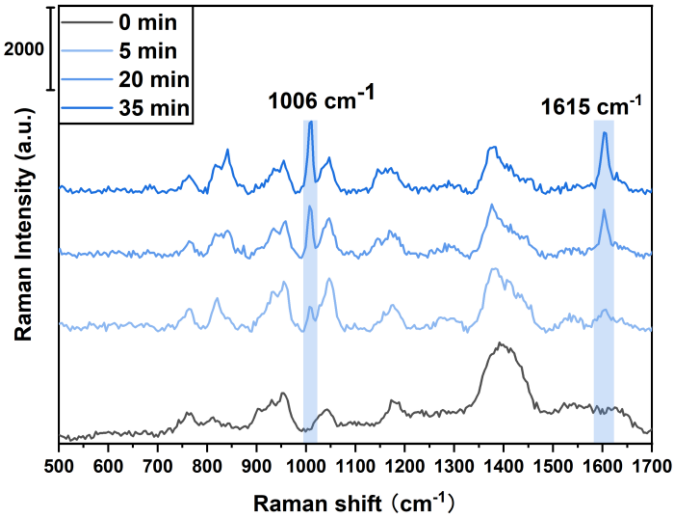

Fig. 4. 6. The SERS spectra of benzaldehyde odor at different time points (0 min, 5 min, 20 min, 35 min) were collected at the same point.

4.3.2.2 Noise reduction of the heatmap graph

During this detection process, the 2D sensor array underwent scanning in a 35 spots × 35 spots format, resulting in the acquisition of 1225 SERS spectra. To generate a heatmap illustrating the spatial distribution of the gas evaporating from the BZD odor source, we utilized the peak intensity values at 1006 cm^{-1} obtained from 1225 locations (35 × 35) on a single sensor array. The heatmap produced by utilizing the raw peak intensity data from a SERS sensor array exposed to the odor source in the left-bottom corner for 35 minutes was shown in Figure 4. 7a. The peak intensity values were significantly higher in the vicinity of the odor source compared to other areas. Moreover, as the position moved away from the odor source, the peak intensity decreased. The SERS spectra of the odor gas were not visible on the far-right side of the SERS sensor array.

Denoising was applied to the heatmap image to enhance the clarity of the spatial distribution of gases visualization results. Images can be denoised using a variety of techniques, such as Gaussian filtering [149], median filtering [150], and Wiener filtering [151]. The gas evaporating from the odor source in our enclosed gas detection setting might be roughly described as a Gaussian distribution. Consequently, Gaussian noise was likely the predominant feature in the generated heatmap image, making Gaussian filtering a suitable choice for addressing the noise in our heatmap images. The denoising effect in Gaussian filtering depended on the size of the Gaussian kernel. In this case, where we need to denoise a limited area while preserving fine-grained details of the

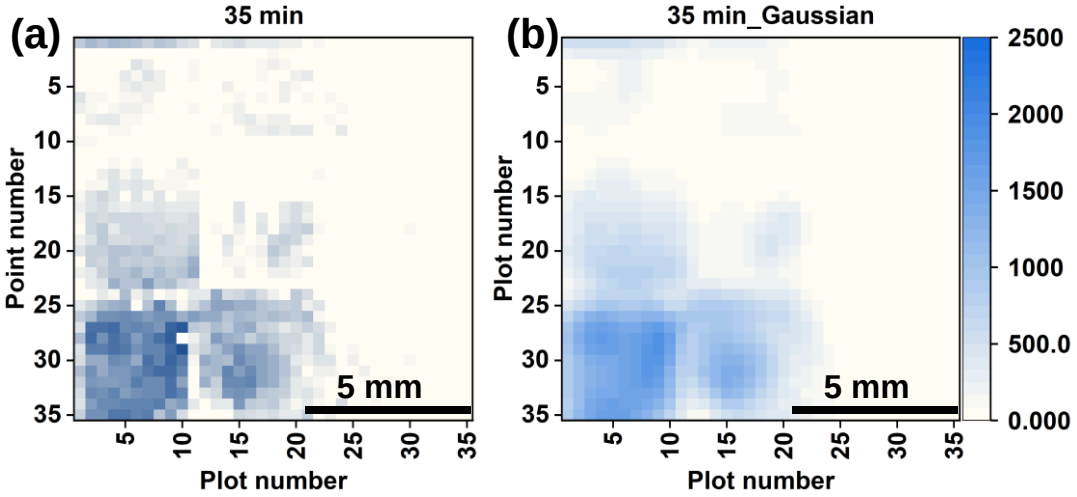

Fig. 4. 7. (a) The heatmap graph generated by 1225 peak intensity values from the SERS sensor exposed to the odor source for 35 min and (b) processed heatmap created by denoising the raw heatmap through Gaussian filter.

gas spatial distribution, a small Gaussian kernel was applied. The denoising process was implemented using Python (version 3.8). Specifically, a 3 × 3 Gaussian kernel with a standard deviation of one was employed for processing the heatmap, resulting in the graph shown in Fig. 4. 7b. Denoising enhanced the clarity of the heatmap, highlighting the location of the odor source. Consequently, the denoising procedure for the subsequent heatmap graphics also utilized the Gaussian filter.

4.3.2.3 Visualization of the spatial distribution of gas versus time

The visualization results of SERS sensors exposed to the odor source for different durations were compared to examine the diffusion dynamics of the odor gas over time. Utilizing the same SERS sensor array, the odor source in the left-bottom corner was observed at 5, 20, and 35 minutes (Fig. 4.8). By analyzing the three heatmap images, it was evident that the odor was barely perceptible before a five-minute exposure. This suggested that only a few benzaldehyde odor molecules were deposited onto the sensor during this brief period. Conversely, as the exposure duration increased, the odor gas surrounding the odor source became more easily detectable. After 20 minutes of

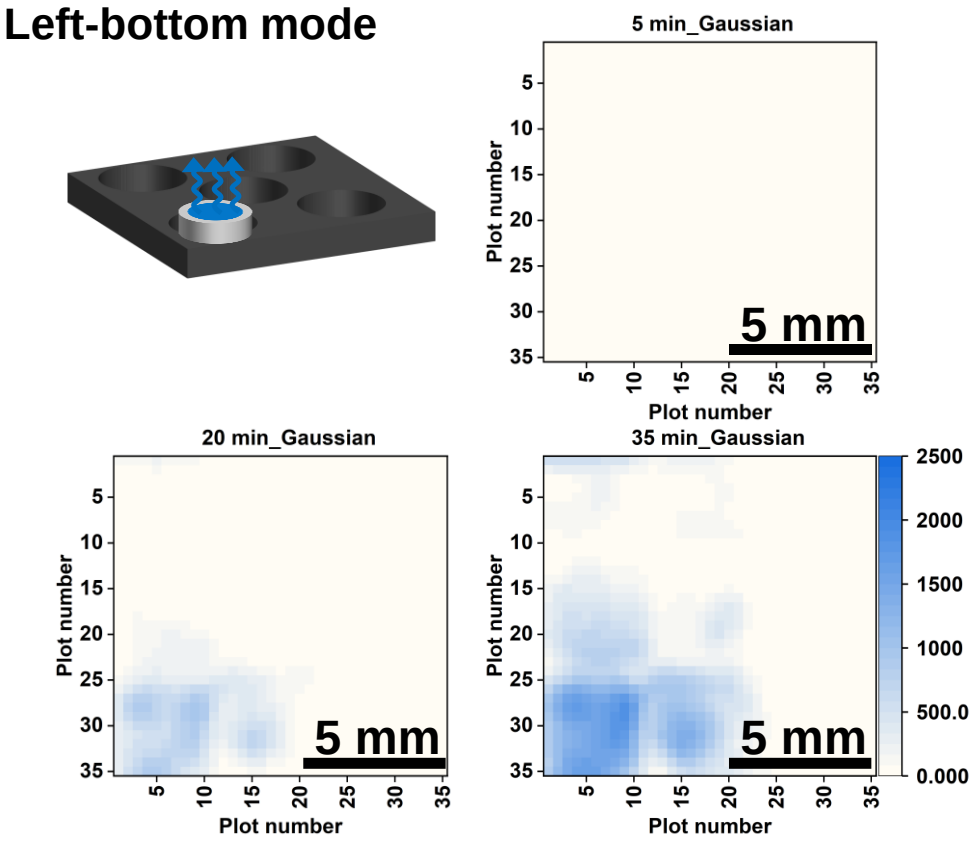

Fig. 4. 8. The visualization of benzaldehyde odor at 5 min, 20 min and 35 min when the odor source was placed at the left-bottom corner.

exposure, the sensor array exhibited a smaller area of odor gas adsorption compared to the 30-minute exposure, and the peak intensity at the same location on the sensor array increased. These experimental findings suggested that the odor spread over time from the left-bottom corner to the surrounding region.

Additionally, as depicted in Fig. 4.9, we conducted two distinct odor source localizations (left-up and left-bottom) to further validate our results. Remarkably, in contrast to the single odor source, we observed a similar odor gas diffusion tendency over time. However, due to the presence of two odor sources, odor gas was detected on the left side of the sensor array during a 20-minute exposure period. The odor gas diffused from the odor source in the left-up and the left-bottom corner to the surrounding simultaneously, therefore, the odor gas could be detected on the left side of the sensor array, which was consistent with our expected results. The detection of odor gas on the left side of the sensor array aligned with our expected results. The

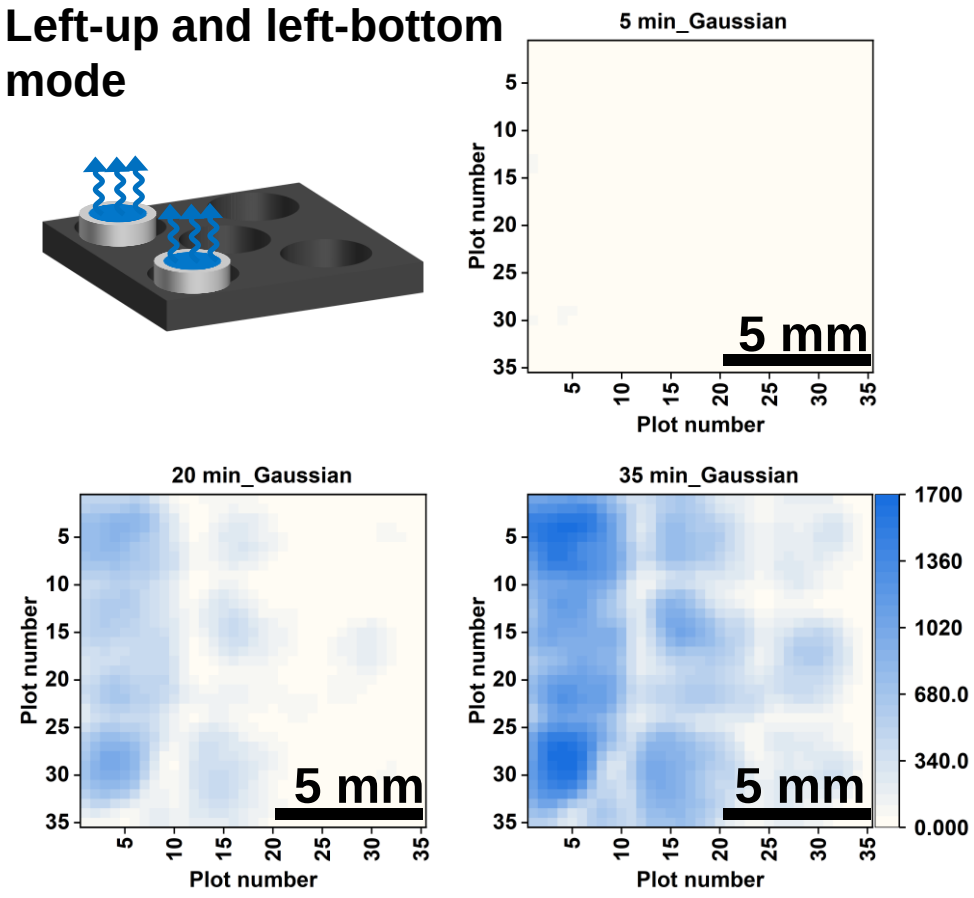

Fig. 4. 9. The visualization of benzaldehyde odor at 5 min, 20 min and 35 min when the odor source was placed at the left-bottom and left-up corner.

odor gas diffused from the odor sources in the left-up and left-bottom corners simultaneously. Additionally, we observed that the peak intensity on the left side was higher than that on the right side, possibly due to the proximity of these regions to the odor source. Consequently, we inferred that as the exposure period increased, the odor gas spread from the left side of the SERS array to the right side.

4.3.3 BZD odor source detected under heating

4.3.3.1 Visualization of the single odor source placed at different positions

Following one minute of heating the odor source, the SERS spectrum of BZD gas became more easily detectable. In a single detection, the 2D sensor array was scanned to collect 1296 (36 × 36) SERS spectra. The SERS intensity of the peak at 1006 cm^{-1} was then calculated to create a heatmap image, illustrating the spatial distribution of the gas evaporating from the odor source.

To simulate the odor source scenario, a framework with five apertures was designed, providing five potential positions for a BZD odor source: Left-Up (LU), Left-Bottom (LB), Center (C), Right-Up (RU), and Right-Bottom (RB). Fig. 4.10 illustrated two visualization results of the odor source positioned in the corner (LB) and center (C) positions. The SERS intensities collected from the sensor array's LB corner were significantly higher than those from other locations when the odor source was placed there. Similarly, higher SERS intensities were observed at the central locations when the

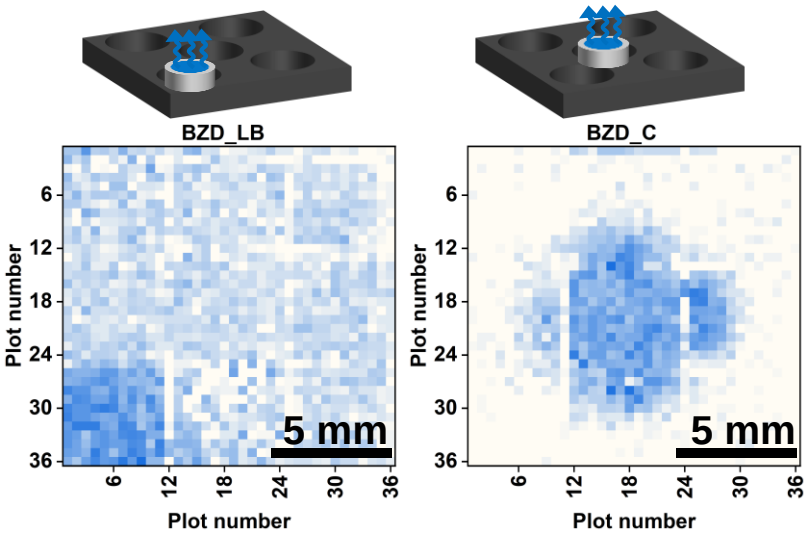

Fig. 4. 10. The heatmap image of visualizing benzaldehyde odor source positioned in the left bottom (LB) and center (C) of the framework.

odor source was placed there. Additionally, as depicted in Fig. S4.5, the distribution of

these SERS intensity values was plotted in a three-dimensional graph. The shape of this distribution bore resemblance to a two-dimensional Gaussian distribution.

4.3.3.2 Visualization of the two odor sources placed at different distribution pattern

To position the two odor sources, three distribution patterns (LB_LU, LB_RU, and LB_C) were established. The heatmap images of the three distribution patterns were easily distinguishable, as illustrated in Fig. 4.11. The spatial distributions of gas from a single odor source were nearly identical when two odor sources were positioned in the LB_LU and LB_RU patterns. Furthermore, due to the sufficient distance between the two odor sources, their mutual diffusion had little effect, making it easy to discern the locations of the two sources. Two gas distributions appeared merged in the LB_C pattern visualization result, creating the appearance of a unified entity. According to the results, the visualization results of the two differently positioned odor sources were essentially a superposition of the separate visualization results based on the positions of the odor sources.

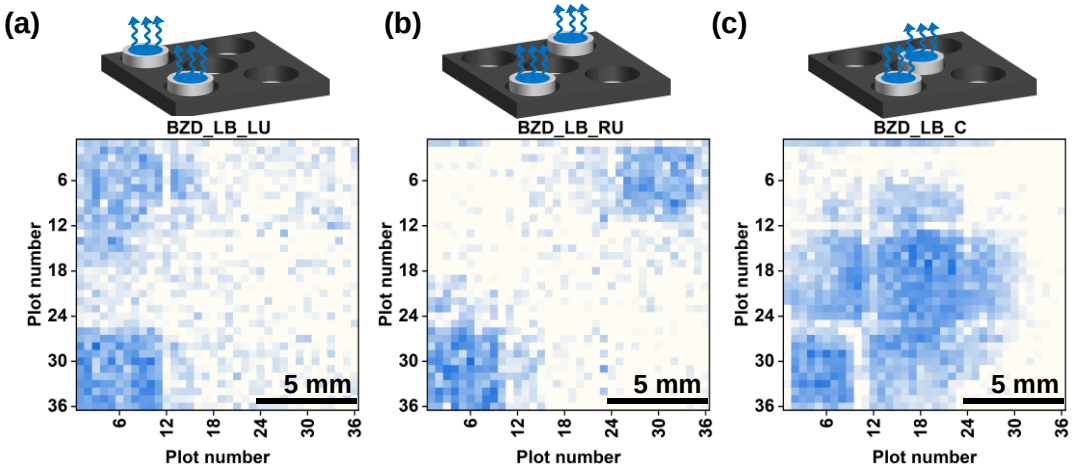

Fig. 4. 11. The visualization and localization result of two benzaldehyde odor sources when the distribution patterns were (a) Left-Bottom_Left-Up (LB_LU), (b) Left-Bottom_Right-Up (LB_RU), and (c) Left-Bottom_Center (LB_C), respectively.

4.3.3.3 Visualization of the odor source with different size

The aluminum plate was prepared with holes measuring 2, 3, and 5 mm in diameter, respectively. The single odor source was positioned at the center of the designed framework. As depicted in Fig. 4.12, despite the aluminum plate covering the odor source, the benzaldehyde gas remained detectable. Three distinct visualizations of odor sources with different sizes were obtained. When comparing the results of BZD_C 2mm

and BZD_C 3mm, there was only a 1 mm fluctuation in the hole diameter, indicating minimal variation in the prominent region's area within the heatmap image. However, because the hole's diameter matched that of the cup, the visualization result for BZD_C 5 mm was comparable to that of BZD_C. Consequently, we inferred that the aluminum plate had no discernible effect on the diffusion of the gas. Furthermore, even with a small 2 mm diameter, spatial distribution of gas from the odor sources of varying sizes could be visualized.

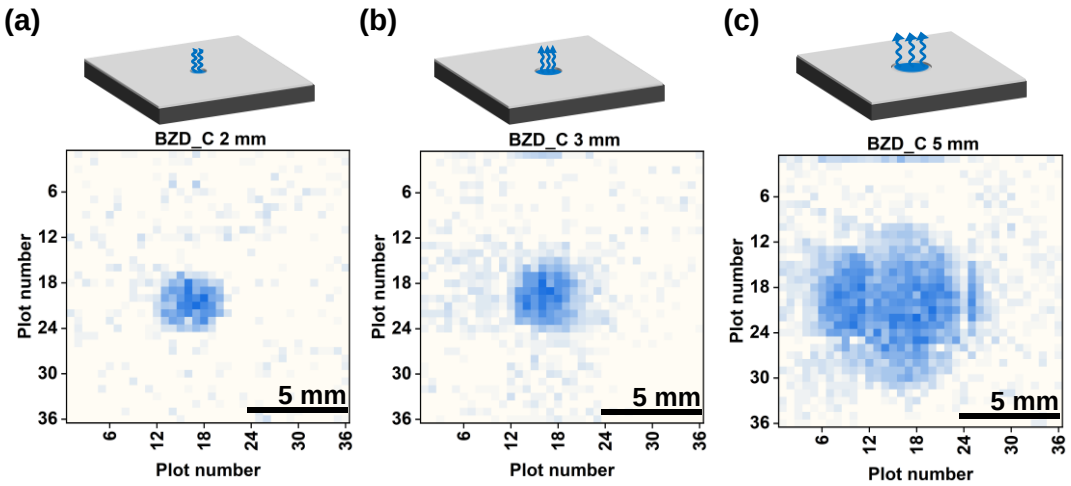

Fig. 4. 12. The visualization and localization result of benzaldehyde odor sources with different size: (a) 2, (b) 3, and (c) 5 mm, respectively.

4.3.4 Visualize the spatial distributions of gases from different odor sources

Because it was necessary to observe more than one odor source simultaneously, identifying distinct odor sources based only on one unique peak in the SERS spectrum may not be possible. Therefore, the utilization of the non-negative matrix factorization (NMF) algorithm became crucial in processing the SERS spectral matrix information acquired from sensor arrays. This spectral matrix encompassed spectra from various individual gases as well as spectra of gas mixtures resulting from their combinations. The NMF algorithm was utilized to extract feature and concentration information of the adsorbed gas at each point on the sensor array. The feature information, which mirrors the gas's SERS spectrum, facilitated the identification of the gas species. A convolutional neural network model was utilized for identifying the feature information. Additionally, the concentration information of the target gas at each point facilitated the generation of a heatmap image, providing visualization of its spatial distribution. The heatmap image underwent processing using a Gaussian fitting model to localize the

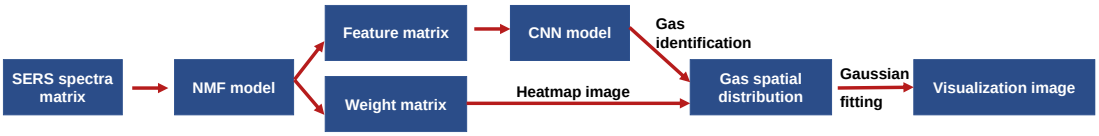

Fig. 4. 13. A flowchart of data processing to identify gases from the collected SRES spectra matrix and visualize the spatial distribution of the specific gas.

odor source. The process of visualizing different odor sources using NMF model was illustrated in Fig 4.13. The illustrations of NMF and Gaussian fitting model were presented in Appendix B.

The proposed method was employed to visualize the spatial distributions of gases evaporating from 4-ethylbenzaldehyde (EBZD) and BZD odor source [152]. We positioned the BZD and EBZD odor sources at the center and the left-bottom locations. As illustrated in Fig. 4.14, the NMF decomposition of the SERS spectra matrix resulted in four feature components. Components r1 and r2 were identified as originating from BZD and EBZD gases, respectively. Components r3 and r4 represented interference (noise and baseline).

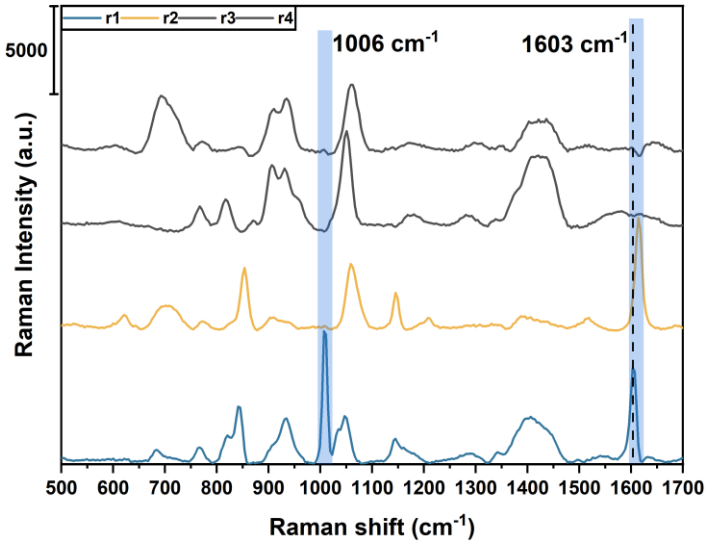

Fig. 4. 14. Non-negative Matrix Factorization (NMF) components were obtained when benzaldehyde (BZD) and 4-ethylbenzaldehyde (EBZD) were detected using one sensor array.

A CNN model was employed to identify these components. To construct our CNN model, we utilized PyTorch (version 2.1) and Python (version 3.8). The training datasets were constructed from the feature data of the component when one and two of the same odor sources were detected. The training dataset was split into training and validation

sets using a 7:3 ratio. A rectified linear units (ReLU) layer was applied after the input data was fed into a one-dimensional convolutional layer. Two consecutive fully connected layers were attached to the ReLU layer. Finally, the SoftMax layer was utilized to classify the output. At the beginning of the training process, the learning rate was 0.0001 and the adaptive moment estimation optimizer was selected. During the training phase, a cosine annealing learning rate scheduling strategy was employed with a period of 10 epochs and a minimum learning rate of 0.00001. The CNN model, after being trained, was applied to identify the components in the NMF decomposition result during the detection of two distinct odor sources.

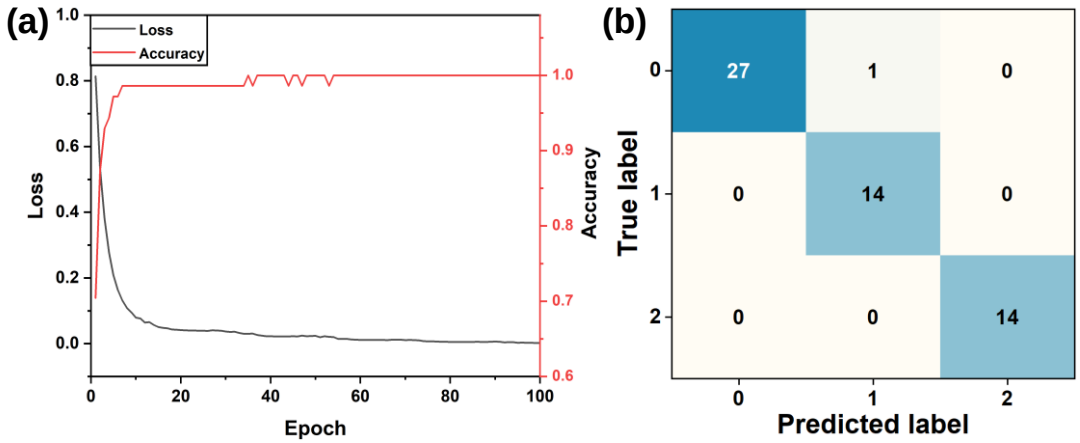

Fig. 4. 15. (a) The loss value of the training and valid dataset when the convolutional neural network (CNN) model was trained. (b) The confusion matrix result for the CNN model used for identifying the NMF components.

The labels 0, 1, and 2 were assigned to the interference, BZD, and EBZD spectra, respectively. As the training progressed, the accuracy consistently increased, while the loss gradually decreased, indicating an improvement in the model's ability to match the data over time (Fig. 4. 15a). The confusion matrix result, with a recognition accuracy of 98.21%, confirmed the effective identification of the trained CNN recognition model, as shown in Fig. 4. 15b. Consequently, the model accurately recognized the feature components in the NMF decomposition data.

In the final stage, the concentration information of the relevant gases was employed to visualize the locations of the odor sources. As an example, we utilized the experiment where EBZD was positioned in the left-bottom and BZD in the left-up to demonstrate how to simultaneously visualize the spatial distribution of both gases. Initially, the concentration data for BZD and EBZD were utilized to generate their respective visualization results. The final visualization, which concurrently illustrated

the spatial distribution of both gases, was generated by overlaying these two visualization results at corresponding points. Therefore, it was possible to identify and localize two distinct odor sources, as depicted in Figure 4.16. The spatial distribution of the BZD gas was indicated by the blue point in the visualization result, while the EBZD gas was represented by the yellow spot. Due to the substantial separation between the two odor sources, the gases were distributed in two distinct spatial patterns.

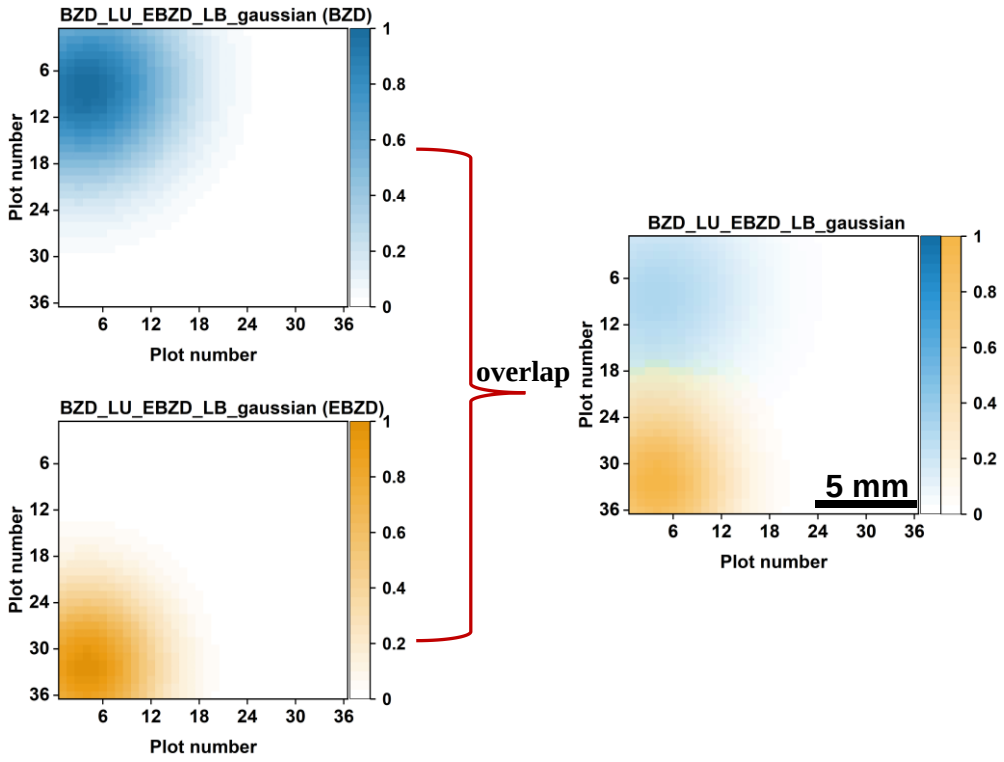

Fig. 4. 16. Overlaying the independent spatial distribution patterns of the two gases enabled the simultaneous visualization of the spatial distribution of both odor sources.

Additionally, as shown in Fig. 4.17a, the spatial distribution of gases evaporating from the BZD in the center and the EBZD in the left-bottom corner was simultaneously visualized. Overlap between the two spatial distributions was observed due to the relatively close physical proximity of the two odor sources. In Fig. 4.17b, it was observed that the spatial distribution of these two gases did not influence each other when BZD was placed in the right-up corner. This can be attributed to the significantly greater separation between the odor sources.

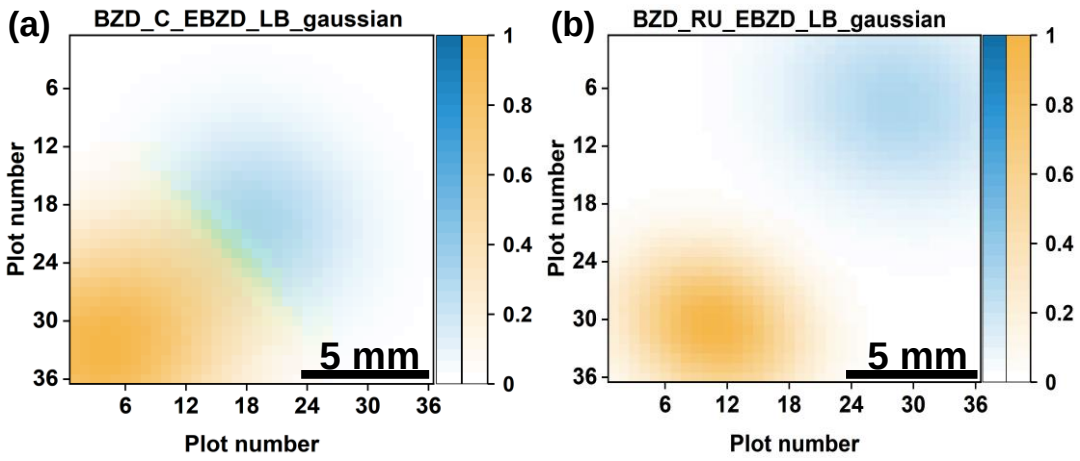

Fig. 4. 17. The visualization result of both BZD and EBZD odor sources detected by one SERS sensor array was obtained. The EBZD odor source was positioned at left-bottom corner. The BZD odor source was positioned at (a) center and (b) right-up corner.

4.4 Conclusion

In conclusion, a 2D SERS gas sensor array was constructed to identify and visualize the gas spatial distribution of BZD and EBZD odor sources. The sensor was fabricated through self-assembly based on the Marangoni effect, ensuring high reproducibility. Positioned above the odor source for gas adsorption, the sensor array was able to capture the gases evaporating from the heated source more effectively compared to the unheated gas. Subsequently, the surface of the sensor array was scanned to obtain SERS spectra of the gases. The SERS intensity values of selected characteristic peaks in the gas spectrum varied at different locations on the sensor. Consequently, a heatmap image was generated using the SERS intensity values of BZD gas, illustrating the spatial distribution of the gas. The results of the gas spatial distribution visualization allowed for an observation of the gas diffusion dynamics over time. These visualization results contributed to a better understanding of the progression of odor gas diffusion from the source to the surrounding environment. Moreover, our proposed method proved effective in visualizing and localizing single BZD odor sources of various sizes.

Distinguishing between different types of gases became challenging when relying solely on several unique distinctive peaks. However, it was possible to differentiate various gases by utilizing SERS spectra that contain molecular structure information. A detection result matrix was constructed using the SERS spectra data collected from the

sensor array and decomposed using the NMF model. The output of the NMF model included concentration and feature information for the detected gas. Plotting the concentration information in a heatmap image facilitated the visualization of the gas's spatial distribution. The image was processed using a Gaussian model to localize the odor source at different positions. To distinguish various components of the feature information, a CNN recognition model was constructed. Consequently, a single sensor array was able to simultaneously identify and visualize the spatial distributions of gases evaporating from BZD and EBZD odor sources placed at distinct positions.

Chapter 5

5. Conclusions and prospects

5.1 Conclusions

5.1.1 Detection and Recognition of the VOC gases using SERS sensor

The distinct characteristic peaks in the SERS spectra are attributed to the specific functional groups of the VOC gas molecules. By comparing these different Raman peak patterns, machine learning-based methods can accurately recognize the VOC gases. Thus, SERS gas sensing technology emerges as a promising method for detecting and identifying VOC gases, owing to its rapid response time, high sensitivity, and exceptional selectivity.

To obtain SERS spectra, a SERS sensor is indispensable as a key device. Two types of the SERS sensor, namely commercial and chemically synthesized nanoparticle-based sensor, were developed to detect VOC gases. The commercial SERS sensor, combined with an adsorption concentrating method, was developed to detect ultra-low concentrations of geosmin. Additionally, the commercial SERS sensors coated with multiple polymer film were fabricated to differentiate VOC gases with similar molecular structures. The chemically synthesized nanoparticle-based SERS sensor was utilized to visualize the spatial distribution of gas from the odor source. The commercially available SERS sensor was highly sensitive and user-friendly but tended to be more expensive. SERS sensors crafted with chemically synthesized nanoparticles exhibited higher sensitivity and cost-effective but involved a relatively complex fabrication process and presented numerous background peaks. Therefore, it is necessary to weigh the detection conditions in order to select the appropriate sensor.

The machine learning models were employed to recognize various VOC gas samples. When detecting gases using SERS sensors coated with polymer films, a PCA model can analyze the intensity of characteristic peaks of the measured gases at specific Raman shifts to differentiate between gas categories. The CNN model was constructed to recognize the feature information of BZD and EBZD odor sources, achieving an accuracy of 98.21%. Therefore, the integration of SERS gas sensors with machine learning models can be developed for recognizing VOC gases.

5.1.2 Visualization of the VOC gases using SERS sensor array

In addition to VOC gas identification, we also visually represent the spatial distribution of gases derived from the recognition results. A SERS sensor array was developed to visualize the spatial distribution of VOC gases evaporating from the odor source in conditions without airflow.

The SERS spectra matrix was acquired by scanning the surface of the SERS sensor array positioned above the odor source. SERS intensity values of characteristic peaks at 1006 cm^{-1} were employed to create a heatmap image, enabling visualization of the gas's spatial distribution. The diffusion of gas on the sensor array was distinctly observable over time. Moreover, a sensor array simultaneously visualized two distinct locations of BZD gas sources. The size of individual BZD gas sources could be determined from these visualized results.

Furthermore, gases evaporating from BZD and EBZD odor sources were detected and visualized using a single SERS sensor array. The NMF algorithm was applied to decompose the acquired SERS spectra matrix, extracting feature and concentration information of the detected VOC gas. The feature information was processed using a CNN model for distinguishing between these two odors. Meanwhile, the concentration information was utilized to generate the heatmap image. This image underwent processing via a 2D Gaussian fitting model, enabling precise localization of these two odor sources. Beyond individually visualizing the spatial distribution of the odor sources, the processed heatmap image revealed the interaction zone between these two sources. This showcased the potential of the SERS sensor array as an easily implementable method for visualizing the spatial distribution of VOC gases.

5.2 Prospects

5.2.1 Identification of VOC mixture gases using SERS sensor

Pure gases (Chapter 3) were accurately identified based on the distinct characteristic peaks in their SERS spectra using the PCA algorithm. Detection of mixed gases, compared to pure gases, holds more significance and may pose greater challenges due to potential overlaps in characteristics among different components within the mixture. This overlap can complicate identification and analysis. Analyzing the entire spectral information holds promise for identifying mixed gases. A SERS sensor fabricated using sputtering method was utilized to detect and identify the pure and mixture VOC gases (Fig. 5. 1).

The VOC gases includes acetophenone, anethole, anisole, and BZD. The 14 types

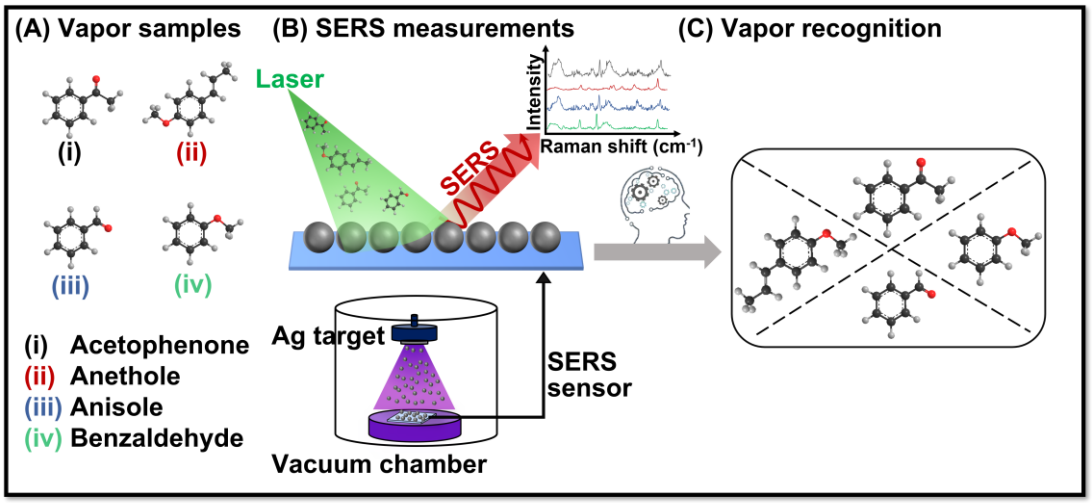

Fig. 5. 1. The Schematic diagram of realization of mixed VOC gases detected by Surface-enhanced Raman scattering (SERS) sensors and identified by machine learning recognition methods.

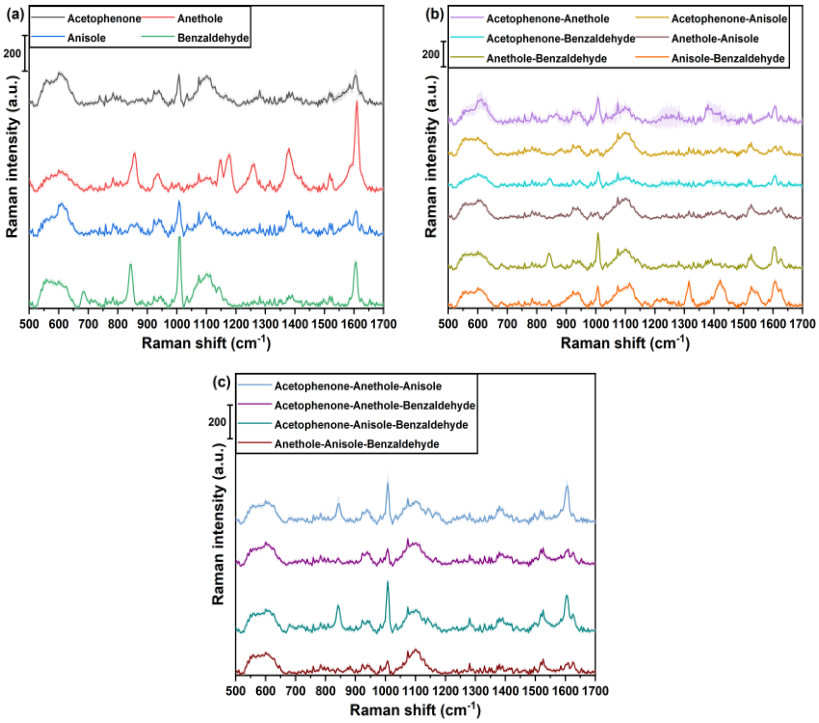

Fig. 5. 2. SERS spectra of (a) the four pure compound vapors, (b) six binary mixtures of compound vapors, and (c) four ternary mixtures of the compound vapors acquired using the bare Surface-enhanced Raman scattering (SERS) sensor.

of VOC gases including four pure, six binary mixtures, and four ternary mixtures gases were detected using the SERS sensors. The distinct SERS spectra were collected as

shown in Fig. 5.2. The vibrational mode assignments of these vapors in the SERS spectra were summarized in Table. S5. 1. We can see that it is not a linear relationship of SERS spectrum between the vapor mixtures and its individual component. As introduced in the section 1.3, electron transfer plays an important role in SERS enhancement. When molecules adhered to the metal nanoparticle surface, electrons transfer from the metal surface to the molecules, forming charge transfer complexes. In our consideration, when multiple vapor molecules simultaneously adhered to the surface of nanoparticles, the electron transfer phenomenon could become more complex due to the diverse interactions between different molecules and pathways of electron transfer. As a result, we have observed the disappearance of certain characteristic peaks.

These VOC gases could be distinguished using a visualization method by processing their distinct SERS spectra. The non-linear dimensionality reduction method t-distributed stochastic neighbor embedding (t-SNE) reduced the normalized 307-dimensional spectral data to two dimensions [153]. Subsequently, the reduced-dimensional data was used to visualize the clusters of gases on a 2D plane as shown in Fig. 5. 3. Except for anethole-benzaldehyde vapor, the other vapors were closely gathered in a relatively separate space. The anethole–benzaldehyde cluster had three distinct sub-clusters, one of which was adjacent to the anisole–benzaldehyde cluster, one adjacent to the anethole–anisole–benzaldehyde cluster, and the other adjacent to the

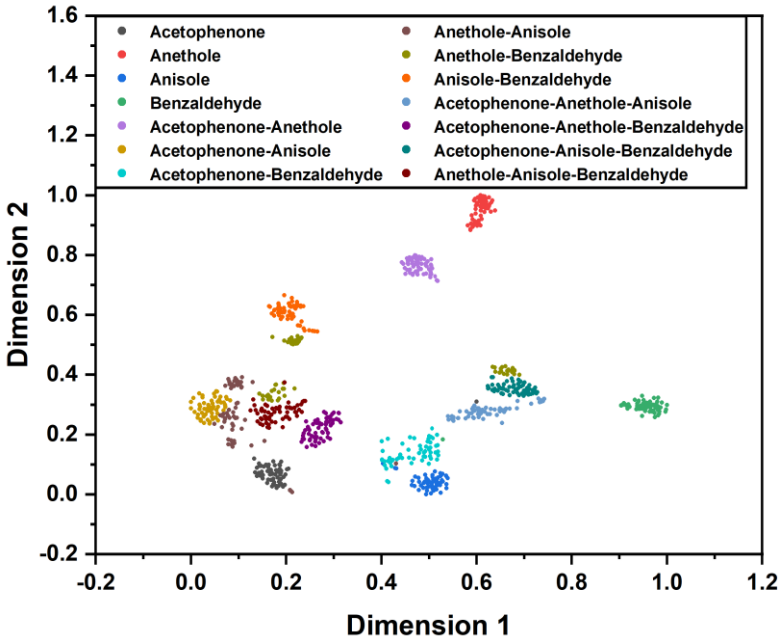

Fig. 5. 3. Visualization of 14 vapors using normalized SERS spectra processed by t-distributed stochastic neighbor embedding (t-SNE) algorithm.

acetophenone–anisole–benzaldehyde cluster. This could be explained by the similarities between the SERS spectra of the anethole–benzaldehyde mixture and the other vapor mixtures.

The t-SNE visualization plot indicated that several vapor samples (anisole (three samples), anethole–anisole (one sample), and benzaldehyde (one sample)) appeared in acetophenone–benzaldehyde mixtures cluster. We used the naive Bayesian classifier (NBC), support vector machine (SVM), and random forest classifier (RFC) recognition models to correctly distinguish between the 14 VOAC vapor samples. The hyper-parameters of SVM and RFC classifiers were optimized using grid search method, and the NBC was used directly to recognize the vapors. The values for the parameters for the classifiers are summarized in Table S5. 2.

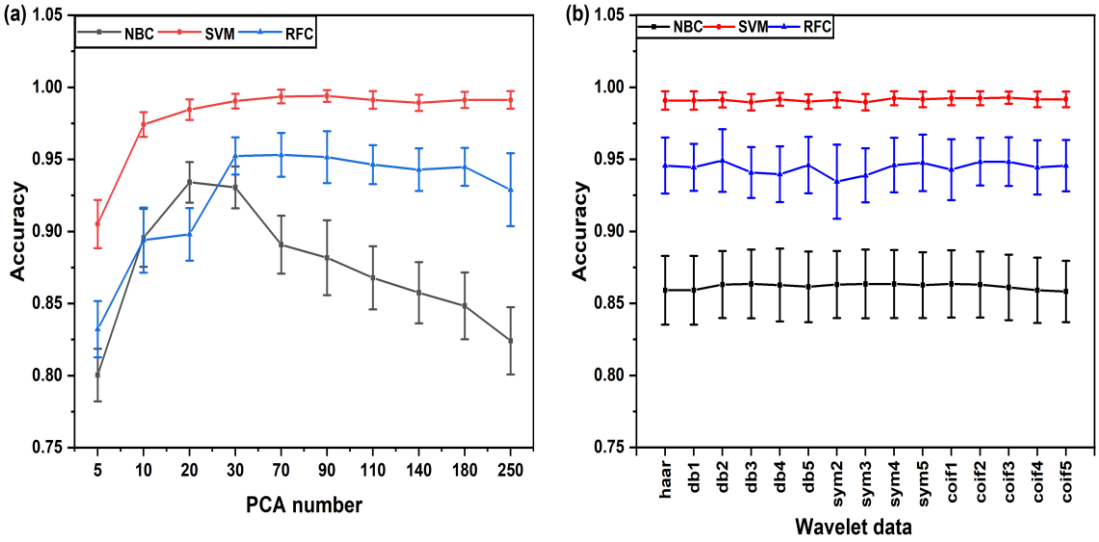

Fig. 5. 4. Accuracy of close-set classification on (a) principal component analysis (PCA) and (b) wavelet data from normalized data after the parameters of models were optimized.

We used PCA and discrete wavelet transform (DWT) to complete the VOAC dataset dimension reduction process. Ten types of PCA-based dataset and 15 types of DWT-based dataset were acquired. Using the processing method described earlier, the mean accuracies achieved using the three classifiers for all datasets were determined. As shown in Fig. 5.4a, the SVM classifier accuracy first increased and then remained relatively stable as the number of principal components increased. The NBC accuracy increased to 20 principal components and then decreased. The accuracy of RFC continuously increased when the number of PC is less than 30, after that, it gradually decreases. When there are too many principal components, it's possible and good

approach to introduce dimension redundancy. Both NBC and RFC may use these features containing limited information for training, which can consequently reduce the accuracy of classification. The SVM classifier was less sensitive than the NBC and RFC to the number of principal components. The highest accuracy value of 99.4% was found for the SVM classifier at 90 principal components. As shown in Fig. 5.4b, the recognition accuracies for the different DWT datasets were not markedly different using the NBC and SVM classifier but the accuracy value was slightly different for the RFC. This could have been because the RFC was trained by randomly selecting data while building the trees in the forest. Interestingly, the SVM classifier also performed best for the DWT dataset, and the highest accuracy value was 99.3% for the coif3 dataset.

We compared the recognition accuracies of the different models for the normalized, PCA-based and DWT-based datasets. The PCA-based dataset constructed using 90 principal components was labeled as PC_90 dataset, and the DWT-based dataset processed using the coif3 filter was labeled as coif3 dataset. The performances of the NBC on the PC_20 and db3 datasets were compared, the performances of the SVM classifier on the PC_90 and coif3 dataset were compared, and the performances of the RFC on the PC_70 and db2 datasets were compared. The optimized hyper-parameters for each classifier are shown in Table. S5.3. Three types of datasets were identified using the well-tuned classifiers, and the accuracies were shown in Fig. 5.5. The 14 vapor samples were clearly better distinguished between by the SVM classifier than the

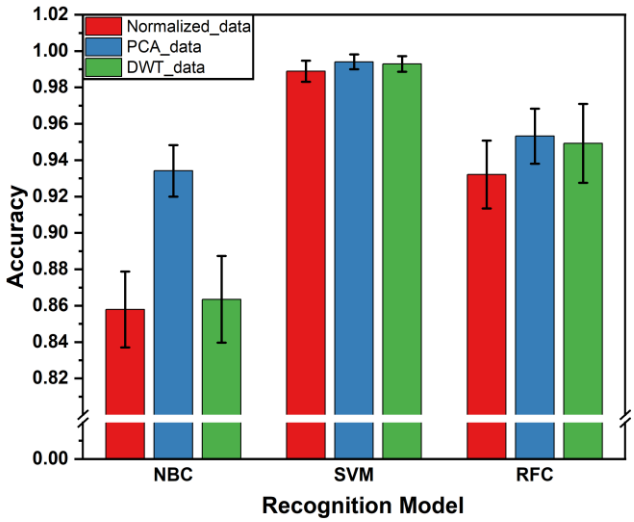

Fig. 5. 5. Best accuracy under different dataset (Normalized data, Normalized_PCA data, and Normalized_DWT data) recognized by three models including naive Bayesian classifier (NBC), support vector machine (SVM), and random forest classifier (RFC).

other classifiers. The three models were less accurate for the normalized dataset than the dataset pretreated using the dimension reduction method. Similar results were found using the NBC and RFC for the three datasets. The maximum accuracy of the NBC was found for the PCA-based dataset. The main features of the SERS spectra may have been encapsulated by the 20 principal components. We concluded that the recognition performance was better for the SVM method than the other methods.

5.2.2 SERS sensor modified with selective MIP

However, the presence of similar molecular structures within a mixed gas makes it challenging to directly extract the contained components due to the overlapping characteristic peaks in SERS spectra. Although the NMF algorithm can identify gas components present in a spectral matrix, it cannot differentiate components within a mixed gas spectrum. Upon spin-coating polymer films onto the sensor, distinct responses are generated for different gases. Hence, modifying the sensor's surface with molecularly imprinted polymer (MIP) is a feasible approach to aid in the extraction and identification of components within mixed gases. The MIP film selectively allows specific gases to pass through and enter the hotspots of the sensor, enabling the collection of SERS spectra for that particular gas. By attaching multiple specific MIP films onto the sensor, distinctive selectivity can be generated for various components within a mixed gas, enabling the analysis of gas composition through a single SERS spectrum integrated with machine learning models (Fig. 5. 6).

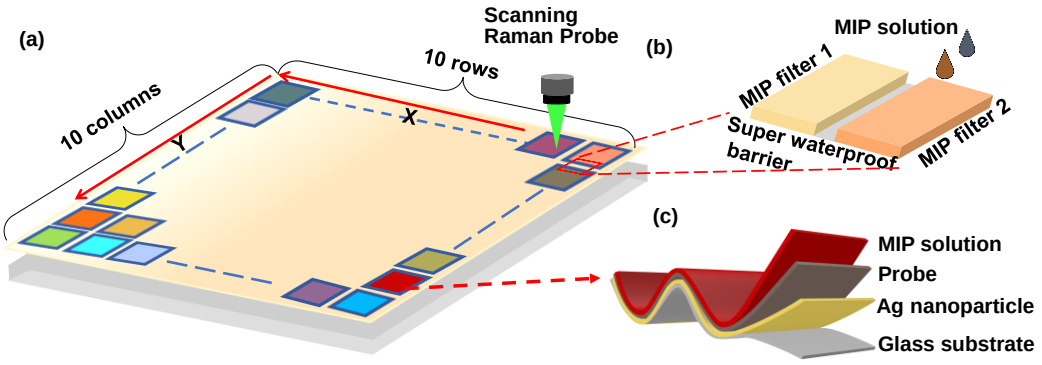

Fig. 5. 6. (a) The constructed SERS sensor array in a 10 × 10 format. (b) Fabrication between the two sensors coated using MIP file. (c) The constructure of the sensor coated with MIP film.

5.2.3 Dynamical visualization of VOC gases

Chapter 4 developed a SERS sensor array to visualize the spatial distribution of

gases evaporating from the odor sources. The localization and size of the odor source were visualized using the proposed method under condition without airflow. Additionally, the visualization results were obtained at a specific time-point, representing a static visualization of gases. In our future work, we plan to record visualization results at multiple time points and construct a time-series of changes, enabling a dynamic and detailed understanding of the spatial diffusion process of VOC gases.

5.2.4 Gas composition visualization system

The spatial distributions of gases evaporating from two odor sources were visualized using a SERS sensor array. In the area where the gases coexisted, the NMF model extracted feature information of these two gases, and they were identified by the CNN model. However, in practical applications, multiple gas sources may coexist in the same area, and they could potentially exist simultaneously in various areas. In future work, our goal is to enhance the current experimental setup to simulate gas mixtures in multiple areas and explore various matrix decomposition methods to visualize the spatial distribution of gas components in the gas mixtures. Additionally, the SERS sensor, coated with selective MIP, will be utilized to facilitate the extraction process of the gas components. Subsequently, the extracted feature data undergoes initial processing through an open-set recognition model to determine its alignment with known gases. Following this, a closed-set recognition model is employed to recognize the known gas, followed by visualization based on the extracted concentration information of the gas. Hence, the gas composition visualization system can be developed utilizing the SERS gas sensing method.

Reference

[1] M. Khatib, and H. Haick, "Sensors for Volatile Organic Compounds," *ACS Nano,* vol. 16, no. 5, pp. 7080-7115, May 24, 2022.

[2] J. Pei, Y. Yin, J. Liu, and X. Dai, "An eight-city study of volatile organic compounds in Chinese residences: Compounds, concentrations, and characteristics," *Sci Total Environ,* vol. 698, pp. 134137, Jan 1, 2020.

[3] C. He, J. Cheng, X. Zhang, M. Douthwaite, S. Pattisson, and Z. Hao, "Recent Advances in the Catalytic Oxidation of Volatile Organic Compounds: A Review Based on Pollutant Sorts and Sources," *Chem Rev,* vol. 119, no. 7, pp. 4471-4568, Apr 10, 2019.

[4] Muhammad Shahzad Kamal, Shaikh A. Razzak, and Mohammad M. Hossain, "Catalytic oxidation of volatile organic compounds (VOC) – A review," *Atmospheric Environment,* vol. 140, pp. 117-134, 2016.

[5] Zhixin Liu, Mengyuan Wang, Meng Wu, Xiaoshuang Li, Haochi Liu, Na Niu, Siqi Li, and Ligang Chen, "Volatile organic compounds (VOC) from plants: From release to detection," *TrAC Trends in Analytical Chemistry,* vol. 158, 2023.

[6] L. Maidodou, I. Clarot, M. Leemans, I. Fromantin, E. Marchioni, and D. Steyer, "Unraveling the potential of breath and sweat VOC capture devices for human disease detection: a systematic-like review of canine olfaction and GC-MS analysis," *Front Chem,* vol. 11, pp. 1282450, 2023.

[7] Sunil K. Jha, and Kenshi Hayashi, "Polyacrylic acid polymer and aldehydes template molecule based MIPs coated QCM sensors for detection of pattern aldehydes in body odor," *Sensors and Actuators B: Chemical,* vol. 206, pp. 471-487, 2015.

[8] Mario Vincenzo Russo, Pasquale Avino, Luisa Perugini, and Ivan Notardonato, "Extraction and GC-MS analysis of phthalate esters in food matrices: a review," *RSC Advances,* vol. 5, no. 46, pp. 37023-37043, 2015.

[9] M. Delgado-Rodríguez, M. Ruiz-Montoya, I. Giraldez, R. López, E. Madejón, and M. J. Díaz, "Use of electronic nose and GC-MS in detection and monitoring some VOC," *Atmospheric Environment,* vol. 51, pp. 278-285, 2012.

[10] M. V. Nikolic, V. Milovanovic, Z. Z. Vasiljevic, and Z. Stamenkovic, "Semiconductor Gas Sensors: Materials, Technology, Design, and Application," *Sensors (Basel),* vol. 20, no. 22, Nov 23, 2020.

[11] D. Degler, U. Weimar, and N. Barsan, "Current Understanding of the Fundamental Mechanisms of Doped and Loaded Semiconducting Metal-Oxide-Based Gas Sensing Materials," *ACS Sens,* vol. 4, no. 9, pp. 2228-2249, Sep 27, 2019.

[12] Papot Jaroenapibal, Pundaree Boonma, Nattha Saksilaporn, Mati Horprathum, Vittaya

Amornkitbamrung, and Napat Triroj, "Improved NO2 sensing performance of electrospun WO3 nanofibers with silver doping," *Sensors and Actuators B: Chemical,* vol. 255, pp. 1831-1840, 2018.

[13] Zhong Li, ZhengJun Yao, Azhar Ali Haidry, Tomas Plecenik, LiJuan Xie, LinChao Sun, and Qawareer Fatima, "Resistive-type hydrogen gas sensor based on TiO2: A review," *International Journal of Hydrogen Energy,* vol. 43, no. 45, pp. 21114-21132, 2018.

[14] Manmeet Kaur, S. Kailasaganapathi, Niranjan Ramgir, Niyanta Datta, Sushil Kumar, A. K. Debnath, D. K. Aswal, and S. K. Gupta, "Gas dependent sensing mechanism in ZnO nanobelt sensor," *Applied Surface Science,* vol. 394, pp. 258-266, 2017.

[15] E. Lee, Y. S. Yoon, and D. J. Kim, "Two-Dimensional Transition Metal Dichalcogenides and Metal Oxide Hybrids for Gas Sensing," *ACS Sens,* vol. 3, no. 10, pp. 2045-2060, Oct 26, 2018.

[16] Sikai Zhao, Yanbai Shen, Xiuxiu Yan, Pengfei Zhou, Yaoyu Yin, Rui Lu, Cong Han, Baoyu Cui, and Dezhou Wei, "Complex-surfactant-assisted hydrothermal synthesis of one-dimensional ZnO nanorods for high-performance ethanol gas sensor," *Sensors and Actuators B: Chemical,* vol. 286, pp. 501-511, 2019.

[17] Jin-Ah Park, Jaehyun Moon, Su-Jae Lee, Seong Hyun Kim, Taehyoung Zyung, and Hye Yong Chu, "Structure and CO gas sensing properties of electrospun TiO2 nanofibers," *Materials Letters,* vol. 64, no. 3, pp. 255-257, 2010.

[18] Xiaopeng Li, Ying Wang, Yu Lei, and Zhiyong Gu, "Highly sensitive H2S sensor based on template-synthesized CuO nanowires," *RSC Advances,* vol. 2, no. 6, 2012.

[19] Xianfeng Wang, Bin Ding, Min Sun, Jianyong Yu, and Gang Sun, "Nanofibrous polyethyleneimine membranes as sensitive coatings for quartz crystal microbalance-based formaldehyde sensors," *Sensors and Actuators B: Chemical,* vol. 144, no. 1, pp. 11-17, 2010.

[20] Zhihua Ying, Yadong Jiang, Xiaosong Du, Guangzhong Xie, Junsheng Yu, and Huiling Tai, "Polymer coated sensor array based on quartz crystal microbalance for chemical agent analysis," *European Polymer Journal,* vol. 44, no. 4, pp. 1157-1164, 2008.

[21] Sibel Emi˙r Di˙ltemi˙z, and Kardelen Ecevi˙t, "High-performance formaldehyde adsorption on CuO/ZnO composite nanofiber coated QCM sensors," *Journal of Alloys and Compounds,* vol. 783, pp. 608-616, 2019.

[22] Juan Xie, Hu Wang, and Ming Duan, "QCM chemical sensor based on ZnO colloid spheres for the alcohols," *Sensors and Actuators B: Chemical,* vol. 203, pp. 239-244, 2014.

[23] Stefan I. Boyadjiev, Velichka Georgieva, Nicolaie Stefan, George E. Stan, Natalia Mihailescu, Anita Visan, Ion N. Mihailescu, Cristina Besleaga, and Imre M. Szilágyi,

"Characterization of PLD grown WO 3 thin films for gas sensing," *Applied Surface Science,* vol. 417, pp. 218-223, 2017.

[24] Pengjia Qi, Chen Zhao, Rui Wang, Teng Fei, and Tong Zhang, "High-Performance QCM Humidity Sensors Using Acidized-Multiwalled Carbon Nanotubes as Sensing Film," *IEEE Sensors Journal,* vol. 18, no. 13, pp. 5278-5283, 2018.

[25] Jin Chul Yang, Suck Won Hong, Sangheon Jeon, Woon Ik Park, Myunghwan Byun, and Jinyoung Park, "Molecular imprinting of hemispherical pore-structured thin films via colloidal lithography for gaseous formaldehyde Gravimetric sensing," *Applied Surface Science,* vol. 570, 2021.

[26] K. Liu, and C. Zhang, "Volatile organic compounds gas sensor based on quartz crystal microbalance for fruit freshness detection: A review," *Food Chem,* vol. 334, pp. 127615, Jan 1, 2021.

[27] Reza Diharja, Muhammad Rivai, Totok Mujiono, and Harris Pirngadi, "Carbon Monoxide Sensor Based on Non-Dispersive Infrared Principle," *Journal of Physics: Conference Series,* vol. 1201, no. 1, 2019.

[28] V. V. Tipparaju, S. J. Mora, J. Yu, F. Tsow, and X. Xian, "Wearable Transcutaneous CO(2) Monitor Based on Miniaturized Nondispersive Infrared Sensor," *IEEE Sens J,* vol. 21, no. 15, pp. 17327-17334, Aug 1, 2021.

[29] T. V. Dinh, D. J. Kim, J. W. Ahn, I. Y. Choi, J. Y. Lee, Y. S. Son, and J. C. Kim, "A Potential Approach to Compensate the Gas Interference for the Analysis of NO by a Non-dispersive Infrared Technique," *Anal Chem,* vol. 92, no. 18, pp. 12152-12159, Sep 15, 2020.

[30] Ravindra Kumar Jha, "Non-Dispersive Infrared Gas Sensing Technology: A Review," *IEEE Sensors Journal,* vol. 22, no. 1, pp. 6-15, 2022.

[31] Trieu-Vuong Dinh, In-Young Choi, Youn-Suk Son, and Jo-Chun Kim, "A review on non-dispersive infrared gas sensors: Improvement of sensor detection limit and interference correction," *Sensors and Actuators B: Chemical,* vol. 231, pp. 529-538, 2016.

[32] Huang Xiao-wei, Zou Xiao-bo, Shi Ji-yong, Li Zhi-hua, and Zhao Jie-wen, "Colorimetric sensor arrays based on chemo-responsive dyes for food odor visualization," *Trends in Food Science & Technology,* vol. 81, pp. 90-107, 2018.

[33] J. Yu, D. Wang, V. V. Tipparaju, F. Tsow, and X. Xian, "Mitigation of Humidity Interference in Colorimetric Sensing of Gases," *ACS Sens,* vol. 6, no. 2, pp. 303-320, Feb 26, 2021.

[34] Xingcai Qin, Rui Wang, Francis Tsow, Erica Forzani, Xiaojun Xian, and Nongjian Tao, "A Colorimetric Chemical Sensing Platform for Real-Time Monitoring of Indoor

Formaldehyde," *IEEE Sensors Journal,* vol. 15, no. 3, pp. 1545-1551, 2015.

[35] Anders Berliner, Myung-Goo Lee, Yagang Zhang, Seong H. Park, Raymond Martino, Paul A. Rhodes, Gi-Ra Yi, and Sung H. Lim, "A patterned colorimetric sensor array for rapid detection of TNT at ppt level," *RSC Advances,* vol. 4, no. 21, 2014.

[36] Z. Li, J. R. Askim, and K. S. Suslick, "The Optoelectronic Nose: Colorimetric and Fluorometric Sensor Arrays," *Chem Rev,* vol. 119, no. 1, pp. 231-292, Jan 9, 2019.

[37] Young Jin Yoo, Joo Hwan Ko, Won-Guen Kim, Yeong Jae Kim, Duk-Jo Kong, Seungchul Kim, Jin-Woo Oh, and Young Min Song, "Dual-Mode Colorimetric Sensor Based on Ultrathin Resonating Facilitator Capable of Nanometer-Thick Virus Detection for Environment Monitoring," *ACS Applied Nano Materials,* vol. 3, no. 7, pp. 6636-6644, 2020.

[38] Z. Li, and K. S. Suslick, "A Hand-Held Optoelectronic Nose for the Identification of Liquors," *ACS Sens,* vol. 3, no. 1, pp. 121-127, Jan 26, 2018.

[39] L. Wu, and X. Qu, "Cancer biomarker detection: recent achievements and challenges," *Chem Soc Rev,* vol. 44, no. 10, pp. 2963-97, May 21, 2015.

[40] N. Queralto, A. N. Berliner, B. Goldsmith, R. Martino, P. Rhodes, and S. H. Lim, "Detecting cancer by breath volatile organic compound analysis: a review of array-based sensors," *J Breath Res,* vol. 8, no. 2, pp. 027112, Jun, 2014.

[41] J. H. Cha, D. H. Kim, S. J. Choi, W. T. Koo, and I. D. Kim, "Sub-Parts-per-Million Hydrogen Sulfide Colorimetric Sensor: Lead Acetate Anchored Nanofibers toward Halitosis Diagnosis," *Anal Chem,* vol. 90, no. 15, pp. 8769-8775, Aug 7, 2018.

[42] Xiang-Yang Zhang, Yu-Shun Yang, Wei Wang, Qing-Cai Jiao, and Hai-Liang Zhu, "Fluorescent sensors for the detection of hydrazine in environmental and biological systems: Recent advances and future prospects," *Coordination Chemistry Reviews,* vol. 417, 2020.

[43] C. Dossantos, A. Harte, S. Quinn, and T. Gunnlaugsson, "Recent developments in the field of supramolecular lanthanide luminescent sensors and self-assemblies," *Coordination Chemistry Reviews,* vol. 252, no. 23-24, pp. 2512-2527, 2008.

[44] S. Bonacchi, D. Genovese, R. Juris, M. Montalti, L. Prodi, E. Rampazzo, M. Sgarzi, and N. Zaccheroni, "Luminescent chemosensors based on silica nanoparticles," *Top Curr Chem,* vol. 300, pp. 93-138, 2011.

[45] H. Y. Li, S. N. Zhao, S. Q. Zang, and J. Li, "Functional metal-organic frameworks as effective sensors of gases and volatile compounds," *Chem Soc Rev,* vol. 49, no. 17, pp. 6364-6401, Sep 7, 2020.

[46] X. G. Liu, H. Wang, B. Chen, Y. Zou, Z. G. Gu, Z. Zhao, and L. Shen, "A luminescent metal-organic framework constructed using a tetraphenylethene-based ligand for

sensing volatile organic compounds," *Chem Commun (Camb),* vol. 51, no. 9, pp. 1677-80, Jan 31, 2015.

[47] S. Rochat, and T. M. Swager, "Conjugated amplifying polymers for optical sensing applications," *ACS Appl Mater Interfaces,* vol. 5, no. 11, pp. 4488-502, Jun 12, 2013.

[48] A. S. Klymchenko, "Solvatochromic and Fluorogenic Dyes as Environment-Sensitive Probes: Design and Biological Applications," *Acc Chem Res,* vol. 50, no. 2, pp. 366-375, Feb 21, 2017.

[49] J. Zhang, M. Zhou, X. Li, Y. Fan, J. Li, K. Lu, H. Wen, and J. Ren, "Recent advances of fluorescent sensors for bacteria detection-A review," *Talanta,* vol. 254, pp. 124133, Mar 1, 2023.

[50] C. Jing, Y. Wang, X. Song, X. Li, M. Kou, G. Zhang, W. Dou, and W. Liu, "Dual-Fluorophore and Dual-Site Multifunctional Fluorescence Sensor for Visualizing the Metabolic Process of GHS to SO(2) and the SO(2) Toxicological Mechanism by Two-Photon Imaging," *Anal Chem,* vol. 95, no. 2, pp. 1376-1384, Jan 17, 2023.

[51] Sanyukta Patel, Reena Jamunkar, Deepak Sinha, Monisha, Tarun Kumar Patle, Tushar Kant, Khemchand Dewangan, and Kamlesh Shrivas, "Recent development in nanomaterials fabricated paper-based colorimetric and fluorescent sensors: A review," *Trends in Environmental Analytical Chemistry,* vol. 31, 2021.

[52] Krishna Persaud, and George Dodd, "Analysis of discrimination mechanisms in the mammalian olfactory system using a model nose," vol. 299, pp. 352-355, 1982.

[53] H. Chen, D. Huo, and J. Zhang, "Gas Recognition in E-Nose System: A Review," *IEEE Trans Biomed Circuits Syst,* vol. 16, no. 2, pp. 169-184, Apr, 2022.

[54] Xingan Yang, Meng Li, Xiaohua Ji, Junqing Chang, Zanhong Deng, and Gang Meng, "Recognition Algorithms in E-Nose: A Review," *IEEE Sensors Journal,* vol. 23, no. 18, pp. 20460-20472, 2023.

[55] Juzhong Tan, and Jie Xu, "Applications of electronic nose (e-nose) and electronic tongue (e-tongue) in food quality-related properties determination: A review," *Artificial Intelligence in Agriculture,* vol. 4, pp. 104-115, 2020.

[56] Arunkumar Shanmugasundaram, Sunkara V Manorama, Dong-Su Kim, Yun-Jin Jeong, and Dong Weon Lee, "Toward Point-of-Care chronic disease Management: Biomarker detection in exhaled breath using an E-Nose sensor based on rGO/SnO2 superstructures," *Chemical Engineering Journal,* vol. 448, 2022.

[57] L. Xu, X. Yu, L. Liu, and R. Zhang, "A novel method for qualitative analysis of edible oil oxidation using an electronic nose," *Food Chem,* vol. 202, pp. 229-35, Jul 1, 2016.

[58] V. Schroeder, E. D. Evans, Y. M. Wu, C. A. Voll, B. R. McDonald, S. Savagatrup, and T. M. Swager, "Chemiresistive Sensor Array and Machine Learning Classification of Food,"

ACS Sens, vol. 4, no. 8, pp. 2101-2108, Aug 23, 2019.

[59] S. Qiu, J. Wang, and L. Gao, "Discrimination and characterization of strawberry juice based on electronic nose and tongue: comparison of different juice processing approaches by LDA, PLSR, RF, and SVM," *J Agric Food Chem,* vol. 62, no. 27, pp. 6426-34, Jul 9, 2014.

[60] Zhongzhou Li, Jun Yu, Diandian Dong, Guanyu Yao, Guangfen Wei, Aixiang He, Hao Wu, Huichao Zhu, Zhengxing Huang, and Zhenan Tang, "E-nose based on a high-integrated and low-power metal oxide gas sensor array," *Sensors and Actuators B: Chemical,* vol. 380, 2023.

[61] C. H. Pan, H. Y. Hsieh, and K. T. Tang, "An analog multilayer perceptron neural network for a portable electronic nose," *Sensors (Basel),* vol. 13, no. 1, pp. 193-207, Dec 24, 2012.

[62] Hongli Ma, Tao Wang, Bolong Li, Weiyang Cao, Min Zeng, Jianhua Yang, Yanjie Su, Nantao Hu, Zhihua Zhou, and Zhi Yang, "A low-cost and efficient electronic nose system for quantification of multiple indoor air contaminants utilizing HC and PLSR," *Sensors and Actuators B: Chemical,* vol. 350, 2022.

[63] M. Kang, I. Cho, J. Park, J. Jeong, K. Lee, B. Lee, D. Del Orbe Henriquez, K. Yoon, and I. Park, "High Accuracy Real-Time Multi-Gas Identification by a Batch-Uniform Gas Sensor Array and Deep Learning Algorithm," *ACS Sens,* vol. 7, no. 2, pp. 430-440, Feb 25, 2022.

[64] Kranthi Kumar Pulluri, and Vaegae Naveen Kumar, "Development of an Integrated Soft E-Nose for Food Quality Assessment," *IEEE Sensors Journal,* vol. 22, no. 15, pp. 15111-15122, 2022.

[65] Xuan Deng, Qing-Hao Meng, Tao Jing, and Hui-Rang Hou, "A Portable E-Nose Endowed With Subjective Evaluation Function of Air Quality in Vehicles," *IEEE Transactions on Instrumentation and Measurement,* vol. 71, pp. 1-11, 2022.

[66] Q. Chen, Z. Chen, D. Liu, Z. He, and J. Wu, "Constructing an E-Nose Using Metal-Ion-Induced Assembly of Graphene Oxide for Diagnosis of Lung Cancer via Exhaled Breath," *ACS Appl Mater Interfaces,* vol. 12, no. 15, pp. 17713-17724, Apr 15, 2020.

[67] Andreas T. Güntner, Vitaly Koren, Kiran Chikkadi, Marco Righettoni, and Sotiris E. Pratsinis, "E-Nose Sensing of Low-ppb Formaldehyde in Gas Mixtures at High Relative Humidity for Breath Screening of Lung Cancer?," *ACS Sensors,* vol. 1, no. 5, pp. 528-535, 2016.

[68] S. Lekha, and S. M, "Recent Advancements and Future Prospects on E-Nose Sensors Technology and Machine Learning Approaches for Non-Invasive Diabetes Diagnosis: A Review," *IEEE Rev Biomed Eng,* vol. 14, pp. 127-138, 2021.

[69] J. Langer, D. Jimenez de Aberasturi, J. Aizpurua, R. A. Alvarez-Puebla, B. Auguie, J. J. Baumberg, G. C. Bazan, S. E. J. Bell, A. Boisen, A. G. Brolo, J. Choo, D. Cialla-May, V. Deckert, L. Fabris, K. Faulds, F. J. Garcia de Abajo, R. Goodacre, D. Graham, A. J. Haes, C. L. Haynes, C. Huck, T. Itoh, M. Kall, J. Kneipp, N. A. Kotov, H. Kuang, E. C. Le Ru, H. K. Lee, J. F. Li, X. Y. Ling, S. A. Maier, T. Mayerhofer, M. Moskovits, K. Murakoshi, J. M. Nam, S. Nie, Y. Ozaki, I. Pastoriza-Santos, J. Perez-Juste, J. Popp, A. Pucci, S. Reich, B. Ren, G. C. Schatz, T. Shegai, S. Schlucker, L. L. Tay, K. G. Thomas, Z. Q. Tian, R. P. Van Duyne, T. Vo-Dinh, Y. Wang, K. A. Willets, C. Xu, H. Xu, Y. Xu, Y. S. Yamamoto, B. Zhao, and L. M. Liz-Marzan, "Present and Future of Surface-Enhanced Raman Scattering," *ACS Nano,* vol. 14, no. 1, pp. 28-117, Jan 28, 2020.

[70] T. Itoh, M. Prochazka, Z. C. Dong, W. Ji, Y. S. Yamamoto, Y. Zhang, and Y. Ozaki, "Toward a New Era of SERS and TERS at the Nanometer Scale: From Fundamentals to Innovative Applications," *Chem Rev,* vol. 123, no. 4, pp. 1552-634, Feb 6, 2023.

[71] Armandas Balčytis, Yoshiaki Nishijima, Sivashankar Krishnamoorthy, Aleksandr Kuchmizhak, Paul R. Stoddart, Raimondas Petruškevičius, and Saulius Juodkazis, "From Fundamental toward Applied SERS: Shared Principles and Divergent Approaches," *Advanced Optical Materials,* vol. 6, no. 16, 2018.

[72] Fleischmann M, Hendra PJ, and McQuillan AJ, "Raman-spectra of pyridine adsorbed at a silver electrode," *Chemical Physics Letters,* vol. 26, pp. 163-166, 1974.

[73] Jeanmaire DL, and Van Duyne RP., "Surface raman spectroelectrochemistry Part I. Heterocyclic, aromatic, and aliphatic amines adsorbed on the anodized silver electrode," *Journal of Electroanalytical Chemistry,* vol. 84, pp. 1-20, 1977.

[74] Albrecht MG, and Creighton JA., "Anomalously intense Raman-spectra of pyridine at a silver electrode," *Journal of American Chemical Society,* vol. 99, pp. 5215-5217, 1977.

[75] A. I. Perez-Jimenez, D. Lyu, Z. Lu, G. Liu, and B. Ren, "Surface-enhanced Raman spectroscopy: benefits, trade-offs and future developments," *Chem Sci,* vol. 11, no. 18, pp. 4563-4577, Apr 14, 2020.

[76] M. Moskovits, "Persistent misconceptions regarding SERS," *Phys Chem Chem Phys,* vol. 15, no. 15, pp. 5301-11, Apr 21, 2013.

[77] M. Constantinou, K. Hadjigeorgiou, S. Abalde-Cela, and C. Andreou, "Label-Free Sensing with Metal Nanostructure-Based Surface-Enhanced Raman Spectroscopy for Cancer Diagnosis," *ACS Appl Nano Mater,* vol. 5, no. 9, pp. 12276-12299, Sep 23, 2022.

[78] Song-Yuan Ding, Jun Yi, Jian-Feng Li, Bin Ren, De-Yin Wu, Rajapandiyan Panneerselvam, and Zhong-Qun Tian, "Nanostructure-based plasmon-enhanced Raman spectroscopy for surface analysis of materials," *Nature Reviews Materials,* vol. 1, no. 6, 2016.

[79] Kristin L. Wustholz, Anne-Isabelle Henry, Jeffrey M. McMahon, R. Griffith Freeman, Nicholas Valley, Marcelo E. Piotti, Michael J. Natan, George C. Schatz, and Richard P. Van Duyne, "Structure-Activity Relationships in Gold Nanoparticle Dimersand Trimers for Surface-Enhanced Raman Spectroscopy," *Journal of the American Chemical Society,* vol. 132, 2010.

[80] L. B. T. Nguyen, Y. X. Leong, C. S. L. Koh, S. X. Leong, S. K. Boong, H. Y. F. Sim, G. C. Phan-Quang, I. Y. Phang, and X. Y. Ling, "Inducing Ring Complexation for Efficient Capture and Detection of Small Gaseous Molecules Using SERS for Environmental Surveillance," *Angew Chem Int Ed Engl,* vol. 61, no. 33, pp. e202207447, Aug 15, 2022.

[81] H. Kim, B. T. Trinh, K. H. Kim, J. Moon, H. Kang, K. Jo, R. Akter, J. Jeong, E. K. Lim, J. Jung, H. S. Choi, H. G. Park, O. S. Kwon, I. Yoon, and T. Kang, "Au@ZIF-8 SERS paper for food spoilage detection," *Biosens Bioelectron,* vol. 179, pp. 113063, May 1, 2021.

[82] S. X. Leong, Y. X. Leong, E. X. Tan, H. Y. F. Sim, C. S. L. Koh, Y. H. Lee, C. Chong, L. S. Ng, J. R. T. Chen, D. W. C. Pang, L. B. T. Nguyen, S. K. Boong, X. Han, Y. C. Kao, Y. H. Chua, G. C. Phan-Quang, I. Y. Phang, H. K. Lee, M. Y. Abdad, N. S. Tan, and X. Y. Ling, "Noninvasive and Point-of-Care Surface-Enhanced Raman Scattering (SERS)-Based Breathalyzer for Mass Screening of Coronavirus Disease 2019 (COVID-19) under 5 min," *ACS Nano,* vol. 16, no. 2, pp. 2629-2639, Feb 22, 2022.

[83] X. Qiao, X. Chen, C. Huang, A. Li, X. Li, Z. Lu, and T. Wang, "Detection of Exhaled Volatile Organic Compounds Improved by Hollow Nanocages of Layered Double Hydroxide on Ag Nanowires," *Angew Chem Int Ed Engl,* vol. 58, no. 46, pp. 16523-16527, Nov 11, 2019.

[84] J. Xu, Y. Xu, J. Li, J. Zhao, X. Jian, J. Xu, Z. Gao, and Y. Y. Song, "Construction of High-Active SERS Cavities in a TiO(2) Nanochannels-Based Membrane: A Selective Device for Identifying Volatile Aldehyde Biomarkers," *ACS Sens,* vol. 8, no. 9, pp. 3487-3497, Sep 22, 2023.

[85] Myoung - Kyu Oh, Ranjit De, and Sang - Youp Yim, "Highly sensitive VOC gas sensor employing deep cooling of SERS film," *Journal of Raman Spectroscopy,* vol. 49, no. 5, pp. 800-809, 2018.

[86] X. Qiao, B. Su, C. Liu, Q. Song, D. Luo, G. Mo, and T. Wang, "Selective Surface Enhanced Raman Scattering for Quantitative Detection of Lung Cancer Biomarkers in Superparticle@MOF Structure," *Adv Mater,* vol. 30, no. 5, Feb, 2018.

[87] Yingfen Jiang, Da-Wen Sun, Hongbin Pu, and Qingyi Wei, "Surface enhanced Raman spectroscopy (SERS): A novel reliable technique for rapid detection of common harmful chemical residues," *Trends in Food Science & Technology,* vol. 75, pp. 10-22, 2018.

[88] H. J. Han, S. H. Cho, S. Han, J. S. Jang, G. R. Lee, E. N. Cho, S. J. Kim, I. D. Kim, M. S.

Jang, H. L. Tuller, J. J. Cha, and Y. S. Jung, "Synergistic Integration of Chemo-Resistive and SERS Sensing for Label-Free Multiplex Gas Detection," *Adv Mater,* vol. 33, no. 44, pp. e2105199, Nov, 2021.

[89] M. Lafuente, F. Almazan, E. Bernad, I. Florea, R. Arenal, M. A. Urbiztondo, R. Mallada, and M. P. Pina, "On-chip monitoring of toxic gases: capture and label-free SERS detection with plasmonic mesoporous sorbents," *Lab Chip,* vol. 23, no. 14, pp. 3160-3171, Jul 12, 2023.

[90] Ailin Li, Xuezhi Qiao, Keyan Liu, Wanqiao Bai, and Tie Wang, "Hollow Metal Organic Framework Improves the Sensitivity and Anti - Interference of the Detection of Exhaled Volatile Organic Compounds," *Advanced Functional Materials,* vol. 32, no. 30, 2022.

[91] N. D. Jayram, D. Aishwarya, S. Sonia, D. Mangalaraj, P. S. Kumar, and G. M. Rao, "Analysis on superhydrophobic silver decorated copper Oxide nanostructured thin films for SERS studies," *J Colloid Interface Sci,* vol. 477, pp. 209-19, Sep 1, 2016.

[92] Jan Krajczewski, Ewa Dumiszewska, Dariusz Czolak, Sylwia Turczyniak Surdacka, and Andrzej Kudelski, "New, epitaxial approach to SERS platform preparation – InP nanowires coated by an Au layer as a new, highly active, and stable SERS platform," *Applied Surface Science,* vol. 607, 2023.

[93] Dan Wang, Guanchen Xu, Xingshuang Zhang, Hongyu Gong, Li Jiang, Guanliang Sun, Yu Li, Guoran Liu, Yong Li, Shikuan Yang, and Xiu Liang, "Dual-functional ultrathin wearable 3D particle-in-cavity SF-AAO-Au SERS sensors for effective sweat glucose and lab-on-glove pesticide detection," *Sensors and Actuators B: Chemical,* vol. 359, 2022.

[94] Rokas Šakalys, Kiang Wei Kho, and Tia E. Keyes, "A reproducible, low cost microfluidic microcavity array SERS platform prepared by soft lithography from a 2 photon 3D printed template," *Sensors and Actuators B: Chemical,* vol. 340, 2021.

[95] H. Im, K. C. Bantz, N. C. Lindquist, C. L. Haynes, and S. H. Oh, "Vertically oriented sub-10-nm plasmonic nanogap arrays," *Nano Lett,* vol. 10, no. 6, pp. 2231-6, Jun 9, 2010.

[96] Shaorong Si, Wenkai Liang, Yinghui Sun, Jing Huang, Weiliang Ma, Zhiqiang Liang, Qiaoliang Bao, and Lin Jiang, "Facile Fabrication of High - Density Sub - 1 - nm Gaps from Au Nanoparticle Monolayers as Reproducible SERS Substrates," *Advanced Functional Materials,* vol. 26, no. 44, pp. 8137-8145, 2016.

[97] M. Park, H. Jung, Y. Jeong, and K. H. Jeong, "Plasmonic Schirmer Strip for Human Tear-Based Gouty Arthritis Diagnosis Using Surface-Enhanced Raman Scattering," *ACS Nano,* vol. 11, no. 1, pp. 438-443, Jan 24, 2017.

[98] L. Ouyang, L. Yao, T. Zhou, and L. Zhu, "Accurate SERS detection of malachite green in aquatic products on basis of graphene wrapped flexible sensor," *Anal Chim Acta,* vol. 1027, pp. 83-91, Oct 16, 2018.

[99] J. B. Phyo, A. Woo, H. J. Yu, K. Lim, B. H. Cho, H. S. Jung, and M. Y. Lee, "Label-Free SERS Analysis of Urine Using a 3D-Stacked AgNW-Glass Fiber Filter Sensor for the Diagnosis of Pancreatic Cancer and Prostate Cancer," *Anal Chem,* vol. 93, no. 8, pp. 3778-3785, Mar 2, 2021.

[100] S. Lin, H. Guan, Y. Liu, S. Huang, J. Li, W. Hasi, Y. Xu, J. Zou, and B. Dong, "Binary Plasmonic Assembly Films with Hotspot-Type-Dependent Surface-Enhanced Raman Scattering Properties," *ACS Appl Mater Interfaces,* vol. 13, no. 44, pp. 53289-53299, Nov 10, 2021.

[101] Yiran Tian, Hongmei Liu, Ying Chen, Canliang Zhou, Yong Jiang, Chenjie Gu, Tao Jiang, and Jun Zhou, "Seedless one-spot synthesis of 3D and 2D Ag nanoflowers for multiple phase SERS-based molecule detection," *Sensors and Actuators B: Chemical,* vol. 301, 2019.

[102] Muhammad Shafi, Runcheng Liu, Zhipeng Zha, Can Li, Xuejian Du, Sartaj Wali, Shouzhen Jiang, Baoyuan Man, and Mei Liu, "Highly efficient SERS substrates with different Ag interparticle nanogaps based on hyperbolic metamaterials," *Applied Surface Science,* vol. 555, 2021.

[103] Qing Tong, Weijia Wang, Yining Fan, and Lin Dong, "Recent progressive preparations and applications of silver-based SERS substrates," *TrAC Trends in Analytical Chemistry,* vol. 106, pp. 246-258, 2018.

[104] Petra C. Lindholm‐Lehto, and Jouni Vielma, "Controlling of geosmin and 2‐methylisoborneol induced off‐flavours in recirculating aquaculture system farmed fish—A review," *Aquaculture Research,* vol. 50, no. 1, pp. 9-28, 2018.

[105] C. Cortada, L. Vidal, and A. Canals, "Determination of geosmin and 2-methylisoborneol in water and wine samples by ultrasound-assisted dispersive liquid-liquid microextraction coupled to gas chromatography-mass spectrometry," *J Chromatogr A,* vol. 1218, no. 1, pp. 17-22, Jan 7, 2011.

[106] Raju Botta, Pitak Eiamchai, Mati Horprathum, Saksorn Limwichean, Chanunthorn Chananonnawathorn, Viyapol Patthanasettakul, and Noppadon Nuntawong, "Investigation of silver nanorods as reusable SERS-active substrates for trace level detection of 2-MIB volatile organic compound," *Sensors and Actuators B: Chemical,* vol. 271, pp. 122-127, 2018.

[107] R. L. Bristow, I. S. Young, A. Pemberton, J. Williams, and S. Maher, "An extensive review of the extraction techniques and detection methods for the taste and odour compound geosmin (trans-1, 10-dimethyl-trans-9-decalol) in water," *TrAC Trends in Analytical Chemistry,* vol. 110, pp. 233-248, 2019.

[108] Katrin Kneipp, Yang Wang, Harald Kneipp, Lev T. Perelman, Irving Itzkan,

Ramachandra R. Dasari, and Michael S. Feld, "Single Molecule Detection Using Surface-Enhanced Raman Scattering (SERS)," *Phys.Rev. Lett.,* vol. 78, pp. 1667-1670, 1997.

[109] G. C. Phan-Quang, N. Yang, H. K. Lee, H. Y. F. Sim, C. S. L. Koh, Y. C. Kao, Z. C. Wong, E. K. M. Tan, Y. E. Miao, W. Fan, T. Liu, I. Y. Phang, and X. Y. Ling, "Tracking Airborne Molecules from Afar: Three-Dimensional Metal-Organic Framework-Surface-Enhanced Raman Scattering Platform for Stand-Off and Real-Time Atmospheric Monitoring," *ACS Nano,* vol. 13, no. 10, pp. 12090-12099, Oct 22, 2019.

[110] Satoshi Araki, Masashi Watanabe, Fumihiro Sassa, and Kenshi Hayashi, "Raman enhanced structure with reconfigured molecularly-imprinted-polymer for gas deteciton," *2016 IEEE SENSORS*, 2016.

[111] S. Y. Ding, E. M. You, Z. Q. Tian, and M. Moskovits, "Electromagnetic theories of surface-enhanced Raman spectroscopy," *Chem Soc Rev,* vol. 46, no. 13, pp. 4042-4076, Jul 7, 2017.

[112] Bhavya Sharma, Renee R. Frontiera, Anne-Isabelle Henry, Emilie Ringe, and Richard P. Van Duyne, "SERS: Materials, applications, and the future," *Materials Today,* vol. 15, no. 1-2, pp. 16-25, 2012.

[113] S. Yang, X. Dai, B. B. Stogin, and T. S. Wong, "Ultrasensitive surface-enhanced Raman scattering detection in common fluids," *Proc Natl Acad Sci U S A,* vol. 113, no. 2, pp. 268-73, Jan 12, 2016.

[114] Z. Zhang, W. Yu, J. Wang, D. Luo, X. Qiao, X. Qin, and T. Wang, "Ultrasensitive Surface-Enhanced Raman Scattering Sensor of Gaseous Aldehydes as Biomarkers of Lung Cancer on Dendritic Ag Nanocrystals," *Anal Chem,* vol. 89, no. 3, pp. 1416-1420, Feb 7, 2017.

[115] Stefan Cichosz, Anna Masek, and Marian Zaborski, "Polymer-based sensors: A review," *Polymer Testing,* vol. 67, pp. 342-348, 2018.

[116] A. Lv, Y. Pan, and L. Chi, "Gas Sensors Based on Polymer Field-Effect Transistors," *Sensors (Basel),* vol. 17, no. 1, Jan 22, 2017.

[117] B. Chen, H. Guo, C. Liu, L. Shang, X. Ye, L. Chen, C. Feng, and K. Hayashi, "Molecularly imprinted sol-gel/Au@Ag core-shell nano-urchin localized surface plasmon resonance sensor designed in reflection mode for detection of organic acid vapors," *Biosens Bioelectron,* vol. 169, pp. 112639, Dec 1, 2020.

[118] S Edwin Jayaraj, V Ramakrishnan, S Perumal, and M Gurunathan, "Surface enhanced Raman scattering studies of acetophenone on colloidal silver particles," *Pramana,* vol. 47, pp. 255-259, 1996.

[119] L. Sinha, O. Prasad, S. Chand, A. K. Sachan, S. K. Pathak, V. K. Shukla, M. Karabacak,

and A. M. Asiri, "FT-IR, FT-Raman and UV spectroscopic investigation, electronic properties, electric moments, and NBO analysis of anethole using quantum chemical calculations," *Spectrochim Acta A Mol Biomol Spectrosc,* vol. 133, pp. 165-77, Dec 10, 2014.

[120] Bin Ding, Michiyo Yamazaki, and Seimei Shiratori, "Electrospun fibrous polyacrylic acid membrane-based gas sensors," *Sensors and Actuators B: Chemical,* vol. 106, no. 1, pp. 477-483, 2005.

[121] Dnyandeo Pawar, Rajesh Kanawade, Ajay Kumar, Ch N. Rao, Peijiang Cao, Shankar Gaware, Dattatray Late, Sangeeta N. Kale, S. T. Navale, W. J. Liu, D. L. Zhu, Y. M. Lu, and Ravindra K. Sinha, "High-performance dual cavity-interferometric volatile gas sensor utilizing Graphene/PMMA nanocomposite," *Sensors and Actuators B: Chemical,* vol. 312, 2020.

[122] Zhimin Gao, Guoshuai Song, Xuemin Zhang, Qian Li, Shuang Yang, Tieqiang Wang, Yunong Li, Liying Zhang, Lei Guo, and Yu Fu, "A facile PDMS coating approach to room-temperature gas sensors with high humidity resistance and long-term stability," *Sensors and Actuators B: Chemical,* vol. 325, 2020.

[123] Bin Chen, Chuanjun Liu, Lingpu Ge, and Kenshi Hayashi, "Localized surface plasmon resonance gas sensor of Au nano-islands coated with molecularly imprinted polymer: Influence of polymer thickness on sensitivity and selectivity," *Sensors and Actuators B: Chemical,* vol. 231, pp. 787-792, 2016.

[124] Halina Kaczmarek, and Aleksandra Szalla, "Photochemical transformation in poly(acrylic acid)/poly(ethylene oxide) complexes," *Journal of Photochemistry and Photobiology A: Chemistry,* vol. 180, no. 1-2, pp. 46-53, 2006.

[125] Wenyue Su, Shichao Wang, Xuxu Wang, Xianzhi Fu, and Jingning Weng, "Plasma pre-treatment and TiO2 coating of PMMA for the improvement of antibacterial properties," *Surface and Coatings Technology,* vol. 205, no. 2, pp. 465-469, 2010.

[126] J. J. H. Lancastre, N. Fernandes, F. M. A. Margaça, I. M. Miranda Salvado, L. M. Ferreira, A. N. Falcão, and M. H. Casimiro, "Study of PDMS conformation in PDMS-based hybrid materials prepared by gamma irradiation," *Radiation Physics and Chemistry,* vol. 81, no. 9, pp. 1336-1340, 2012.

[127] Y. J. Zhang, S. Chen, P. Radjenovic, N. Bodappa, H. Zhang, Z. L. Yang, Z. Q. Tian, and J. F. Li, "Probing the Location of 3D Hot Spots in Gold Nanoparticle Films Using Surface-Enhanced Raman Spectroscopy," *Anal Chem,* vol. 91, no. 8, pp. 5316-5322, Apr 16, 2019.

[128] S. Cong, Z. Wang, W. Gong, Z. Chen, W. Lu, J. R. Lombardi, and Z. Zhao, "Electrochromic semiconductors as colorimetric SERS substrates with high

reproducibility and renewability," *Nat Commun,* vol. 10, no. 1, pp. 678, Feb 8, 2019.

[129] Liang Shang, Chuanjun Liu, Masashi Watanabe, Bin Chen, and Kenshi Hayashi, "LSPR sensor array based on molecularly imprinted sol-gels for pattern recognition of volatile organic acids," *Sensors and Actuators B: Chemical,* vol. 249, pp. 14-21, 2017.

[130] Félix Lussier, Vincent Thibault, Benjamin Charron, Gregory Q. Wallace, and Jean-Francois Masson, "Deep learning and artificial intelligence methods for Raman and surface-enhanced Raman scattering," *TrAC Trends in Analytical Chemistry,* vol. 124, 2020.

[131] Xin-xing Chen, and Jian Huang, "Odor source localization algorithms on mobile robots: A review and future outlook," *Robotics and Autonomous Systems,* vol. 112, pp. 123-136, 2019.

[132] Tao Jing, Qing - Hao Meng, and Hiroshi Ishida, "Recent Progress and Trend of Robot Odor Source Localization," *IEEJ Transactions on Electrical and Electronic Engineering,* vol. 16, no. 7, pp. 938-953, 2021.

[133] Daigo Terutsuki, Tomoya Uchida, Chihiro Fukui, Yuji Sukekawa, Yuki Okamoto, and Ryohei Kanzaki, "Real-time odor concentration and direction recognition for efficient odor source localization using a small bio-hybrid drone," *Sensors and Actuators B: Chemical,* vol. 339, 2021.

[134] K. Iitani, K. Toma, T. Arakawa, and K. Mitsubayashi, "Transcutaneous Blood VOC Imaging System (Skin-Gas Cam) with Real-Time Bio-Fluorometric Device on Rounded Skin Surface," *ACS Sens,* vol. 5, no. 2, pp. 338-345, Feb 28, 2020.

[135] X. Li, M. M. Chen, H. F. Su, M. L. Zhang, S. Y. Xie, and L. S. Zheng, "Real-Time Sniffing Mass Spectrometry Aided by Venturi Self-Pumping Applicable to Gaseous and Solid Surface Analysis," *Anal Chem,* vol. 94, no. 40, pp. 13719-13727, Oct 11, 2022.

[136] Y. Liu, H. Yang, C. Ma, S. Luo, M. Xu, Z. Wu, W. Li, and S. Liu, "Luminescent Transparent Wood Based on Lignin-Derived Carbon Dots as a Building Material for Dual-Channel, Real-Time, and Visual Detection of Formaldehyde Gas," *ACS Appl Mater Interfaces,* vol. 12, no. 32, pp. 36628-36638, Aug 12, 2020.

[137] Hiroshi Ishida, Takafumi Tokuhiro, Takamichi Nakamoto, and Toyosaka Moriizumi, "Improvement of olfactory video camera gas-odor flow visualization system," *Sensors and Actuators B: Chemical,* vol. 83, pp. 256-261, 2002.

[138] Hiro-Taka Yoshioka, Chuanjun Liu, and Kenshi Hayashi, "Multispectral fluorescence imaging for odorant discrimination and visualization," *Sensors and Actuators B: Chemical,* vol. 220, pp. 1297-1304, 2015.

[139] Masato Matsuoka, Ge Lingpu, Fumihiro Sassa, and Kenshi Hayashi, "Spatiotemporal Visualization of Gases Using 2-D LSPR Gas Sensor," *IEEE Sensors Letters,* vol. 7, no. 9,

pp. 1-4, 2023.

[140] K. Yang, S. Zong, Y. Zhang, Z. Qian, Y. Liu, K. Zhu, L. Li, N. Li, Z. Wang, and Y. Cui, "Array-Assisted SERS Microfluidic Chips for Highly Sensitive and Multiplex Gas Sensing," *ACS Appl Mater Interfaces,* vol. 12, no. 1, pp. 1395-1403, Jan 8, 2020.

[141] S. Lin, Z. Cheng, Q. Li, R. Wang, and F. Yu, "Toward Sensitive and Reliable Surface-Enhanced Raman Scattering Imaging: From Rational Design to Biomedical Applications," *ACS Sens,* vol. 6, no. 11, pp. 3912-3932, Nov 26, 2021.

[142] Dorleta Jimenez de Aberasturi, Malou Henriksen‐Lacey, Lucio Litti, Judith Langer, and Luis M. Liz‐Marzán, "Using SERS Tags to Image the Three‐Dimensional Structure of Complex Cell Models," *Advanced Functional Materials,* vol. 30, no. 14, 2020.

[143] L. Xing, Y. Xiahou, P. Zhang, W. Du, and H. Xia, "Size Control Synthesis of Monodisperse, Quasi-Spherical Silver Nanoparticles To Realize Surface-Enhanced Raman Scattering Uniformity and Reproducibility," *ACS Appl Mater Interfaces,* vol. 11, no. 19, pp. 17637-17646, May 15, 2019.

[144] X. Lin, G. Fang, Y. Liu, Y. He, L. Wang, and B. Dong, "Marangoni Effect-Driven Transfer and Compression at Three-Phase Interfaces for Highly Reproducible Nanoparticle Monolayers," *J Phys Chem Lett,* vol. 11, no. 9, pp. 3573-3581, May 7, 2020.

[145] A. M. Gabudean, D. Biro, and S. Astilean, "Localized surface plasmon resonance (LSPR) and surface-enhanced Raman scattering (SERS) studies of 4-aminothiophenol adsorption on gold nanorods," *Journal of Molecular Structure,* vol. 993, no. 1-3, pp. 420-424, 2011.

[146] Martin Šubr, Martin Petr, Ondřej Kylián, Jiří Kratochvíl, and Marek Procházka, "Large-scale Ag nanoislands stabilized by a magnetron-sputtered polytetrafluoroethylene film as substrates for highly sensitive and reproducible surface-enhanced Raman scattering (SERS)," *Journal of Materials Chemistry C,* vol. 3, no. 43, pp. 11478-11485, 2015.

[147] X. Zhou, F. Zhou, H. Liu, L. Yang, and J. Liu, "Assembly of polymer-gold nanostructures with high reproducibility into a monolayer film SERS substrate with 5 nm gaps for pesticide trace detection," *Analyst,* vol. 138, no. 19, pp. 5832-8, Oct 7, 2013.

[148] K. Yang, K. Zhu, Y. Wang, Z. Qian, Y. Zhang, Z. Yang, Z. Wang, L. Wu, S. Zong, and Y. Cui, "Ti(3)C(2)T(x) MXene-Loaded 3D Substrate toward On-Chip Multi-Gas Sensing with Surface-Enhanced Raman Spectroscopy (SERS) Barcode Readout," *ACS Nano,* vol. 15, no. 8, pp. 12996-13006, Aug 24, 2021.

[149] Mehdi Mafi, Harold Martin, Mercedes Cabrerizo, Jean Andrian, Armando Barreto, and Malek Adjouadi, "A comprehensive survey on impulse and Gaussian denoising filters for digital images," *Signal Processing,* vol. 157, pp. 236-260, 2019.

[150] Arwa Alhadi Omer, Obai Ibrahim Hassan, Abdalazim Ibrahim Ahmed, and Alwaleed Abdelrahman, "Denoising CT Images using Median based Filters a Review," *2018 International Conference on Computer, Control, Electrical, and Electronisc Engineering (ICCCEEE)*, pp. 1-6, 2018.

[151] Jin Wang, Jiaji Wu, Zhensen Wu, Jechang Jeong, and Gwanggil Jeon, "Wiener filter-based wavelet domain denoising," *Displays,* vol. 46, pp. 37-41, 2017.

[152] Lin Chen, Hao Guo, Cong Wang, Bin Chen, Fumihiro Sassa, and Kenshi Hayashi, "Two-Dimensional SERS Sensor Array for Identifying and Visualizing the Gas Spatial Distributions of Two Distinct Odor Sources," *Sensors,* vol. 24, no. 3, 2024.

[153] Cheng Qu, Chuanjun Liu, Yun Gu, Shuiqin Chai, Changhao Feng, and Bin Chen, "Open-set gas recognition: A case-study based on an electronic nose dataset," *Sensors and Actuators B: Chemical,* vol. 360, 2022.

[154] Jiancun Shi, Zefa Yang, Lixin Wu, and Jingjing Niu, "Large-Gradient Interferometric Phase Unwrapping Over Coal Mining Areas Assisted by a 2-D Elliptical Gaussian Function," *IEEE Geoscience and Remote Sensing Letters,* vol. 19, pp. 1-5, 2022.

Appendix A Chapter 3 supporting information

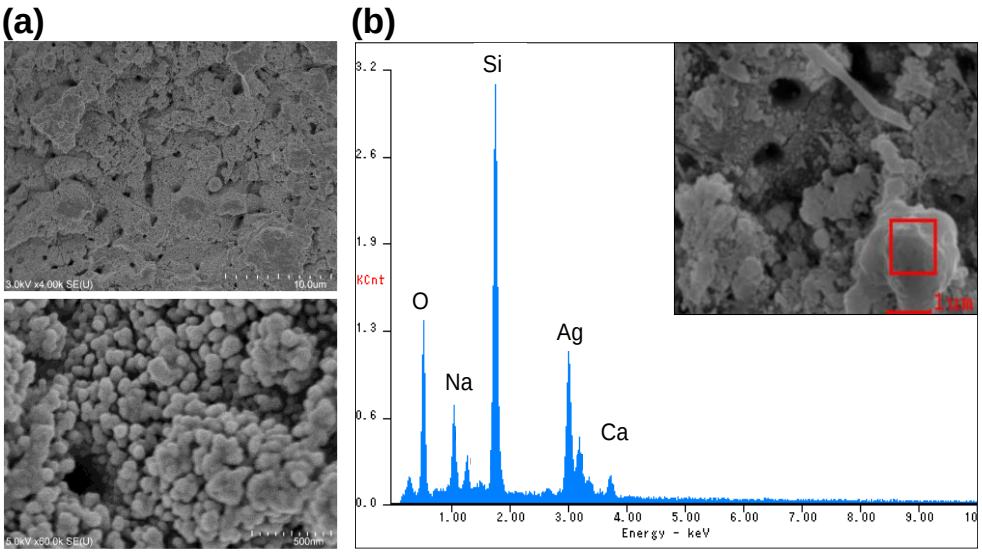

Fig. S3. 1. (a) SEM images of Ag nanoparticles (b) EDX results of selected area obtained from bare sensor.

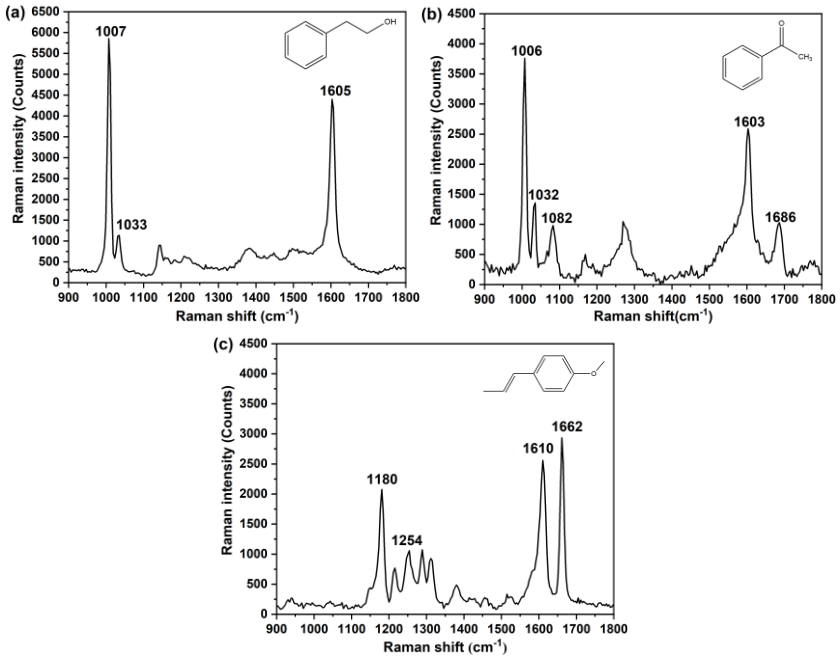

Fig. S3. 2. SERS spectra of (a) phenethyl alcohol, (b) acetophenone and (c) anethole solution detected by bare SRES sensor.

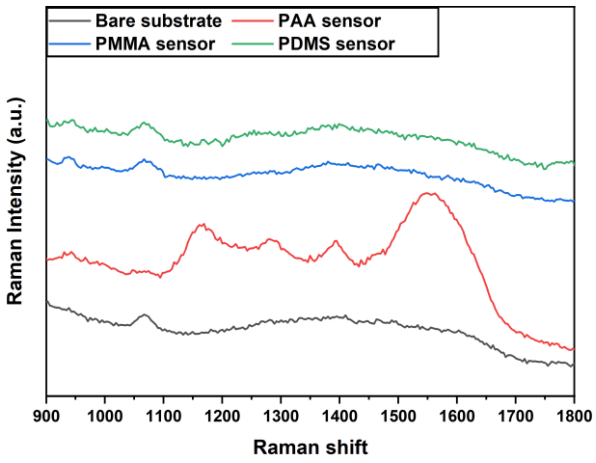

Fig. S3. 3. The background Raman spectra of bare substrate, PAA-, PMMA- and PDMS-coated SERS sensors.

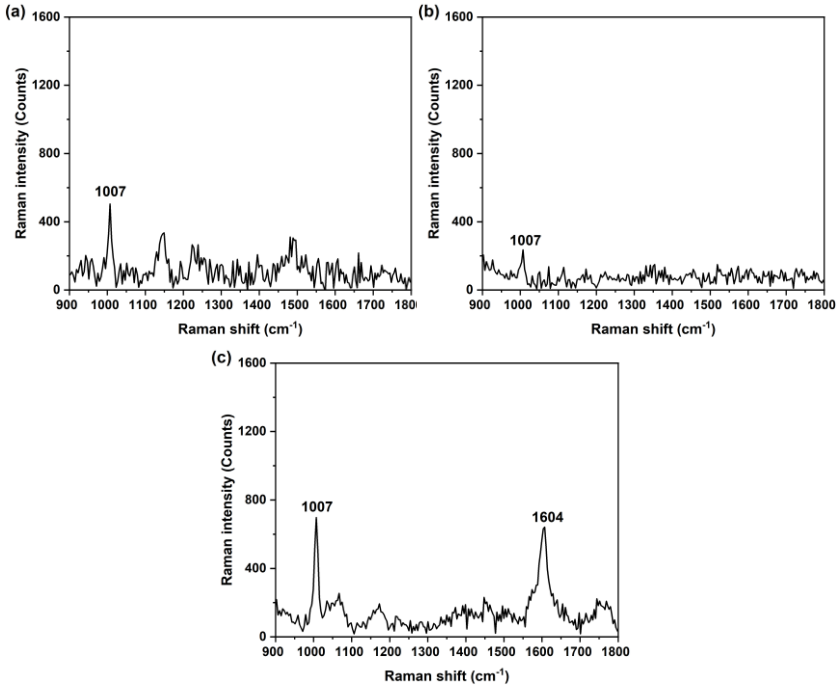

Fig. S3. 4. SERS spectra of phenethyl alcohol gas detected by (a) PAA, (b) PMMA and (c) PDMS coated SERS gas sensor.

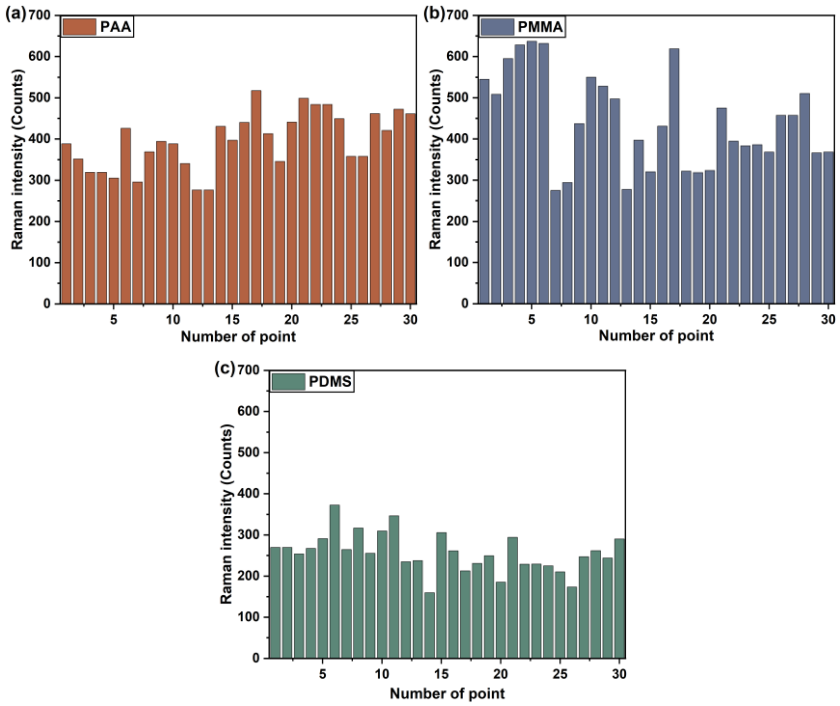

Fig. S3. 5. SERS intensities at 1007 cm^{-1} of random 30 points obtained by using (a) PAA, (b) PMMA and (c) PDMS coated sensors for acetophenone gas detection.

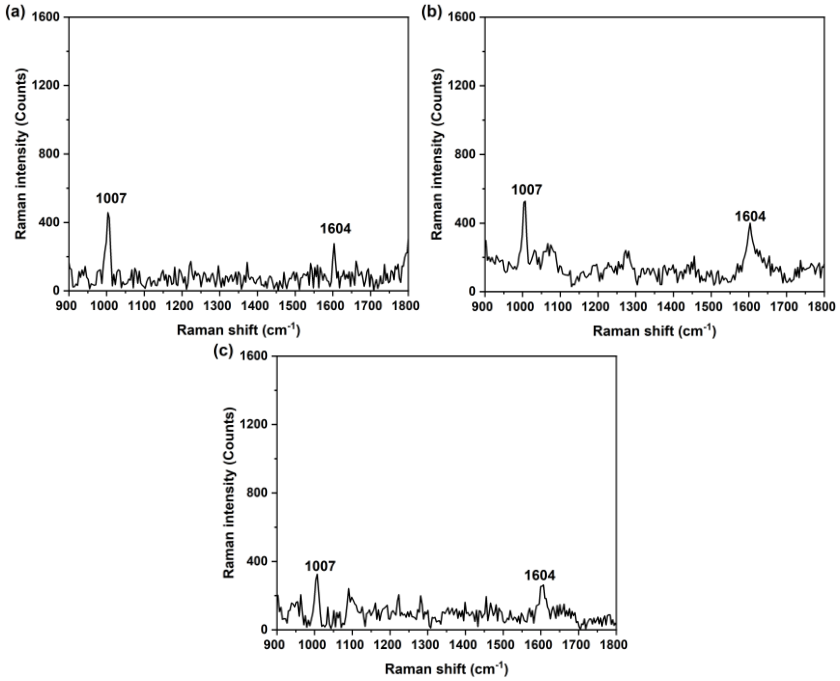

Fig. S3. 6. SERS spectra of acetophenone gas detected by (a) PAA, (b) PMMA and (c) PDMS coated sensors.

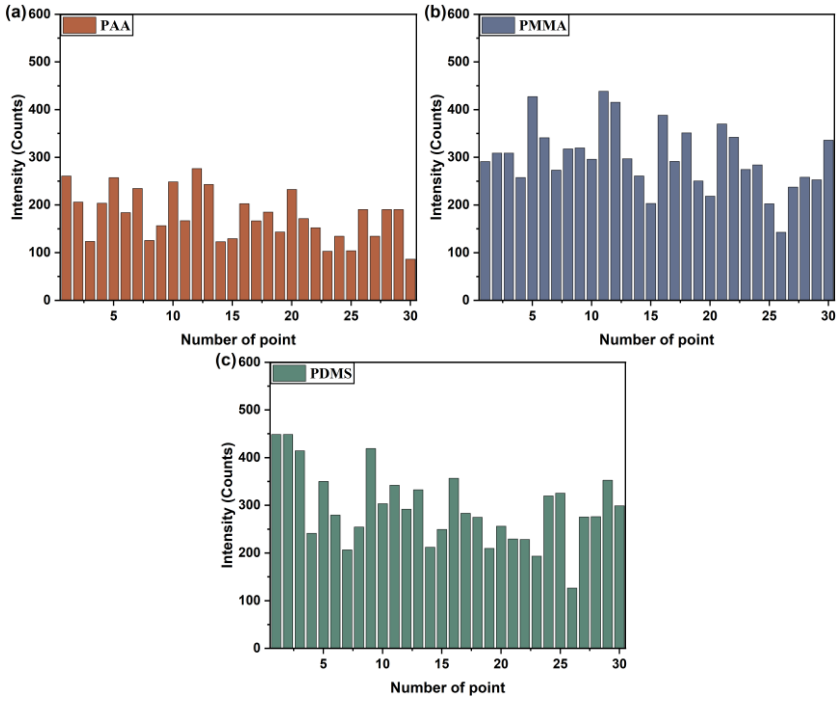

Fig. S3. 7. SERS intensities at 1175 cm^{-1} of random 30 points obtained by using (a) PAA, (b) PMMA and (c) PDMS coated sensors for anethole gas detection.

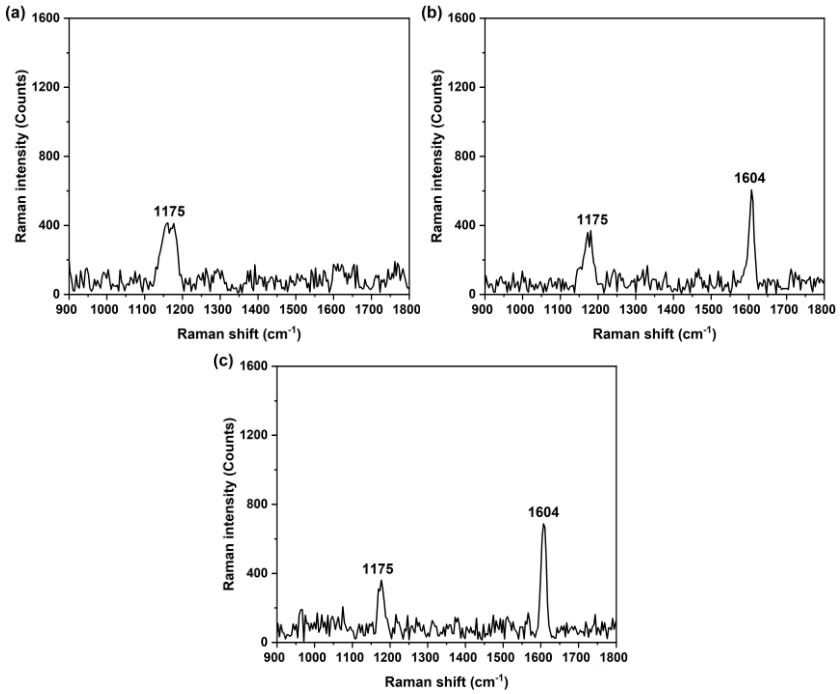

Fig. S3. 8. SERS spectra of anethole gas detected by (a) PAA, (b) PMMA and (c) PDMS coated sensors.

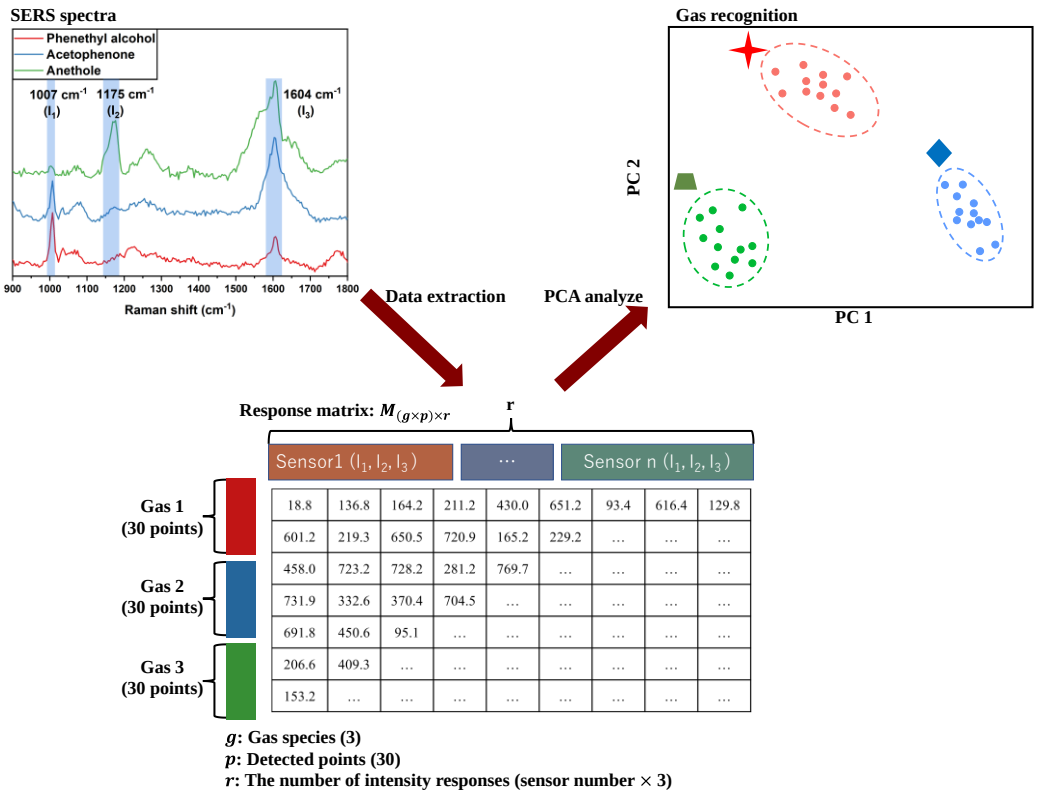

Fig. S3. 9. The response matrix was constructed by utilizing the Raman intensity obtained when gas was detected using SERS sensors covered with different polymer films. Subsequently, the response matrix was analyzed using a PCA model.

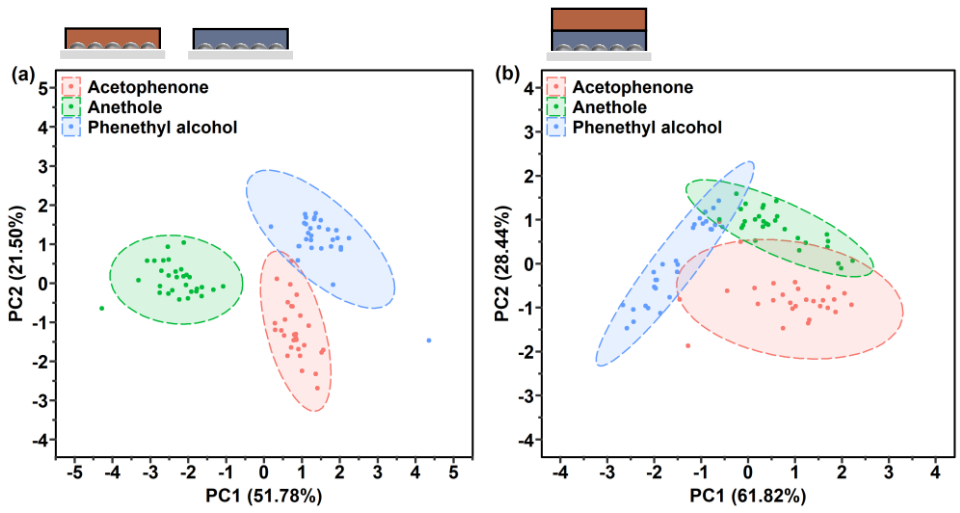

Fig. S3. 10. PCA score plots of the (a) two single-layer film coated PMMA, PAA, (b) one double-layer film coated PMMA-PAA SERS sensors for phenethyl alcohol, acetophenone and anethol gases.

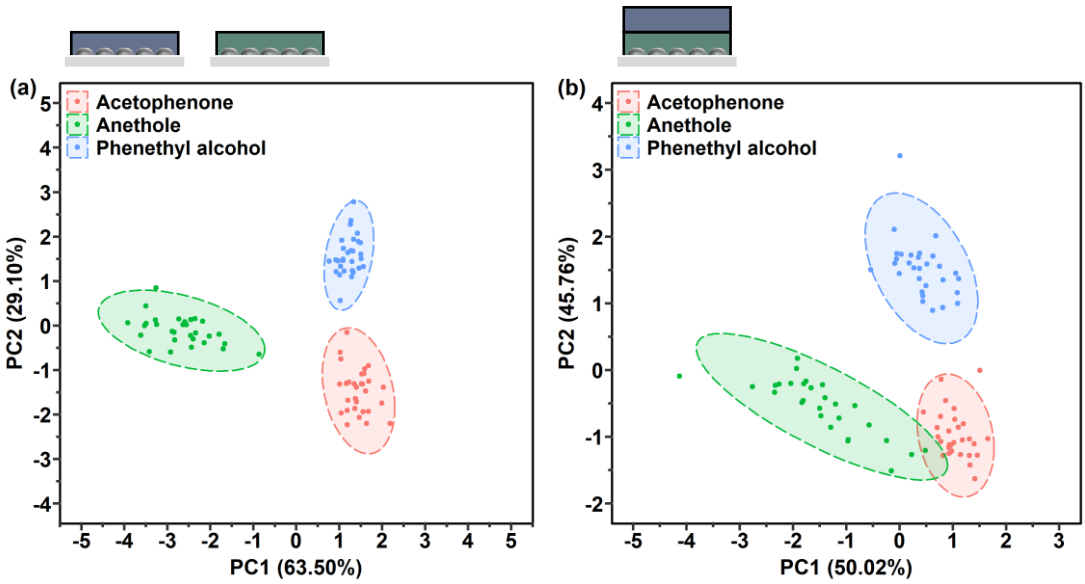

Fig. S3. 11. PCA score plots of the (a) two single-layer film coated PDMS, PMMA, (b) one double-layer film coated PDMS-PMMA SERS sensors for phenethyl alcohol, acetophenone and anethol gases.

Appendix B Chapter 4 supporting information

1. NMF algorithm

The non-negative matrix was decomposed into a feature matrix and a weight matrix using NMF. In this study, the V matrix was constructed by applying the SERS spectra collected from n points on the SERS sensor array, with each spectrum having dimension of m. Therefore, the V was decomposed as

$$V_{n\times m} = W_{n\times r}H_{r\times m} \quad (1)$$

where matrix W represents the concentration of each component at each position, matrix H represents the feature of each component, and r signifies the number of the components extracted from the sensor array. For component 1, $h_{1\times m}$ represents the feature of the component, and $w_{n\times 1}$ represents the concentration of component 1 at each position. Hence, $w_{n\times 1}$ is reconstructed as a matrix to visualize the spatial distribution of the gas, generating a heatmap image. Finally, the component was identified based on the $h_{1\times m}$ feature result.

2. Gaussian fitting method

The experiment's measurements were influenced by several factors, such as variability in gas flow and air interference. The concentration information was not considered to be ideal. Therefore, the heatmap image was processed using Gaussian fitting model. The shape of the gas evaporating from the odor source on the SERS sensor array was nearly circular or elliptical. Consequently, a 2-D Gaussian function was employed to fit the spatial distribution, and this function is expressed as [154]:

$$I(x,y) = A\exp(-(a(x-x_0)^2 + 2b(x-x_0)(y-y_0) + c(y-y_0)^2))$$

$$a = \frac{cos^2\theta}{2\sigma_x{}^2} + \frac{sin^2\theta}{2\sigma_y{}^2}$$

$$b = -\frac{\sin 2\theta}{4\sigma_x{}^2} + \frac{\sin 2\theta}{4\sigma_y{}^2}$$

$$c = \frac{sin^2\theta}{2\sigma_x{}^2} + \frac{cos^2\theta}{2\sigma_y{}^2}$$

Here, (x, y) is the coordinate, x_0 and y_0 are the coordinates of the center point, A is the amplitude, σ_x and σ_y are the standard derivation components, and θ is a rotation angle. These parameters were fitted to construct a Gaussian distribution, and the outcome was utilized to generate a visual representation of the spatial distribution of the gas.

Figure

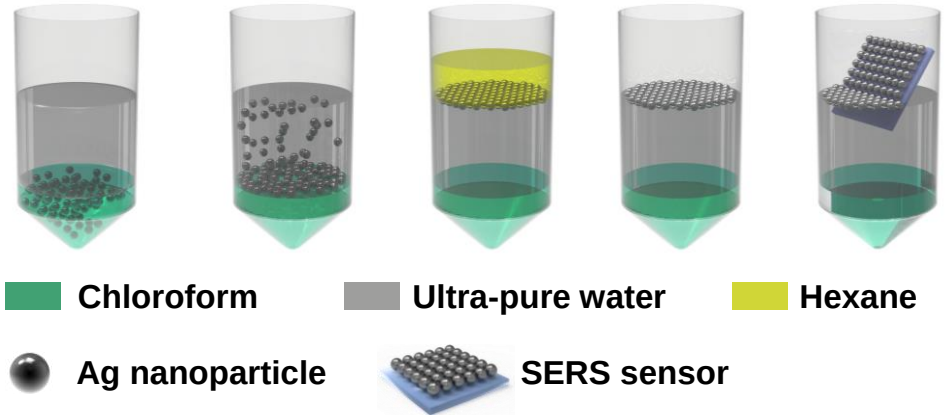

Fig. S4. 1. The fabrication process of the Surface Enhanced Raman Scattering (SERS) sensors, obtained by transferring the Ag nanoparticles (NPs) monolayer film to the glass substrate.

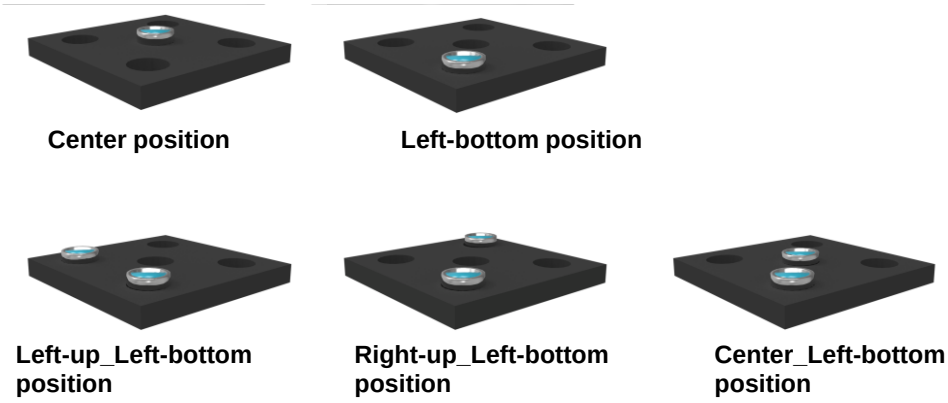

Fig. S4. 2. Five position patterns of the fixed odor sources.

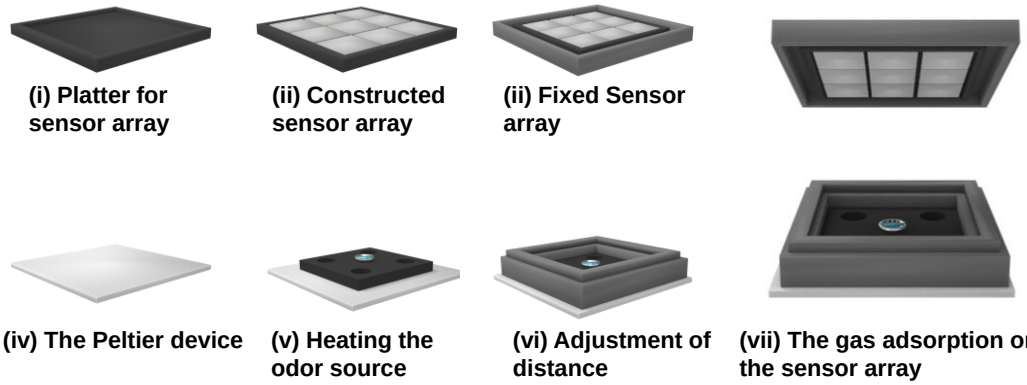

Fig. S4. 3. The process of gas evaporating from the odor source being adsorbed on the Surface Enhanced Raman Scattering (SERS) sensor array. The constructed sensor array (ii) was scanned using our program-controlled X-Y stage.

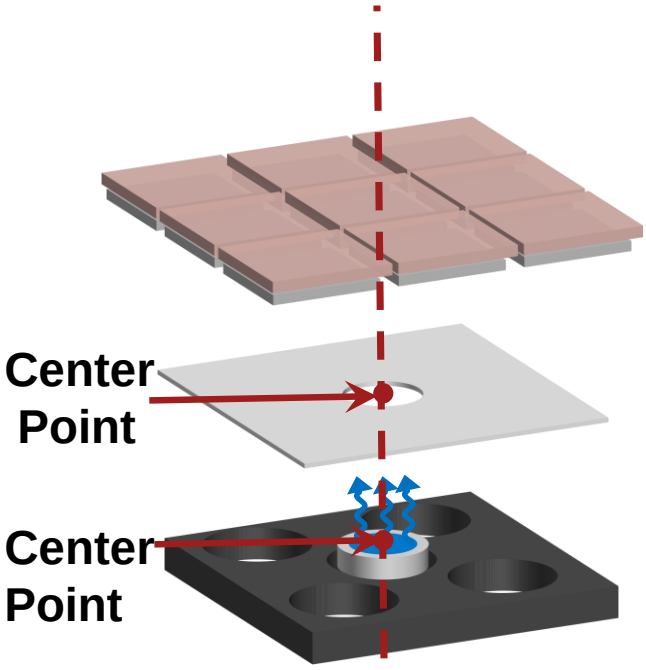

Fig. S4. 4. The schematic graph depicting the detection of odor sources with different sizes.

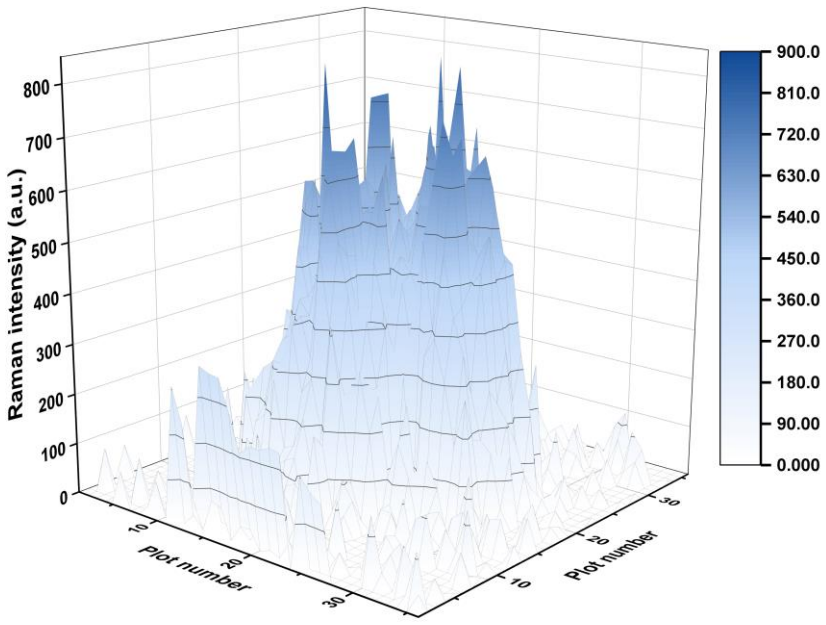

Fig. S4. 5. The 3D graph illustrates the distribution of Raman intensities for benzaldehyde gas evaporating from the odor source positioned in the center.

Table

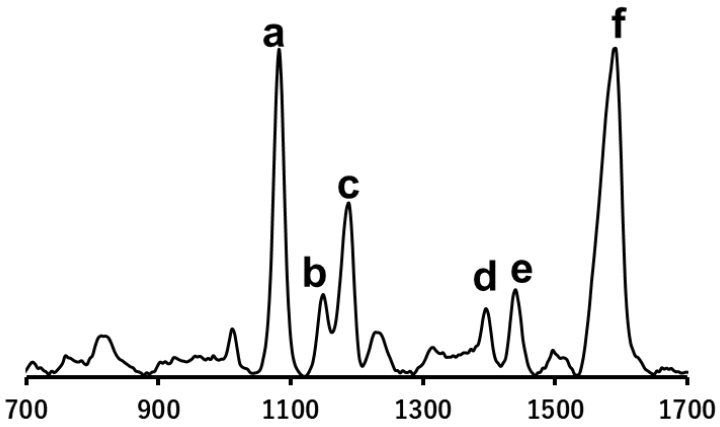

a	1082	v(C=C) + v(C-S)
b	1148	β(C-H) + v(C-N)
c	1181	β(C-H)
d	1394	v(N=N) + v(C-N)
e	1440	v(N=N) + β(C-H)
f	1585	v(C=C)

Table. S4. 1. Vibrational mode assignments for 4-ATP.

Appendix C Chapter 5 supporting information

Table. S5. 1. The main vibrational mode assignments of four vapor samples.

Vapor	Peak position (cm^{-1})	Vibrational mode assignment
Acetophenone	1007	Benzene ring breathing
	1606	Benzene ring stretching
Anethole	1150	v(C-C) in-plane
	1176	v(C-O-C)
	1610	Benzene ring stretching
Anisole	1007	Benzene ring breathing
	1606	Benzene ring stretching
Benzaldehyde	845	γ(C-H)
	1007	Benzene ring breathing
	1606	Benzene ring stretching

For the SVM method, the hyper-parameters were the regularization parameter (C), kernel coefficient (gamma), and kernel type. For the RFC method, the hyper-parameters were the number of trees in the forest (n_estimators), the number of features (max_features), the minimum number of samples at a leaf node (min_samples_leaf), and the function for evaluating the quality of a split (criterion).

Table. S5. 2. Optimal hyper-parameters for the SVM and RFC methods.

Recognition model	Parameters	value
SVM	C	1, 100, 1000, 10000, 100000, 1000000
	gamma	0.000001, 0.00001, 0.0001, 0.001, 0.01, 0.1, 1
	kernel	“rbf”, “linear”
RFC	n_estimators	50, 100, 150, 200
	max_features	6, 12, 18, 24
	min_samples_leaf	5, 10, 20, 30
	criterion	"gini", "entropy"

Table. S5. 3. Optimized hyper-parameters for the SVM classifier and RFC method to give the best accuracy.

Recognition model	Dataset	Parameters
SVM	Normalized data	'C': 100 'gamma': 0.01 'kernel': rbf
	PC_90 data	'C': 100 'gamma': 0.1 'kernel': rbf
	COIF3 data	'C': 10 'gamma': 0.1 'kernel': rbf
RFC	Normalized data	'n_estimators': 200 'max_features': 24 'min_samples_leaf': 5 'criterion': entropy
	PC_70 data	'n_estimators': 150 'max_features': 12, 'min_samples_leaf': 5 'criterion': 'gini'
	DB2 data	'n_estimators': 20 'max_features': 12 'min_samples_leaf': 5 'criterion': 'entropy'